MCGILL UNIVERSITY

DOCTORAL THESIS

On the detector response and the reconstruction of the source intensity distribution in small photon fields

---

Author:

Pavlos

PAPACONSTADOPOULOS

Supervisor:

Dr. Jan SEUNTJENS

A thesis submitted to McGill University in partial fulfillment of the

requirements of the degree of Doctor of Philosophy

in the

Medical Physics Unit

Department of Physics

MCGILL UNIVERSITY

Abstract

Department of Physics

Doctor of Philosophy

On the detector response and the reconstruction of the source intensity distribution in small photon fields

by Pavlos PAPACONSTADOPOULOS

This PhD thesis pertains to the subject of small field dosimetry. Small photon fields, generally referring to fields smaller than 2×2 cm^2, are routinely used in the clinic during modern radiotherapy treatment deliveries. However, several investigators have raised questions regarding the accuracy of the dosimetry in such conditions. An important issue involves the significant perturbations that are caused by most detectors in small field conditions. These perturbations will result in erroneous dose calculations during treatment planning and affect the treatment outcome. Currently it is still not clear which detector system should be preferred in small fields. In this work, the response of modern dosimeters is investigated via Monte Carlo simulations and experiments. Detector-specific correction and perturbation factors are reported for modern detector systems and their accuracy is evaluated experimentally. The need for off-axis corrections is also investigated, a less explored area in previous research. The calibration process, essential for some detector systems, is carefully examined and recommendations are provided. Another unexplored area that directly affects the dosimetry in small fields is the accurate knowledge of the X-ray source distribution. As the field size is reduced and becomes comparable to the X-ray source size, significant accelerator output variations are observed. In principle these variations can be predicted if direct source reconstruction methods are developed. Current source reconstruction methods require special equipment, not easily accessible in every clinic. In this work we suggest a novel approach for the source reconstruction problem, which requires no prior knowledge of the source's functional form nor any specialized equipment. The method is based on a maximum-likelihood expectation-maximization algorithm and utilizes small field photon fluence profiles. The method is evaluated and benchmarked against simulations and experiments and significant sources of uncertainties are identified.

Cette thèse de doctorat porte sur le sujet de la dosimétrie en petits champs. Les sources de photons dits en “petits champs ” font généralement référence à des champs plus petits que $2 \times 2\, cm^2$ et sont couramment utilisés en clinique durant les traitement de radiothérapie modernes. Cependant, plusieurs chercheurs ont soulevé des questions quant à l’exactitude de la dosimétrie dans de telles conditions. Une question importante concerne les perturbations considérables causées par la plupart des détecteurs dans des conditions utilisant des petits champs. Ces perturbations vont entraîner des calculs de doses erronés lors de la planification du traitement et ainsi affecter leur résultat. Actuellement, le système de détecteur à privilégier dans des conditions de petits champs n’a pas encore été déterminé. Dans ce travail, la réponse des dosimètres modernes est étudiée via des simulations Monte-Carlo, ainsi que dans des conditions expérimentales. Les facteurs de corrections et de perturbations spécifiques aux différents détecteurs modernes sont présentés dans cette étude, et leur exactitude est évaluée expérimentalement. La nécessité des corrections hors-axe est également étudiée, une zone moins explorée dans les précédents travaux de recherches. Le processus d’étalonnage, essentiel pour certains systèmes de détection, est méticuleusement examinée et des recommandations sont établies. Un autre domaine inexploré qui affecte directement la dosimétrie en petits champs est la connaissance précise de la distribution spatiale de la source de rayons X. Lorsque la taille du champ est considérablement réduite et devient comparable à la taille de la source, d’importantes variations en sortie de l’accélérateur linéaire sont observées. En principe, ces variations peuvent être prédites si des méthodes de reconstruction directe de la source à rayons X sont développés. Les méthodes de reconstruction de la source actuellement utilisées nécessitent des équipements spéciaux qui sont difficilement accessibles dans chaque clinique de radiothérapie. Dans cette étude, nous proposons une nouvelle approche pour résoudre le problème de la reconstruction de la source à rayons X qui ne nécessite aucune connaissance préalable de la forme fonctionnelle de la source, ni aucun équipement spécialisé. La méthode est basée sur un algorithme dénommé ”maximum-likelihood expectation-maximization” et utilise des profils de fluence de photons en petits champs. La méthode est évaluée et comparée à des simulations et expériences de références, et d'importantes sources d'incertitudes sont identifiées.

Acknowledgements

First of all, I am grateful to my supervisor, Professor Jan Seuntjens, for sharing his expertise in dosimetry and for his continuous support and encouragement during my graduate studies. I would also like to thank the many brilliant researchers I had the honour and pleasure to work and publish papers with: Dr. Frederic Tessier, Dr. Slobodan Devic, Dr. Ives Levesque, Dr. Louis Archambault, Dr. Gyorgy Heigyi and Robert Maglieri. Their expertise and high standards improved substantially the quality of this work.

A special thanks goes to all the members of my PhD committee: Dr. Alasdair Syme, Dr. Stephen Davis, Dr. Frederic Tessier and Dr. Arman Sarfehnia as well as to all the Medical Physics students for many fruitful discussions we had and the constructive feedback I received on the project.

In addition, I would like to acknowledge the support of the following: Joe Larkin for efficiently manufacturing any needed experimental equipment, Michael Evans, Russell Ruo, Horacio Patrocinio and Tanner Connell for providing helpful advices on clinical and research subjects, Margery Knewstubb and Tatjana Nisic for patiently taking care of administrative issues, Lalageh Mirzakhanian and Martin Vallieres for carefully reviewing and correcting this thesis. I am particularly grateful to the Alexander S. Onassis Public Benefit Foundation in Greece, which has partially funded my PhD in the last 3 years.

Finally, it would be amiss if I did not express my gratitude to my parents, Christo and Liletta, for encouraging me to pursue graduate studies abroad and helping me in every challenge I faced.

Contents

List of Figures

List of Tables

List of Abbreviations

CAX	**C**entral **AX**is
CH	**C**ondensed **H**istory
CHUQ	**C**entre **H**ospitalier **U**niversitaire de **Q**uebec
CLR	**C**herenkov **L**ight **R**atio
CPE	**C**harged **P**article **E**quilibrium
CSDA	**C**ontinuously **S**lowing **D**own **A**pproximation
CSE	**C**ross-**S**ection **E**nhancement
CT	**C**omputed **T**omography
CVD	**C**hemical **V**apour **D**eposition
DP	**D**ose **P**rofile
EBRT	**E**xternal **B**eam **R**adiation **T**herapy
ECUT	**E**lectron **CUT**-off
FF	**F**lattening **F**ilter
FFF	**F**lattening **F**ilter **F**ree
FWHM	**F**ull **W**idth **H**alf **M**aximum
FWTM	**F**ull **W**idth **T**enth **M**aximum
IMRT	**I**ntensity **M**odulated **R**adiation **T**herapy
KERMA	**K**inetic **E**nergy **R**eleased **MA**ss
LINAC	**LIN**ear **AC**celerator

MC	**M**onte **C**arlo
MLC	**M**icro-**L**eaf **C**ollimator
MLEM	**M**aximum-**L**ikelihood **E**xpectation-**M**aximization
MTF	**M**odulation **T**ransfer **F**unction
NTCP	**N**ormal **T**issue **C**omplication **P**robability
OAR	**O**rgans **A**t **R**isk
OF	**O**utput **F**actor
PCUT	**P**hoton **CUT**-off
PD	**P**hoto-**D**iode
PDD	**P**ercent **D**epth **D**ose
PMT	**P**hoto-**M**ultiplier **T**ube
PSD	**P**lastic **S**cintillation **D**osimeter
PSF	**P**oint **S**pread **F**unction
PV	**P**ixel **V**alue
RF	**R**adio **F**requency
RMSE	**R**oot **M**ean **S**quare **E**rror
ROI	**R**egion **O**f **I**nterest
SABR	**S**tereotactic **AB**lative **R**adiotherapy
SDD	**S**ource **D**etector **D**istance
SBRT	**S**tereotactic **B**ody **R**adiation **T**herapy
SRS	**S**tereotactic **R**adio**S**urgery
SSD	**S**ource **S**urface **D**istance
TCP	**T**umor **C**ontrol **P**robability

TLD	**T**hermo-**L**uminescent **D**osimeter
TPS	**T**reatment **P**lanning **S**ystem
VRT	**V**ariance **R**eduction **T**echnique

Στην Νάντια μου, που είναι πάντα δίπλα μου...

Chapter 1

Introduction

1.1 Introduction to Radiation Therapy

Cancer is one of the leading causes of mortality in the world. Approximately 14 new cases and 8.2 million cancer-related deaths were encountered in 2012 (Stewart and Wild, 2014). Furthermore, the number of new cases and cancer-related deaths is expected to rise to 22 million and 13 million respectively per year in the next two decades. One of the defining characteristics of cancer is the rapid and uncontrollable proliferation of abnormal cells.

Radiation therapy is one of the 3 major treatment modalities for cancer with the other two being chemotherapy and surgery. About half of the cancer patients will receive radiation therapy at some point of their treatment. During radiation therapy, ionizing radiation, such as high-energy (MeV) photons or charged particles, deposit energy on the tumor site (Lawrence, Ten Haken, and Giaccia, 2008). The average energy deposited per unit mass is defined as the absorbed dose and is measured in units of Gray (1 Gy = 1 J/kg). Overall, the treatment goal is to reduce the tumor size or stall the growth rate by maximizing the dose delivered in the tumor site while at the same time minimizing the dose in surrounding healthy tissue and organs at risk (OAR).

It is well accepted that the biological effects of radiation result primarily from damage to the DNA. There are two forms of action that can cause damage to the DNA (Podgorsak et al., 2005): (i) direct action, defined as the direct deposition of energy to the DNA by charged particle tracks and (ii) indirect action defined as the indirect deposition of energy in the DNA by the process of water radiolysis and the creation of free radicals in the cell. Direct and indirect damage to the DNA will cause either single or double strand breaks. Single strand breaks occur more frequently, but they are usually repaired by the cell. Lethal events in the DNA occur more easily with double strand breaks, especially if the strand breaks occur in the same region. Direct action is responsible for about one third of the DNA damage, while indirect action is responsible for the other two thirds. Lethal events in the DNA will result in chromosome aberrations, mutations and eventually cell death.

Radiation damage in the DNA may be associated in different outcomes on the cell life cycle. In some cases it is associated with loss of functionality, while in others with loss of proliferative ability. As reference values, we can say that cell functionality is destroyed with a dose around 100 Gy, while loss of proliferative ability occurs around 2 Gy (Hall and Giaccia, 2006). For the purposes of radiation therapy, tumor cells need to stop proliferating, while healthy tissue cells need to preserve their functionality. Two important metrics are used to quantify the above: the tumor control probability (TCP) expresses the probability of controlling locally the tumor and the normal tissue complication probability (NTCP) expresses the probability of a healthy tissue experiencing functionality loss. Plotting TCP and NTCP in a dose-response curve allows us to identify a range of doses in which the TCP values are high (efficient tumor cell kill), while NTCP is relative low (no severe normal tissue complication). This constitutes the "therapeutic window" for dose prescription purposes (figure 1.1).

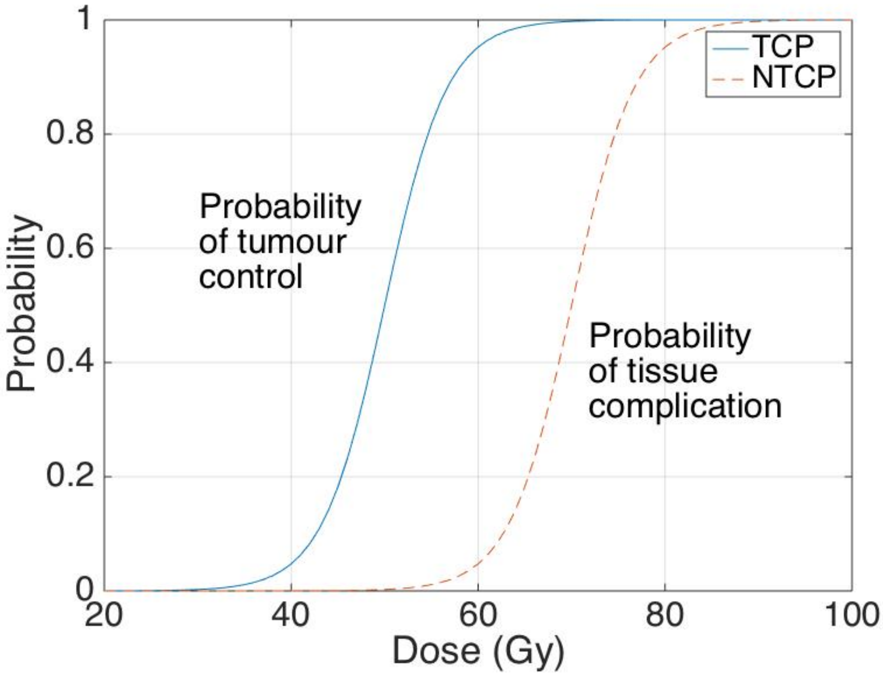

FIGURE 1.1: TCP and NTCP dose response curves. The therapeutic window is defined in the region where the TCP curve is high, while the NTCP curve remains low.

The radiation used to treat the tumor can be emitted either outside of the patient body, as in external beam radiotherapy (EBRT), or inside the body as in Brachytherapy. In the latter case radioactive sources are placed close to or within the tumor volume. The concept of EBRT appeared soon after the discovery of X-rays by Röntgen, 1896. In the first years, X-ray tubes were mainly used which provided only limited energies in the keV range. It was during the 1950s and the invention of the ^{60}Co teletherapy machines that provided the first beams in the MeV energy range (Podgorsak et al., 2005). The higher energy photon beams provided deeper penetration in soft tissue and thus better coverage of deep-seated tumors. The ^{60}Co machines were used for many years until they were gradually replaced by medical linear accelerators (LINACs). Medical LINACs are widely used today in most clinics around the world. The advantage of a LINAC is that it can generate both electron and photon beams with various energies from 4 MeV to 22 MeV. A typical modern LINAC is shown in figure 1.2.

FIGURE 1.2: A Varian Novalis® Tx linear accelerator (Varian Medical Systems, Palo Alto, CA, USA)

A LINAC accelerates electrons using non-conservative microwave radio-frequency (RF) fields in the range of 10^3 to 10^4 MHz (Podgorsak, 2010). The accelerated electrons are brought into the LINAC treatment head. The LINAC treatment head consists of several components which assist in producing and defining the photon fields (figure 1.3). First, the electron beam is incident on a target, usually composed of tungsten or copper. As they de-accelerate in the target, electrons emit Bremsstrahlung X-rays. The X-ray fluence distribution is mainly forward peaked. Traditionally, a flattening filter (FF) is placed on the beam line to flatten the beam according to the clinical needs.

However, in modern LINACs a flattening filter free (FFF) mode exists that increases the dose rate. Transmission ion chambers are used to monitor the beam output, flatness and symmetry continuously during treatment. The photon beam is collimated through various collimation levels: the primary collimator, secondary collimator (or jaws) and the micro-leaf collimator (MLC). The primary collimator is a fixed collimation system which defines the maximum field size. The jaws reside beneath the monitor chambers and they can dynamically move and shape different square or rectangular field sizes. Finally, the MLC resides just upstream of the exit of the treatment head and allows the shaping of arbitrary irregular field sizes. The purpose of beam collimation is to achieve maximum conformity of the radiation beam to the patient-specific tumor location, size and shape. Figure 1.3 presents a sketch of the treatment head components along with their relative positions.

Prior to the radiation treatment, a patient-specific treatment simulation needs to be carried out. This step ensures that the delivery is properly aimed at the target, while sparing OAR. As a first step of the process, computed tomography (CT) scans of the area to be treated are acquired. The patient's treatment position is also determined by skin marks or tattoos. These marks will be used to position the patient to exactly the same location during the treatment sessions. The radiation oncologist would then determine the location and extent of the clinical disease to be treated, along with the dose to be delivered, on the CT images. Critical structures surrounding the tumour should also be outlined and a maximum tolerance dose is prescribed for them, if needed.

As a next step, a computer calculation is carried out by the physicist or dosimetrist

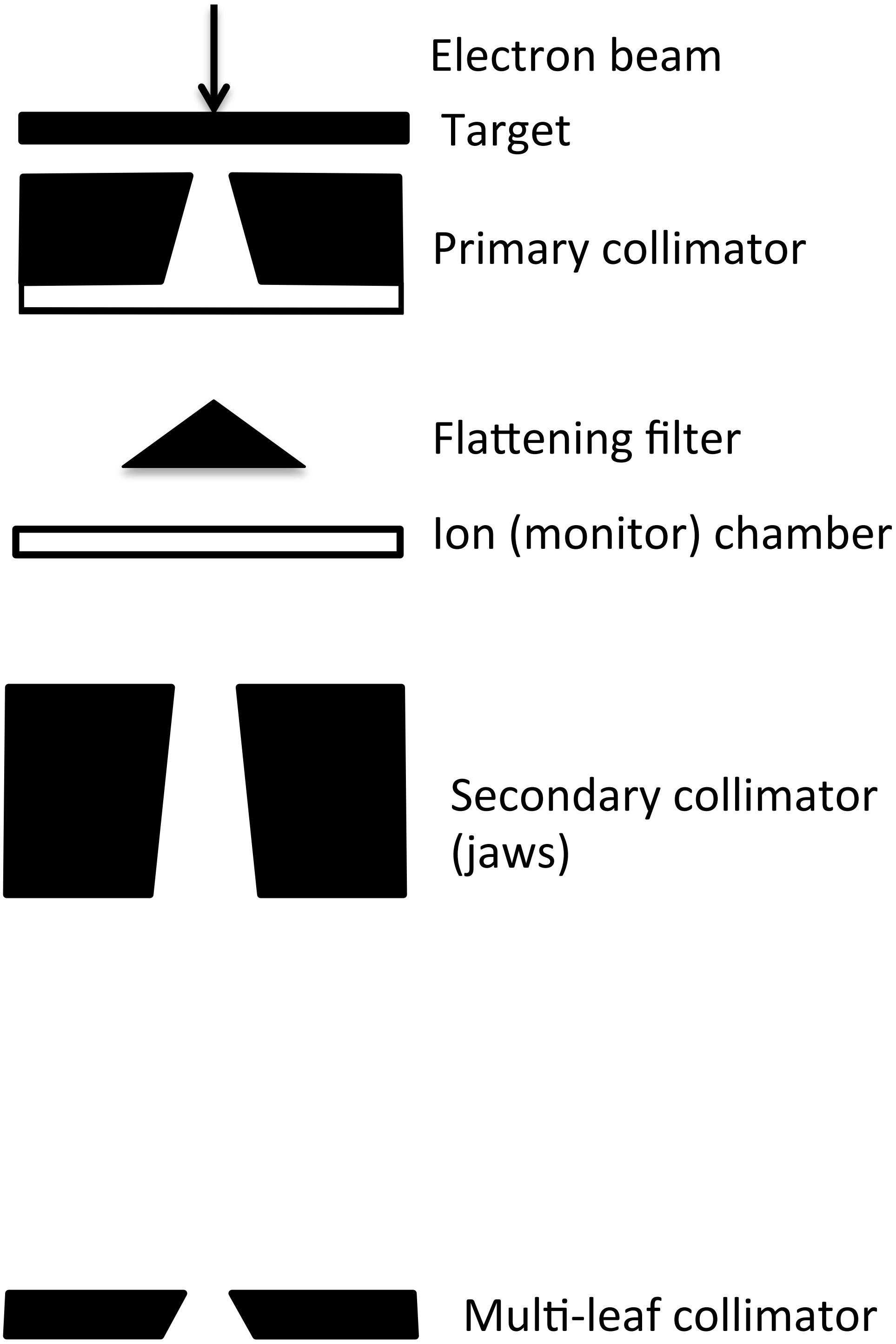

FIGURE 1.3: A typical linear accelerator head sketch including the main beam defining components.

to determine the appropriate arrangement of the radiation beams to satisfy the prescribed and tolerance dose limits. The dose calculations are most often performed with the usage of a beam model. The beam model simulates the photon and electron beam characteristics as they exit the LINAC treatment head, as well as the particle transport through the patient-specific geometry. Monte Carlo (MC) methods are generally considered as the most accurate algorithms for modeling the radiation beam. However, due to the intense computing resources needed for MC simulations, analytical beam models may be preferred.

An important responsibility of the medical physicist in the clinic is to ensure that the beam models in the treatment planning system (TPS) reproduce accurately the beam characteristics of the LINAC. This task is accomplished by a process called commissioning which is performed during LINAC installation. During this process a large set of dose measurements, most often performed in water, is used as an input to the TPS. The beam model parameters are then tuned accordingly in order to achieve an acceptable agreement with the measured data. After the accelerator commissioning the performance of the algorithms still needs to be validated on the actual patient treatment plan, especially in special radiotherapy procedures. In the following some special radiotherapy techniques are discussed (NCI, 2010).

- **Intensity Modulated Radiation Therapy (IMRT)**

  In IMRT the photon fluence is dynamically modulated by the MLC, using multiple small and irregular field sizes, in order to maximize the conformity of the dose distribution in the target (Bortfeld, 2006). IMRT follows an inverse treatment planning scheme. The optimization algorithm selects the optimal field sizes, shapes, angles and relative weights that respect the radiation oncologist's prescribed dose in the target as well as the tolerance doses at the OAR. However, an IMRT plan may result in delivering low doses in large volume regions, which has raised a concern regarding the possibility of inducing more secondary cancers compared to more conventional deliveries (Hall and Wuu, 2003).

- **Stereotactic Radiosurgery (SRS)**

  SRS refers to the delivery of high doses of radiation in small regions in the brain or spinal cord. It is usually performed in a single treatment session, therefore high precision is essential. For the SRS treatments head frames or other immobilization devices are commonly used.

- **Stereotactic Body Radiation Therapy (SBRT)**

  SBRT, also referred as Stereotactic Ablative Radiotherapy (SABR), delivers high doses of radiation in small regions outside the brain and the spinal cord, most often in lung and liver. Since these tumors are likely to move, due to body movements and breathing, SBRT is usually given in a few sessions (1 - 5).

1.2 Introduction to small field dosimetry

Small photon fields are often used during the delivery of IMRT, SRS or SBRT treatments. The delivery of small photon fields can be performed by specialized units such as the CyberKnife® robotic radiosurgery system (Accuray Inc., Sunnyvale, CA, USA) and the Leksell GammaKnife® (Elekta Instrument AB, Stockholm, Sweden) or even by conventional linear accelerators, such as the Varian Novalis® Tx equipped with high precision MLCs (BrainLab AG, Feldkirchen, Germany). Even though the above technological improvements have offered a high level of precision in the delivery of small radiation beams, several physics-based dosimetric issues are presented as the fields become gradually smaller. These issues lead to questioning of the actual accuracy of the measurements used for beam model commissioning. It is important to note that systematic errors introduced during commissioning will propagate to the beam model and thus will affect all subsequent calculations performed during patient-specific treatment planning.

To begin with, there is no clear definition of what constitutes a small field (Das, Ding, and Ahnesjö, 2008). Practically speaking a field smaller than 2×2 cm^2 can be considered small. More rigorously, small field conditions are considered to exist when one of the following effects becomes dominant (Aspradakis, 2010):

- The collimation system partially blocks the direct X-ray source as produced in the LINAC target. This effect is commonly referred to as *source occlusion*.
- Charged particles that were created within the field and scattered out of it are not replaced by an equal number of charged particles created outside of the field and scattered in. This effect is commonly referred to as *loss of charged particle equilibrium* (CPE).
- The detector resolution is large relative to the field size, which causes volume averaging effects or the detector is composed by non-water equivalent materials which results in particle fluence perturbations.

The first two effects are often defined as *beam-specific* and the last effect as *detector-specific*. Conventionally, in medical physics the dose is reported in water. This convention originates in the idea that the human body is mainly composed of water-like materials. For that purpose, the calibration procedures are always performed in water. However, there is no dosimeter that directly measures dose in water. Real detectors have finite sizes and non-water components. Detector- and field- specific corrections need to be applied to the measurements. The corrections can be generally classified as *component-specific* perturbation factors and *detector replacement* perturbation factors. The component-specific effects refer to the perturbations caused by the non-water components that surround the sensitive volume (or cavity) of the detector. The detector replacement perturbations refer to the sensitive volume or cavity where the signal is actually measured. As the cavity may also be composed of non-water materials, the incident energy fluence may be perturbed compared to the case where the cavity would have been composed purely of water. Furthermore, the cavity may be large enough that the delivered dose distribution within the cavity may not be uniform. This would lead to volume averaging effects. The above effects can be quantified using MC simulations, as shown by Wulff et al., 2010 and Bouchard et al., 2009a for air-filled ion chambers. Crop et al., 2009 observed that the perturbation factors may vary as the ion chamber moves laterally to off-axis positions.

A formalism was suggested for the dosimetry of small and non-standard fields by Alfonso et al., 2008. According to the suggested formalism a small static field can be measured accurately by any detector as long as an appropriate correction factor is applied. The correction factors can be determined by MC simulations of the dose deposited in the sensitive volume of the detector relative to the respective calculation at a point in water. For that purpose, the detector needs to be explicitly modeled following the technical drawings provided by the manufacturer. This approach has been followed by several investigators for the Cyberknife system and linear accelerators (Araki, 2006; Francescon, Cora, and Cavedon, 2008; Francescon, Cora, and Satariano, 2011; Cranmer-Sargison et al., 2011; Francescon et al., 2012; Czarnecki and Zink, 2013; Wagner et al., 2013). The above studies are focused on the derivation of a single correction factor on the central axis. However, off-axis positions may also need corrections, as the Crop et al., 2009 study has demonstrated for air-filled chambers.

An alternative approach suggested by the Alfonso formalism relies on the the derivation of the correction factors purely by experimental methods (Pantelis et al., 2010; Pantelis et al., 2012; Ralston et al., 2012). In such case, a dosimeter with properties close to water, such as polymer gels or radiochromic film, can be chosen as the reference dosimeter. Radiochromic film presents several features that make it a promising dosimeter for small fields including the near-to-water material composition and high spatial resolution. However, the calibration procedure, along with the film and scanner non-uniformities, most often result in much higher uncertainty levels compared to other dosimeters, especially in the low dose region (< 1 Gy) where the sensitivity drops significantly. The above issues are crucial for the measurement of stereotactic profiles, where low dose regions will unavoidably appear.

One of the most important beam parameters for small field beam modeling, is the electron source at the target level (figure 1.3) or the respective photon distribution generated in the target (Aspradakis, 2010). The electron source is rarely a pencil beam, but rather follows some Gaussian-like spatial distribution. The exact electron (or photon) source size and shape are most often unknown for a given accelerator. In most beam models the source is assumed to follow Gaussian distribution and the full width at half maximum (FWHM) of the source is iteratively tuned based on a "trial-and-error" procedure until a good agreement is observed between calculations and measurements. Even though such an approach might be sufficient for larger fields, it appears problematic for small fields. As the collimator settings are gradually decreased, the portion of the source that is "visible" through the aperture is decreased (source occlusion). Larger sources are expected to present a more dominant source occlusion effect for the same collimator settings. An increased source occlusion effect will result in a drop of the dose output, a widening of the dose profile penumbra and an apparent increase in the field size. Therefore, the dosimetry in small fields is much more sensitive to the variations of the source. These effects could potentially be quantified for determination of the source size (Zhu, Bjärngard, and Shackford, 1995; Wang and Leszczynski, 2007). However, one should keep in mind that similar effects may be observed due to detector-specific effects as described earlier. Therefore, it is not clear if the observed dose characteristics can be attributed to the source occlusion or detector measurements.

Several researchers have tried to bypass the above problem by attempting to directly measure the source distribution using other methods. The most accurate technique suggested to date utilizes a rotating "slit" collimator and a CT reconstruction method (Munro, Rawlinson, and Fenster, 1988; Jaffray et al., 1993; Caprile and Hartmann, 2009). However, this device is difficult to handle and use routinely in the clinic.

Currently, there is no method for the direct reconstruction of the source distribution utilized in the clinic.

1.3 Thesis outline and objective

The objective of the thesis is to provide data and develop methods that can potentially improve the dosimetry in small photon radiation fields. Specifically this work focuses on two important areas in small field dosimetry: (i) the response of modern small field dosimeters on dose output and profile measurements used during beam model commissioning and (ii) the direct reconstruction of the LINAC source distribution using a clinical experimental set-up.

For the first part, a detailed MC beam model was commissioned for use in small photon fields. The importance of including the detector model in the calculations and using large or small field sizes during the beam model commissioning was investigated. The response of a liquid ionization, diode, scintillator and synthetic diamond was studied in small fields. The purpose of this step was to investigate which detector requires the smallest corrections for the dosimetry in small fields. The component-specific and detector-replacement perturbation effects were also studied in order to understand the origin of the corrections and possibly suggest modifications of the detector designs that would improve their performance.

For the second part, the objective was to develop a method that would reconstruct the source distribution without the need of using any correction-dependent detectors or an iterative "trial-and-error" tuning procedure. Furthermore, we required two restrictions to be respected: (i) the method should include a simple experimental set-up that could easily be performed in a clinical environment and (ii) no prior assumptions should be made for the source distribution. The suggested reconstruction method was based on a maximum-likelihood expectation maximization (MLEM) technique and fluence profile measurements. For the fluence profile measurements radio-chromic film and a high density material were used.

As described in the previous section, radio-chromic film exhibits high uncertainty levels, especially in the low dose region where the sensitivity drops significantly. We hypothesized that there could be sensitivity gains in the low dose region if the films are scanned in the reflection mode instead of the transmission mode. An investigation on the uncertainty, accuracy and resolution of the reflection mode was performed and compared to the transmission mode. A calibration protocol was suggested which was subsequently used as part of the method in the direct source reconstruction experimental measurements.

The thesis consists of four manuscripts, two published, one accepted for publication and one to be submitted for review. Chapter 2 presents fundamental concepts in radiation physics and dosimetry. Chapter 3 extensively reviews previous research in small photon fields. Chapter 4 presents published work on the correction, perturbation and modification of modern small field dosimeters. Chapter 5 presents experimental work on the accuracy of plastic scintillation dosimeters. Chapter 6 presents published work on a calibration protocol for low dose radiochromic film dosimetry using reflection scanning. Chapter 7 presents published work on the development of a source reconstruction method for clinical linear accelerators. Chapter 8 derives conclusions from this work and suggests future directions of research.

1.4 Contribution of authors

The first manuscript, “On the correction, perturbation and modification of small field detectors in relative dosimetry”, presents published work mainly conducted by Pavlos Papaconstadopoulos. Dr. Frederic Tessier assisted with the Monte Carlo calculations and detector modeling. Dr. Jan Seuntjens provided general guidance and supervision of the study.

The second manuscript, “Experimental investigation on the accuracy and precision of plastic scintillation dosimeters and on the spectral discrimination calibration method in small photon fields ”, presents experimental work mainly conducted by Pavlos Papaconstadopoulos. Dr. Louis Archambault provided the prototype plastic scintillator (CHUQ PSD) dosimeter and assisted with the measurements, data analysis and interpretation. Dr. Jan Seuntjens provided general guidance and supervision of the project.

The third manuscript, “A protocol for EBT3 radiochromic film dosimetry using reflection scanning ”, presents published work mainly conducted by Pavlos Papaconstadopoulos. Dr. Gyorgy Hegyi assisted with the resolution analysis measurements. Dr. Jan Seuntjens provided supervision of the work and assisted with review comments. Dr. Slobodan Devic suggested the original idea, assisted with measurements and data analysis and provided general guidance on the project.

The fourth manuscript, “Direct reconstruction of the source intensity distribution of a clinical linear accelerator using a maximum likelihood expectation maximization algorithm ”, presents published work mainly conducted by Pavlos Papaconstadopoulos. Dr. Ives Levesque assisted with the theory and implementation of the imaging algorithm and de-blurring kernel. Robert Maglieri contributed in the implementation of the MLEM algorithm and assisted with the uncertainty estimation. Dr. Jan Seuntjens provided general guidance and supervision.

Chapter 2

Introduction to radiation dosimetry

2.1 Fundamental concepts in dosimetry

2.1.1 Particle and energy fluence

Assuming a finite sphere of volume V surrounding a point P, let N be the expectation value of particles striking the sphere (figure 2.1). If we reduce the sphere to an infinitesimal volume dV with a cross-sectional area of da we can define the particle fluence as the quotient of the differential of dN by da (Attix, 2008):

$$\Phi = \frac{\mathrm{dN}}{\mathrm{da}} \tag{2.1}$$

Similarly if we define R to be the expectation value of the total kinetic energy incident on the sphere, then we can define the energy fluence as the quotient of dR to da (Attix, 2008):

$$\Psi = \frac{\mathrm{dR}}{\mathrm{da}} \tag{2.2}$$

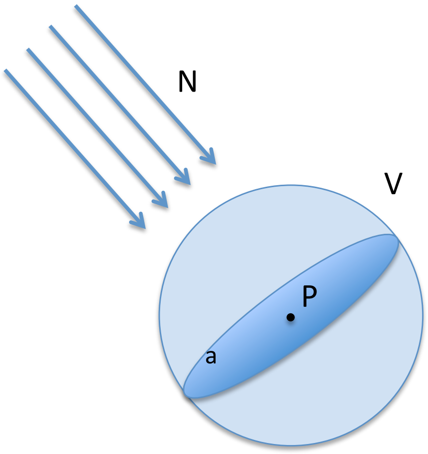

FIGURE 2.1: Particle fluence defined as the number of particles striking the cross-sectional area of a sphere.

Assuming that the particle beam is monoenergetic with energy E, then the energy fluence can be linked to the particle fluence as follows:

$$\Psi = \mathrm{E}\Phi \tag{2.3}$$

However, in practical cases particles are not monoenergetic, but rather follow an energy distribution. In that case the particle fluence can be described as a function of energy, $\phi(\mathrm{E}) = \frac{\mathrm{d}\Phi}{\mathrm{dE}}(\mathrm{E})$. The total particle fluence could then be determined as:

$$\Phi = \int_0^{\mathrm{E_{max}}} \phi(\mathrm{E})\mathrm{dE} \tag{2.4}$$

In this case the total energy fluence would be written also as:

$$\Psi = \int_0^{\mathrm{E_{max}}} \phi(\mathrm{E})\mathrm{EdE} \tag{2.5}$$

Finally, the particle fluence can also be expressed as a function of solid angle $\mathrm{d}\Omega = \sin(\theta)\mathrm{d}\theta\mathrm{d}\beta$. In that case the total fluence would be expressed as (Attix, 2008):

$$\Phi = \int_0^{\pi}\int_0^{2\pi}\int_0^{\mathrm{E_{max}}} \phi(\theta,\beta,\mathrm{E})\sin(\theta)\mathrm{d}\theta\mathrm{d}\beta\mathrm{dE} \tag{2.6}$$

2.1.2 Kerma, exposure and dose

As photons interact with matter part of their energy is transferred to charged particles. The term *energy transferred*, ϵ_{tr}, is formally defined as the kinetic energy transferred to charged particles within the volume V, regardless of how the charged particles will subsequently lose their energy (Attix, 2008). The kinetic energy released per unit mass (kerma), expressed in units of Gy ($1\,\mathrm{Gy} = 1\frac{\mathrm{J}}{\mathrm{kg}}$) can be defined as:

$$\mathrm{K} = \frac{\mathrm{d}\overline{\epsilon_{\mathrm{tr}}}}{\mathrm{dm}} \tag{2.7}$$

The energy transferred to the charged particles can be lost in the material either through collisions or radiative losses. The latter case may involve bremsstrahlung or annihilation in-flight photons that are most likely to leave the volume V. Therefore, we can separate kerma into two components: collisional kerma, $\mathrm{K_{col}}$, referring to the energy transferred to charged particles, but lost only by collisions (net energy transferred, $\epsilon^{\mathrm{n}}_{\mathrm{tr}}$) and radiative kerma, $\mathrm{K_{rad}}$, which refers to the remaining energy lost through radiative events:

$$\mathrm{K} = \mathrm{K_{col}} + \mathrm{K_{rad}} \tag{2.8}$$

The most fundamental quantity in radiation dosimetry and medical physics is the absorbed dose. Absorbed dose is defined as the total energy imparted, ϵ, per unit mass in volume V by charged particles:

$$\mathrm{D} = \frac{\mathrm{d}\bar{\epsilon}}{\mathrm{dm}} \tag{2.9}$$

Dose is measured in units of Gy, similar to the kerma. In contrast to the quantity of kerma, which is defined only for indirect ionizing radiation, such as photons, dose is used for any particle beam.

Another important quantity in dosimetry is the exposure, X, defined as the amount of charge, Q, of ions of one sign produced in a volume V of dry air of mass dm (Attix, 2008):

$$\mathrm{X} = \frac{\mathrm{dQ}}{\mathrm{dm}} \tag{2.10}$$

Exposure is measured in R (Röngten) equal to $2.58\,10^{-4}\,\frac{C}{kg}$. Exposure can be seen as the ionization equivalent of collisional kerma in air, $(\mathrm{K}_{\mathrm{col}})_{\mathrm{air}}$.

2.1.3 Photon interaction coefficients

If we consider N_0 photons incident perpendicularly on a material of thickness L , the number of particles passing through the material without interacting (N) is given by the law of exponential attenuation (Podgorsak, 2010):

$$\mathrm{N} = \mathrm{N}_0 \mathrm{e}^{-\mu \mathrm{L}} \tag{2.11}$$

The coefficient μ [cm^{-1}], referred to as the linear attenuation coefficient, expresses the probability that a photon interacts per unit length. Dividing μ by the material density ρ we define the mass attenuation coefficient, $\frac{\mu}{\rho}$ [$\frac{\mathrm{cm}^2}{\mathrm{g}}$] (Podgorsak, 2010). It should be noted that the exponential law is strictly applied only in narrow beam geometries, meaning that photons that have scattered out of the initial path track or absorbed in the material, are not counted.

The mass energy transfer coefficient, $\frac{\mu_{tr}}{\rho}$, is defined as (Attix, 2008):

$$\frac{\mu_{\mathrm{tr}}}{\rho} = \frac{\mu}{\rho}\frac{\mathrm{E}_{\mathrm{tr}}}{\mathrm{E}} \tag{2.12}$$

The mass energy transfer coefficient represents the fraction of the photon energy that, upon interaction, is transferred as kinetic energy to the charged particles per unit mass. Therefore it links the concept of energy fluence to kerma:

$$\mathrm{K} = \Psi\frac{\mu_{\mathrm{tr}}}{\rho} \tag{2.13}$$

Finally the mass energy absorption coefficient, $\frac{\mu_{\mathrm{en}}}{\rho}$, represents the fraction of the photon energy that, upon interaction, is transferred as kinetic energy to the charged particles and then lost through collisional losses. Therefore, it links the concept of energy fluence to collisional kerma (Attix, 2008):

$$\mathrm{K}_{\mathrm{col}} = \Psi\frac{\mu_{\mathrm{en}}}{\rho} \tag{2.14}$$

The mass energy absorption coefficient is always a fraction of the mass transfer coefficient and the two can be linked by the following equation:

$$\frac{\mu_{\mathrm{en}}}{\rho} = \frac{\mu_{\mathrm{tr}}}{\rho}(1 - \overline{\mathrm{g}}), \tag{2.15}$$

where $\overline{\mathrm{g}}$ represents the average fraction of energy lost by charged particles via radiative losses (Podgorsak, 2010). Since collisional losses will result in ionizations, the concepts of exposure and collisional kerma in air are linked as:

$$\mathrm{X} = \frac{\Psi(\frac{\mu_{\mathrm{en}}}{\rho})_{\mathrm{air}}}{(\frac{\overline{\mathrm{W}}}{\mathrm{e}})_{\mathrm{air}}} = \frac{(\mathrm{K}_{\mathrm{col}})_{\mathrm{air}}}{(\frac{\overline{\mathrm{W}}}{\mathrm{e}})_{\mathrm{air}}}, \tag{2.16}$$

where $\frac{\overline{W}}{e}$ is the mean energy expended per ion pair. Its value for dry air is considered constant and equal to 33.97 eV per ion pair (or $\frac{\mathrm{J}}{\mathrm{C}}$) . The last equation justifies the statement that exposure is the ionization equivalent of collisional kerma in air.

2.1.4 Charged particle equilibrium

Charged particle equilibrium (CPE) exists for the volume V, if each charged particle of a given energy leaving the volume is replaced by an identical particle of the same energy entering the volume (Attix, 2008). As described earlier, the net energy transferred, ϵ_{tr}^{n}, refers to the energy transferred to charged particles within volume V and subsequently lost through collisions. On the other hand the energy imparted, ϵ, refers to the total energy imparted in volume V. As a charged particle is generated within the volume, it may partly impart its energy inside the volume and partly outside of it. Therefore, in general, the relationship $\epsilon < \epsilon_{tr}^{n}$ is satisfied. However, under conditions of CPE the energy imparted outside of the volume will be replaced (on average) by an equal amount of energy imparted by a charged particle generated outside the volume V and entering in it (figure 2.2). In such case $\overline{\epsilon} = \overline{\epsilon_{tr}^{n}}$ and therefore:

$$\mathrm{D} \overset{\mathrm{CPE}}{=} \mathrm{K}_{\mathrm{col}} \tag{2.17}$$

The importance of the above equation lies in the fact that it links the concept of absorbed dose to collisional kerma and hence to energy fluence. If the volume V is composed by air then equation 2.16 can be expanded as:

$$\mathrm{D}_{\mathrm{air}} \overset{\mathrm{CPE}}{=} (\mathrm{K}_{\mathrm{col}})_{\mathrm{air}} = \mathrm{X}\left(\frac{\overline{\mathrm{W}}}{\mathrm{e}}\right)_{\mathrm{air}} \tag{2.18}$$

Thus, by measuring the charges created in a defined volume and mass of air we can determine the absorbed dose within the volume under conditions of CPE.

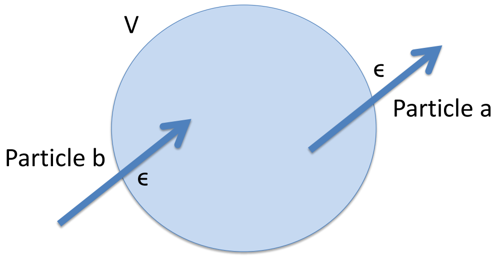

FIGURE 2.2: An example of charged particle equilibrium in a cavity. Particle a leaves the cavity and deposits energy ϵ outside of it. Particle b enters the cavity with energy ϵ and deposits it in the volume. Overall, the same energy is deposited in the cavity as if particle a had imparted all of its transferred energy in the volume.

2.1.5 Stopping power and cavity theory

The purpose of radiation dosimetry is to measure the dose in a medium, that being most of the times water as a close approximation to the human body. However, experimentally it is not easy to have a dosimeter with the same material properties as water. The dosimeter's reading refers to the dose deposited in the medium of its own active volume. Thus, for an ionization chamber the dose is most often deposited in air and a final conversion is needed from air to dose in water.

A fundamental concept used in cavity theory is the stopping power (Attix, 2008). The linear stopping power, S, is defined as the energy lost by a charged particle per unit length:

$$\mathrm{S} = \frac{\mathrm{dE}}{\mathrm{dl}}\left[\frac{\mathrm{MeV}}{\mathrm{cm}}\right] \tag{2.19}$$

Dividing the linear stopping power with the density of the medium, ρ, we can define the mass stopping power:

$$\frac{\mathrm{S}}{\rho} = \frac{1}{\rho}\frac{\mathrm{dE}}{\mathrm{dl}}\left[\frac{\mathrm{MeVcm^2}}{\mathrm{g}}\right] \tag{2.20}$$

The mass stopping power can be further classified according to the type of energy loss to collisional, $\mathrm{S_{col}}$, and radiative, $\mathrm{S_{rad}}$, mass stopping power (Podgorsak, 2010):

$$\frac{\mathrm{S}}{\rho} = \left(\frac{\mathrm{S}}{\rho}\right)_{\mathrm{col}} + \left(\frac{\mathrm{S}}{\rho}\right)_{\mathrm{rad}} \tag{2.21}$$

We can assume that collisional losses are mainly depositing dose locally (Podgorsak, 2010). Thus, if there is a fluence of particles, $\phi(E)$, crossing a cavity, such as volume V in figure 2.1, the dose deposited in the medium of the cavity can be derived as:

$$D = \int_0^{E_{\max}} \phi(E)\left(\frac{S(E)}{\rho}\right) dE, \tag{2.22}$$

if bremsstrahlung events are not considered significant and secondary electrons are assumed not to leave the local region. At the same time the mean stopping power can be calculated as:

$$\left(\frac{\overline{S}}{\rho}\right) = \frac{\int_0^{E_{\max}} \phi(E)\frac{S}{\rho}(E)dE}{\int_0^{E_{\max}} \phi(E)dE} = \frac{D}{\Phi}, \tag{2.23}$$

where Φ is the total particle fluence. Therefore, the dose in the medium can be expressed as:

$$D_{\text{med}} = \left(\frac{\overline{S}}{\rho}\right)_{\text{med}} \Phi_{\text{med}} \tag{2.24}$$

If the cavity has a different medium (e.g. air) then the ratio of the doses in the two media would be written as (Attix, 2008):

$$D_{\text{cav}}^{\text{med}} = \left(\frac{\overline{S}}{\rho}\right)_{\text{air}}^{\text{med}} \Phi_{\text{cav}}^{\text{med}} \tag{2.25}$$

Equation 2.25 allows us to calculate the dose in the medium, if the dose in the cavity medium, mean stopping power ratios and particle fluence ratios are known. Unfortunately, the particle fluence can not be measured. However, if we assume that the cavity is small, relative to the electron range, and that there are not any particles generated in the cavity, but only those crossing it, we can assume that the particle fluence is not perturbed by the cavity and thus $\Phi_{\text{cav}}^{\text{med}} \approx 1$. The above two restrictions are commonly referred to as Bragg-Gray conditions and a cavity that respects them as a Bragg-Gray cavity (Attix, 2008). Thus, under Bragg-Gray conditions we can measure the dose in the medium as:

$$\mathrm{D}_{\mathrm{med}} = \mathrm{D}_{\mathrm{air}} \left(\frac{\overline{\mathrm{S}}}{\rho} \right)_{\mathrm{air}}^{\mathrm{med}} \tag{2.26}$$

2.1.6 Large and general cavity theories

In the case where the cavity is large enough so that all the charged particles are generated in the cavity and their range does not allow them to exit, we have the case of a large cavity. In such case, the dose in the medium can be calculated directly by the photon mass energy absorption coefficients. We can also assume that the energy fluences do not vary significantly by changing the medium and thus $\Psi_{\mathrm{cav}}^{\mathrm{med}} \approx 1$ (Attix, 2008).

$$\mathrm{D}_{\mathrm{med}} = \mathrm{D}_{\mathrm{cav}} \left(\frac{\mu_{\mathrm{en}}}{\rho} \right)_{\mathrm{cav}}^{\mathrm{med}} \Psi_{\mathrm{cav}}^{\mathrm{med}} \approx \mathrm{D}_{\mathrm{cav}} \left(\frac{\mu_{\mathrm{en}}}{\rho} \right)_{\mathrm{cav}}^{\mathrm{med}} \tag{2.27}$$

It is possible for the cavity neither to be that small to satisfy the Bragg-Gray conditions neither that large so it would be a pure photon detector. In such intermediate size cavities a mixed model can be used such as the one proposed by Burlin, 1966:

$$\mathrm{D}_{\mathrm{med}} = \mathrm{D}_{\mathrm{cav}} \left[\beta \left(\frac{\overline{\mathrm{S}}}{\rho} \right)_{\mathrm{cav}}^{\mathrm{med}} + (1-\beta) \left(\frac{\mu_{\mathrm{en}}}{\rho} \right)_{\mathrm{cav}}^{\mathrm{med}} \right], \tag{2.28}$$

where β expresses the fraction of the dose that is deposited by particles crossing the cavity and $1-\beta$ is the fraction of the dose that originated by photon interactions in the cavity. Determining the parameter β is challenging and it will depend on the detector design geometry and material used.

2.1.7 Range

The range of a charged particle, R, refers to the maximum distance the particle can reach in a medium (Podgorsak, 2010). It depends on the initial energy of the particle, its mass and charge and the composition of the material. One of the most common range definitions used in radiation dosimetry and safety is based on the continuously slowing down approximation (CSDA). According to this approximation, particles are assumed to move on straight lines and lose gradually their initial energy. The CSDA range can be calculated by integration of the inverse stopping power from 0 to the initial particle energy $\mathrm{E_0}$:

$$\mathrm{R_{CSDA}[cm]} = \int_0^{\mathrm{E_0}} \frac{\mathrm{dE}}{\mathrm{S(E)}} \tag{2.29}$$

It should be emphasized that $\mathrm{R_{CSDA}}$ is not a very accurate approximation for light charged particles, such as electrons, as these will deflect significantly from their initial track due to multiple Coulomb scattering. However for shielding purposes the CSDA concept is most often an adequate approximation.

2.2 Detectors

In this section a number of the most important detectors will be presented with emphasis to the systems most commonly used in small radiation fields.

2.2.1 Ionization chambers

Air-filled ionization chambers are probably the most common dosimeters used in a clinical environment. They can be used for both reference and relative dosimetry. An ion chamber is composed by an air-filled cavity surrounded by a solid wall. Upon irradiation electrons are generated in the wall and cross the cavity. Ionizations in the gas result in electron-ion pairs which eventually are collected by a an electrode pair. Operating voltages may range from 100 to 800 V. Assuming that CPE exists, the collected charge can be related to the dose in the medium using cavity theory :

$$\mathrm{D_{med}} = \frac{\mathrm{Q}}{\mathrm{m_{air}}} \left(\frac{\overline{\mathrm{W}}}{\mathrm{e}}\right)_{\mathrm{air}} \left(\frac{\overline{\mathrm{S}}}{\rho}\right)_{\mathrm{air}}^{\mathrm{med}} \tag{2.30}$$

As the quantity of interest is dose in water it is advantageous the wall medium be made from water-like materials. Ionization chambers can be made in a variety of shapes (cylindrical, parallel plate etc) and volume sizes. However, as the size becomes small the resulting signal-to-noise ratio is decreased significantly, raising practical limitations in the maximum spatial resolution that can be achieved with ionization chambers. For that reason air-filled ionization chambers are not generally recommended for small fields as they are expected to present a significant volume averaging effect. At the same time the electrode materials most often composed by aluminum or steel may also perturb the beam.

A liquid-filled ionization chamber has been proposed (Wickman, 1974) and commercially developed by PTW (microLion 31018). The sensitive volume in this detector is filled with iso-octane liquid with density values close to water. The signal-to-noise ratio is expected to be improved which allows the reduction of the cavity dimensions and makes the dosimeter more suitable for small fields. However, ionization recombination effects are not very well understood in liquids and may result in dose-rate dependencies. For that purpose a high voltage of 800 V is suggested to be applied on this detector along with appropriate corrections (Chung, Davis, and Seuntjens, 2013).

2.2.2 Diodes

Diodes are often used for relative photon beam dosimetry (McKerracher and Thwaites, 2002; Sauer and Wilbert, 2007). They can be manufactured in very small sizes while at the same time offering high sensitivity. Most commonly the manufacturing process involves lightly doping a pure silicon substrate to become either n-type or p-type and then heavily doping with impurities of the opposite type in the surface region to form a p-n junction. A region of steep charge gradient and strong electric field is created which is commonly referred to as the depletion region (Zhu and Saini, 2009). The depletion region in silicon diode detectors varies but often is found to be about 50-60 μm thick and about 1-2 mm wide.

The silicon substrate is expected to cause an over- response when exposed in low energy photon beams, such as in the profile and depth dose tails of large fields used in radiotherapy. To compensate for this, some diodes have a high atomic number and density shield that absorbs these low energy photons. In small fields it has been reported that high density materials surrounding the cavity result in an over-response (Francescon, Cora, and Satariano, 2011). Therefore, unshielded diodes are in general preferred over shielded diodes.

It is important to note, that even though a diode's sensitive volume is physically small it should not be considered a small cavity since the range of the electron in high density materials is also significantly smaller. This suggests that the absorbed dose should be more appropriately modeled using a general cavity theory (Burlin, 1966), where part of the dose originates from photons interacting directly in the sensitive volume and creating charged particles and part of the dose originates from high energy electrons crossing the cavity (Yin, Hugtenburg, and Beddoe, 2004; Eklund and Ahnesjö, 2009).

2.2.3 Diamond detectors

Natural diamond detectors are attractive dosimeters mainly due to their near-to-water material composition. They exhibit high sensitivity and can be manufactured in small volumes (Heydarian, Hoban, and Beddoe, 1996; Laub, Kaulich, and Nüsslin, 1999). However, the major disadvantage with natural diamonds is that they can not easily be manufactured in a reproducible manner (De Angelis et al., 2002). Furthermore, they present dose rate dependencies, are significantly more expensive than other dosimeters and if biased incorrectly they may be damaged. The only commercial natural diamond detector available (PTW Riga type 60003) is no longer manufactured.

An interesting recent development is a synthetic diamond based on chemical vapor deposition (CVD) which promises low dose rate dependence and lower manufacturing cost than the natural diamond. The detector consists of a single crystal intrinsic layer deposited on a high pressure, high temperature diamond substrate. The dosimeter acts as a diamond-based Schottky-barrier photodiode and operates at zero bias voltage. Ciancaglioni et al., 2012 has characterized the detector in photon beams.

2.2.4 Scintillators

Plastic scintillator dosimeters (PSD) were first suggested by Beddar, Mackie, and Attix, 1992a and Beddar, Mackie, and Attix, 1992b as near-water equivalent dosimeters. PSDs present similar densities and atomic numbers to water and can be manufactured in small sizes. Thus, in principle, they should exhibit minimal perturbations under all conditions. A PSD system is composed by the scintillating probe which emits light upon irradiation, an optical fiber that transfers the light and a photodetector that collects the signal (Beaulieu et al., 2013).

The major drawback of PSDs is the Cherenkov light that is produced in the plastic by charged particles traveling faster than the speed of light in the medium. The charged particles start to polarize the medium which consequently results in the emission of visible light during the relaxation process (Beaulieu et al., 2013). The Cherenkov emission intensity is highest in the lower part of the visible spectrum. The Cherenkov light produced will depend on the length of irradiated fiber and thus its effect may vary depending on the irradiation conditions.

Several methods have been suggested for removing the Cherenkov signal. One of the first methods, originally suggested by Beddar, Mackie, and Attix, 1992a involves two fibers: one with the scintillation volume and the other without any scintillation volume. The latter fiber can be used as a reference fiber for measurements of the pure Cherenkov signal which is subsequently subtracted from the scintillation measurements. An alternative solution involves using an air-core fiber instead of a plastic fiber, which is not expected to create any Cherenkov light (**lambert2008Cherenkov**). De Boer, Beddar, and Rawlinson, 1993 suggested an optical filtering method so that the lower wavelengths, where Cherenkov mainly exists, are filtered out of the signal. Clift, Johnston, and Webb, 2002 proposed separating the Cherenkov to scintillation signal by temporal methods using a scintillation material with much longer decay time.

Perhaps the most practical method suggested to date is the spectrum discrimination, or chromatic removal, technique, originally suggested by Fontbonne et al., 2002. The main idea consists of measuring the signal from two different spectral regions under conditions that maximize and minimize the portion of the fiber irradiated. From these measurements the ratio of the Cherenkov emission between the two spectral regions can be determined, commonly referred as the Cherenkov Light Ratio (CLR). The CLR can be used subsequently, during measurements, to account for the relative Cherenkov response differences seen in the two spectral regions.

2.2.5 Radiochromic film

Radiochromic film is often used for commissioning and IMRT quality assurance measurements in the clinic. Some of its most advantageous features include the water equivalence, high spatial resolution, minimal energy dependence and the direct measurement of the full 2-D dose distribution (Devic, 2011). The introduction of the GAFCHROMIC EBT model (International Specialty Products, Wayne, NJ) increase substantially the sensitivity in the clinically important dose range of 0 - 8 Gy. However, the dose response is non-linear and a calibration procedure is needed prior to measurements. During calibration a set of film pieces are irradiated to known dose levels and a fitting optimization process is followed. Films can be scanned using a flat-bed document scanner and the Red (R), Green (G) and Blue (B) pixel color values are extracted (Devic et al., 2005). Most often the transmission scanning mode is used using the red color which exhibits the highest sensitivity. Prior to readout the films need to be left for 8 - 24 hrs for self-development. However, several sources of uncertainty exist mainly due to non-uniformities of the scanning process which reduce the overall accuracy and precision of the dosimeter. Such uncertainties may exceed 6% at the 1 Gy level (Hartmann, Martišíková, and Jäkel, 2010) and often are much higher for low dose regions such as the ones present in dose profiles.

2.3 Monte Carlo calculations

The Monte Carlo (MC) method is a category of computational algorithms that uses random sampling of known probability distributions to solve a complex physical or mathematical problem (Chetty et al., 2007). In the case of radiation transport such a technique can be utilized to simulate the charged or uncharged particle transport in a medium. For that purpose a pseudo-random number generator is used to sample physical quantities of interest from known probability distributions. If the process is repeated for a large number of histories, the average value of macroscopic quantities, such as fluence or dose, can be estimated (Rogers and Bielajew, 1990). The MC method is generally considered to be the most accurate numerical method for radiation dosimetry purposes. Even though it is crucial to validate the accuracy of the algorithms by measurements, MC methods can even offer us answers not accessible by other means, e.g. how many times did Compton scattering occur for a photon.

In the case of photon transport the algorithm starts by determining first the distance to the next interaction and the type of interaction (e.g. photoelectric, compton or pair production) by random sampling. The final energy and direction of the particle are then determined by sampling the appropriate energy and angular distribution and the algorithm continues in a similar fashion to the next event (Rogers and Bielajew, 1990). During the simulation of a particle transport a quantity of interest, such as energy imparted in a cavity, can be scored. In the case of electrons the simulation will soon become computationally intensive. This is because electrons will suffer a large number of elastic scattering events even in thin and low density materials. For that purpose a condensed-history (CH) technique is most often applied (Berger, 1963). The CH technique is based on the idea that a large number of scattering events can be grouped together in a single step. Each electron track is then decomposed to a series of discrete steps. The energy loss and angular deflection can be calculated after each step. One can significantly speed-up the calculation if a larger electron step is chosen. However, very large steps will limit the accuracy of the algorithm and the user needs to decide what is the level of accuracy needed in each case.

If a particle reaches an energy below which no significant dosimetric changes are observed then there is a benefit to stop the calculations and deposit the remaining energy locally. This energy threshold is referred as the cut-off energy. Another reason for introducing a cut-off energy threshold is that uncertainties in the cross-section data increase significantly for low energies.

2.3.1 BEAMnrc/EGSnrc

BEAMnrc is a general purpose code to simulate photon and electron radiotherapy beams in the energy range of 1 keV to 30 MeV (Rogers et al., 1995). The physics for simulating the radiation transport are simulated at the backend by the EGSnrc Monte Carlo code (Kawrakow and Rogers, 2000).

The design philosophy behind BEAM is that a linear accelerator can be modeled by a series of component modules (CMs). A CM follows some abstract geometry class that mimics the general shape and design of different linear accelerator components. For example the CM SLABS defines a set of parallel slabs that can be used to model the different compartments of the target. A wide variety of CMs exist and often the same CM type can be used for different accelerator components. The accelerator is created by placing in order each CM along the z-axis. The electron source is always considered to start at z=0 (figure 1.3).

After the abstract accelerator has been defined, the user needs to input the specific geometric and material characteristics for each CM as well as various source parameters. In the SLABS example, the user should provide information on how many slabs exist in the CM, their thickness and material composition. This information can be provided by the manufacturer or measured directly on the linac, if possible. However, there may be some information that is not available. These parameters may include: (i) the source distribution and size, (ii) the energy and (iii) the angular spread of the electrons incident on the target as well as (iv) the exact field openings as defined by the jaws or MLC. The above parameters are often tuned based on experimental measurements.

The BEAMnrc simulation can provide as an output a phase-space file at any plane selected by the user. The output plane always crosses perpendicularly the z-axis. The phase-space file includes the properties of all particles crossing the selected plane. These properties include the lateral position (X,Y), the energy (E), the charge (IQ), the direction cosines (U,V), the statistical weight (WT), the position of last interaction (ZLAST) and LATCH. LATCH is a history tag. It can provide information such as at which CMs the particle passed or interacted with. Alternatively to a phase-space file, the BEAMnrc simulation output can be used directly as an input to a dose calculation engine such as the DOSXYZnrc or egs_chamber code.

2.3.2 DOSXYZnrc

DOSXYZnrc is a EGSnrc-based dose calculation code (Walters, Kawrakow, Rogers, et al., 2005). The photon and electron transport is performed in a 3-D Cartesian phantom which is composed by rectangular-shaped voxels. The voxel size can change independently on each dimension according to the needed resolution during the simulation. The material properties can also vary for each voxel. There are a number of sources that can be used as an input to the DOSXYZnrc code including a phase-space file incident on any angle or a full BEAMnrc treatment head simulation.

2.3.3 egs_chamber and cavity

The *egs_chamber* code is based on the *cavity* code, an EGSnrc-based user code which allows the calculation of dose in the cavity of a detector. The *cavity* code uses the EGSnrc C++ class library which allows modeling of a wide range of different geometries and is not restricted to a Cartesian grid as is the case for the DOSXYZnrc code. This property is an advantage for modeling detectors, which often have complicated geometrical designs surrounding the sensitive volume. However, the simulations are computationally intensive especially if the detector is moved laterally or if perturbation factors are needed. The above issues were handled much better with the *egs_chamber* code which introduced a number of variance reduction techniques, such as cross-section enhancement, intermediate phase-space file and correlated sampling, to increase the efficiency of the simulations (Wulff, Zink, and Kawrakow, 2008).

2.3.4 Variance reduction techniques

The efficiency of a simulation is calculated by the following formula:

$$\epsilon = \frac{1}{\mathrm{T}\sigma^2}, \tag{2.31}$$

where T is the total computation time and σ^2 is the variance of the calculated quantity of interest (e.g. dose). A true variance reduction technique (VRT) improves the efficiency of the simulation without changing the calculated outcome. This means that repeating the calculations without the VRT should not alter the calculated results. In the following the main VRTs will be presented as they are applied most often in the EGSnrc-based codes.

Range rejection In range rejection the history of an electron is terminated if its kinetic energy becomes lower than a threshold value (ESAVE) that would not allow it to exit the current region and reach the cavity. However, during the rejected track the electron could have emitted bremsstrahlung photons that could potentially reach the cavity. If the ESAVE value is chosen to be 2 MeV or less, the bremsstrahlung yield is less than 2 % and practically the error in the dose calculations is expected to be very low (Rogers et al., 1995).

Particle splitting In particle splitting, particles are split to N identical particles, each one of them assigned a statistical weight of 1/N. This VRT is particularly useful in regions where there are not that many particles and the statistics need to be improved.

Russian Roulette In Russian roulette (RR) each particle is "killed" with a probability p and if it survives its weight is increased by 1/p. This is particularly useful in cases where there are many particles in regions that most likely will not contribute to the final dose in the region of interest. However, if the surviving particles do reach the region of interest they will have a significantly higher weight than all the rest that did not play RR and this may create a bias in the reported quantities. This particle is referred then as a "fat" particle.

Directional Bremsstrahlung Splitting Directional Bremsstrahlung Splitting (DBS) is one of the most important VRT in BEAMnrc accelerator simulations. First, a region of interest (ROI) is defined at the exit plane of the accelerator. Every time a bremsstrahlung photon is created it is split NBRSPL times. Each photon will then have a weight of 1/NBRSPL. For all photons targeted outside the ROI, RR is played with the surviving photon taking back its weight of NBRSPL. The above procedure results in many "non-fat" photons in the ROI (where statistics are important) and a few "fat" photons outside the ROI (where particle transport is inefficient).

Photon cross-section enhancement In photon cross-section enhancement (CSE) the photon cross-section values are increased by a factor b within a specified region. Thus, CSE will create b times more charged particles in that region than usual. However, since electron tracks are computationally expensive it is important to enhance the cross-sections only in regions where the resulting electrons are expected to deposit dose in the scoring region of interest. Otherwise, the calculation times will increase without any gains in the dose uncertainty and the efficiency will actually drop. This VRT is often used in the *egs_chamber* code with a CSE shell defined around the chamber geometry.

Intermediate phase-space storage (IPSS) In the case that someone wants to calculate the dose in the cavity of a detector as it is moved in different lateral or depth positions, it becomes inefficient to repeat the particle transport starting form the accelerator source each time. Instead, a geometrical region can be defined that surrounds all possible positions that a detector may be and upon simulation a temporary phase-space file is saved in that region. As the detector is moved to the next position the simulation starts directly from the IPSS region.

2.3.5 Uncertainties in MC simulations

Since MC simulations involve random sampling of probability distributions to estimate a particle trajectory and physical quantities of interest (e.g. dose or fluence), they are subject to statistical uncertainties. The initial approach for calculating the statistical uncertainty in the BEAM code system was the batch method (Rogers and Bielajew, 1990). According to this method the total number of histories is first grouped to N

batches. For each batch i the physical quantity of interest, X_i, (e.g. dose in a voxel) is calculated and the average value, $\overline{X}$, is determined as the mean value from all batches. The uncertainty estimate in the mean value $\overline{X}$ for N batches is determined as:

$$s^2 = \frac{1}{N(N-1)} \sum_{i=1}^{N} (X_i - \overline{X})^2 \tag{2.32}$$

Several problems are associated with the batch method. First, the uncertainty on the uncertainty is often large especially if the total number of batches N is relatively small (10 or less). For example, a batch sample size of $N = 10$ will result in an uncertainty of about 30 $\%$ assuming Poisson statistics. Secondly the method ignores any correlation between particles, an important issue if variance reduction techniques have been utilized. Finally, memory requirements are increased since an extra location is required to store the results from each batch.

An improvement on the previous approach is the history-by-history method (Walters, Kawrakow, and Rogers, 2002). A distinct difference of this method is that the uncertainty calculation is based on individual histories rather than batches. Equation 2.31 can be re-written as

$$s^2 = \frac{1}{N-1} \left(\frac{\sum_{i=1}^{N} X_i^2}{N} - \left(\frac{\sum_{i=1}^{N} X_i}{N} \right)^2 \right), \tag{2.33}$$

where N is the number of independent events or histories and X_i is the physical quantity of interest scored for an independent event i. Since the number of histories is a much larger sample than the number of batches, the uncertainty on the uncertainty is expected to be smaller. It should be noted that an independent event or history includes all particle tracks associated with one initial particle starting from the source. Thus, the history-by-history method preserves correlations between all particles associated with the same primary history. Finally, since $\sum_{i=1}^{N} X_i$ and $\sum_{i=1}^{N} X_i^2$ can be calculated on the fly memory requirements are improved.

Besides the statistical processes (type-A uncertainties), MC simulations will also suffer from uncertainties in the cross-section data, model approximations and round-off errors. In addition, type-B uncertainties are likely to be introduced depending on the accuracy of geometrical and material information used for modeling the accelerator and detector system. Technical drawings provided by the manufacturer are essential to be used for accurate dose calculations.

Chapter 3

A review of small field dosimetry

3.1 The physics of small fields

3.1.1 What constitutes small?

The definition of a small field size appears to be the first problematic area in small field dosimetry. In a clinical environment small fields are most often considered to be smaller than 3×3 cm^2 (Das, Ding, and Ahnesjö, 2008). However, this definition is rather arbitrary and originates from the empirical knowledge that measurements or calculations below these field sizes may often be problematic. Alternatively, small fields can be defined by means of a physics-related effect that appears at a specific collimator setting and is further enhanced as the collimation aperture becomes smaller. Such an effect could be the loss of CPE or the source occlusion. However, such an effect would vary depending on the beam energy, the collimator proximity to the source and the actual source size. Thus, the definition of "small" would vary depending on the beam quality and accelerator design. Charles et al., 2014 attempted to provide a practical definition of what could be considered small by quantifying the field size at which a detector or field size positioning error of 1 mm would result in an output factor variation of 1 % or more. They concluded that field sizes of 15 mm or less can be considered small for 6 MV photon beams and special experimental attention is required.

The above observations set theoretical boundaries in small fields by assuming that the dose in a small volume of water is reported. However, in clinical practice some of the most severe discrepancies in small field dose measurements arise from detector-specific effects. Thus, a complete definition of “small” should include the choice of the detector as well. For example, large volume detectors may start measuring dose in gradient regions and thus present a volume averaging of the signal (Laub and Wong, 2003). In such case “small” should be defined as the limiting field size that a specific detector can still measure in a uniform dose region.

3.1.2 Loss of charged particle equilibrium

As described in section 2.1.4, conditions of charged particle equilibrium exist if all charged particles exiting the cavity or sensitive volume of the detector are replaced by an equal amount of charged particles entering the cavity with similar energy and angular properties. Under CPE the collisional kerma is equal to the absorbed dose, a crucial condition for the application of cavity theory on ionization chamber dosimetry. As the field size becomes smaller or comparable to the electron range in the medium, charged particles generated in the field and scattered-out of the field are not going to be replaced by particles scattered-in, since there is no source to generate those outside the field (figure 3.1). However, one must appreciate that similar conditions will appear

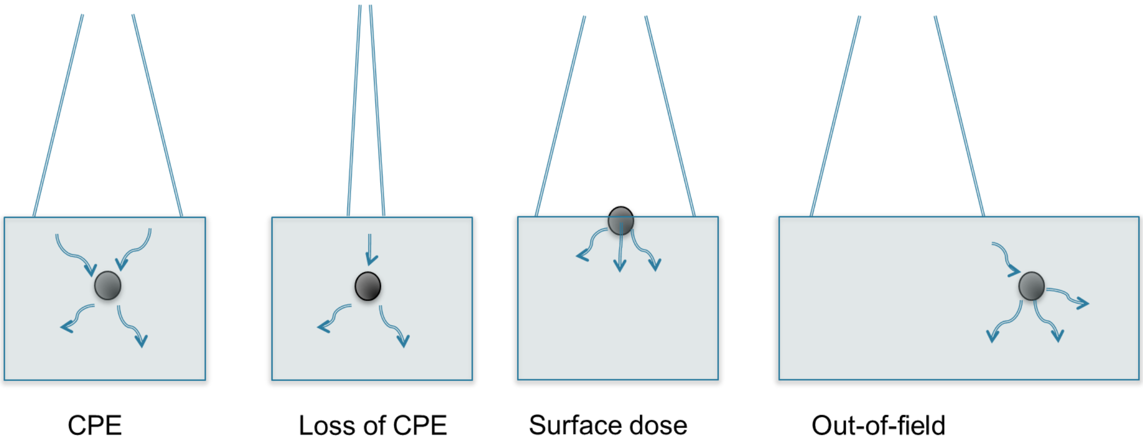

FIGURE 3.1: Loss of charged particle equilibrium (CPE) as the field becomes small, as the detector moves on the surface or out of the field

not only in small fields but also in large fields as the detector is moved closer to the phantom surface. Dose profiles will also suffer by loss of CPE as the detector exits the radiation field and thus electrons are scattered in the field only from one side (figure 3.1).

Loss of CPE is expected to be more pronounced for higher beam qualities (photon energies) since the generated charged particles will have longer ranges. It is possible to quantify the loss of CPE for each beam quality by calculating, using Monte Carlo methods, the absorbed dose and the collisional kerma in the cavity. The field radius for which the ratio of dose to K_{col} becomes lower than the equilibrium value can be identified as the loss of electron equilibrium radius, r_{LEE} (Li et al., 1995). Figure 3.2 presents this relationship for nominal beam qualities from Co-60 up to 24 MV.

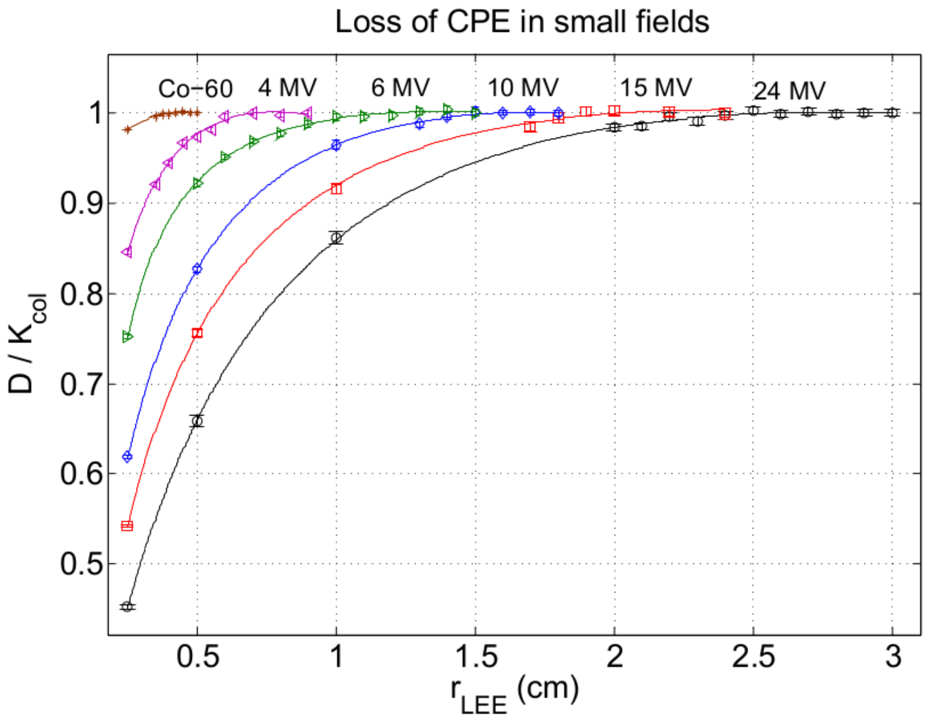

FIGURE 3.2: Ratio of dose to collisional kerma for beam qualities of Co-60 and 4 MV to 24 MV as a function of the field radius. The point where the curves cross the unity horizontal axis can be defined as the loss of electron equilibrium radius. The ratios are normalized to the equilibrium level.

3.1.3 Energy spectra and stopping power ratios in small fields

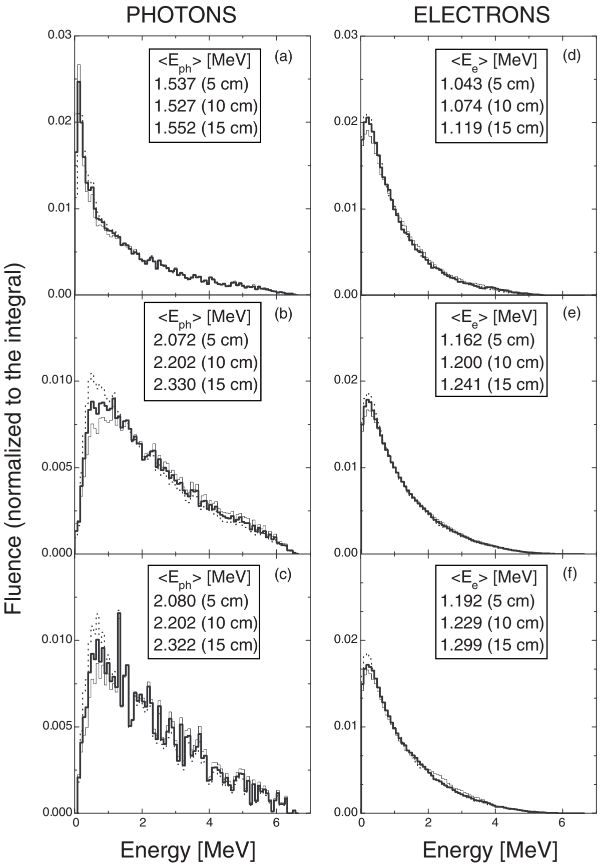

FIGURE 3.3: Photon and electron spectra in a 10 × 10 cm^2 square field (a,d) compared to the respective spectra using a radiosurgery applicator diameter of 1 cm (b,e) and 0.3 cm (c,f). Adapted by Sánchez-Doblado et al., 2003 by permission of IOP Publishing.

As the field size becomes increasingly small, mainly photons generated in the target directly arrive at the phantom surface, while scattered photons from the primary collimator and flattening filter become less important as they are most often emitted in larger angles and absorbed in the collimation blocks. In addition, photon fluence in large fields will include a low-energy component of bremsstrahlung radiation emitted from the target at large angles. Photon scattering in the phantom is also a dominant effect in larger fields. As a result of the above effects, the average photon energy is expected to be higher in small fields than large fields, an effect also referred as beam hardening. It follows that the average energy of the secondary electron fluence should also be expected to be higher. Sánchez-Doblado et al., 2003 have explored this in MLC-shaped narrow fields using Monte Carlo calculations (figure 3.3).

It is reasonable to expect that spectral changes may also affect the stopping power ratios of water to air, which for the purpose of reference dosimetry, are calculated for a 10×10 cm^2 field size. This could have a dosimetric effect on air-filled ionization chamber dosimetry where cavity theory is applied. However, Sánchez-Doblado et al., 2003 and Eklund and Ahnesjö, 2008 have shown that such variation does not exceed 0.6 % between 10×10 cm^2 and 0.3×0.3 cm^2 field sizes.

3.1.4 The source occlusion problem

As source we most often refer to the electron spatial intensity distribution incident on the target surface. Alternatively, the source could be defined as the bremsstrahlung fluence spatial intensity distribution as it is generated within the target or as it is seen below the target (Aspradakis, 2010). The latter definition may also be found in the literature as the *focal-spot*. The exact definition of the source depends strongly on the specifics of the beam model. MC accelerator models most often start the simulation from the electron source and model the particle transport in the target, while analytical beam models used in the TPS may start from the photon distribution below the target to increase computational efficiency. However, both definitions can be classified as the *direct* source of the linac. The electron (or photon) source is most often assumed to follow a 2-D elliptical Gaussian distribution and its size is characterized by the FWHM.

Incident photons on the various accelerator compartments, residing below the target, will produce scatter radiation. These are most often referred to as *indirect* or *extra-focal* sources. The flattening filter is mostly contributing to the extra-focal radiation which has been estimated to be about 8 % of the beam output (Jaffray et al., 1993) in large fields. The indirect/scattered photons are on average emitted in larger angles than the direct photons. Thus, in small fields the scattered photons will most probably be absorbed in the collimation blocks and their contribution to the beam output minimized. As shown in figure 3.4 it is the direct source emitted from the target that almost exclusively contributes to the beam output of small field sizes.

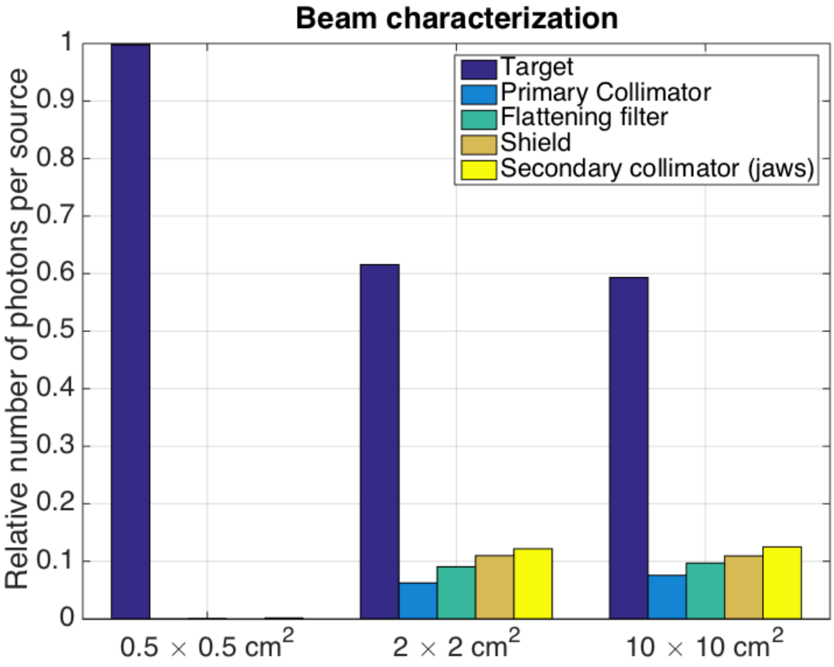

FIGURE 3.4: Direct (target) and indirect/scattered radiation sources emitted by a medical linear accelerator for field sizes of 0.5 × 0.5, 2 × 2, 10 × 10 cm^2. For the smallest field size, photons almost exclusively originate from the target.

As the collimation aperture is reduced, there is a point at which the collimation opening is comparable to the photon source size as projected from the target to the collimation level. Further reduction of the field size will result in partial blocking of the photon source, an effect commonly referred as partial source occlusion. The full source distribution is no longer visible from the measurement point and thus the beam output is expected to drop. Furthermore, the overlapping penumbras created by the opposed collimation jaws will affect the dose profiles.

3.2 The dosimetry of small fields

3.2.1 Output factor and dose profile measurements

Output factors (OF) and dose profiles (DP) are some of the most important dose measurements that need to be performed during linac commissioning. These data need to be provided as an input to the TPS to appropriately tune beam model parameters, such as the source size and energy. Therefore, the accuracy of these measurements is an essential requirement. The OF is defined as the ratio of the dose delivered at a point in a field size $\mathrm{f_{clin}}$, $\mathrm{D^{fclin}}$, to the dose delivered at the same point in a reference field $\mathrm{f_{ref}}$, $\mathrm{D^{fref}}$:

$$\mathrm{OF} = \frac{\mathrm{D^{fclin}}}{\mathrm{D^{fref}}} \tag{3.1}$$

A dose profile is defined as the ratio of the dose delivered at a point in a field size $\mathrm{f_{clin}}$ at an off-axis position, $\mathrm{D^{fclin}}(\mathrm{x})$, to the dose delivered at a point at the central axis in the same field size $\mathrm{f_{clin}}$, $\mathrm{D^{fclin}}(0)$:

$$\mathrm{DP} = \frac{\mathrm{D^{fclin}}(\mathrm{x})}{\mathrm{D^{fclin}}(0)} \tag{3.2}$$

Dose profiles define the radiation field size as the distance between the 50 % dose levels. The profiles can be measured in the in-plane (y) or cross-plane (x) orientations. The penumbra width (PW) is defined as the lateral distance at which the dose will drop from the 80 % to the 20 % dose level or alternatively from the 90 % to 10 % dose level. The PW depends on the source size and level of occlusion, the lateral electron range and photon scattering. Thus, PWs are expected to vary as a function of depth and field size.

The measurements are performed with the use of a water tank and an appropriate detector. For accurate detector positioning, special holders are manufactured and utilized along with a motorized scanning system. As a first step the detector is positioned at the center of a large field using the linac positioning alignment system. As a second step the detector position is fine tuned in a small field while the radiation beam is on, until the maximum signal is measured. The depth of the measurements should be chosen so that that electrons generated in the accelerator head during photon transport, referred also as electron contamination, can not reach the measurement point and perturb the measurements. A depth of 5 cm or 10 cm can be considered sufficient for all energies. The source to surface distance (SSD) should ideally be set at 100 cm as this is most often the reference distance used during linac calibration. Most TPS require that OFs and DPs be measured for every field size that may be needed during IMRT and SRS treatments.

As explained in the previous sections, small fields and out-of-field positions will suffer from loss of CPE and partial source occlusion. The latter will result in a drop of the OF and an increase in the PW as a function of source size. Figure 3.5 exhibits these effects on OFs and DPs as the FWHM of the source varies from 0 to 2 mm.

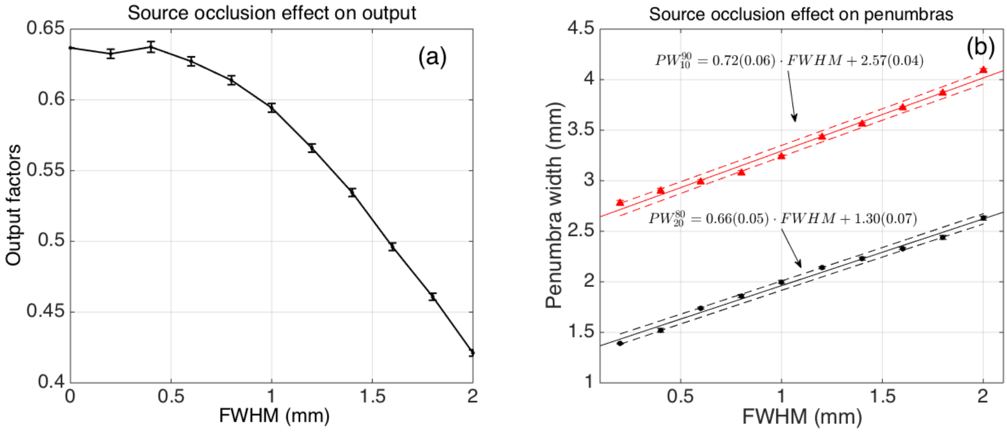

FIGURE 3.5: The effect of source occlusion on output factors (a) and profile penumbras (b) of a 0.5 × 0.5 cm^2 relative to a reference field size of 10 × 10 cm^2. As the source's FWHM is increased the output factors drop and the penumbra widths (80-20 % and 90-10 %) are increased. Monte Carlo calculations of dose to water using a Varian Novalis linac model and the BEAMnrc/egs_chamber codes

Another particular problem of small fields is related to the field size definition. For large fields the dosimetric field size (FWHM) follows closely the field size as projected by the collimation blocks. However, as the field becomes comparable or smaller to the lateral electron range, the profile penumbras will start overlapping, the output will drop and the dosimetric field size will be broader than the projected aperture (figure 3.6). It is therefore crucial for experimentalists to report both the dosimetric field size and the nominal geometric field size. Cranmer-Sargison et al., 2013 has recently proposed an effective field size metric ($\mathrm{FS_{eff}} = \sqrt{\mathrm{FWHM_x} \cdot \mathrm{FWHM_y}}$) to increase the reproducibility of OF reporting in small fields among different accelerators.

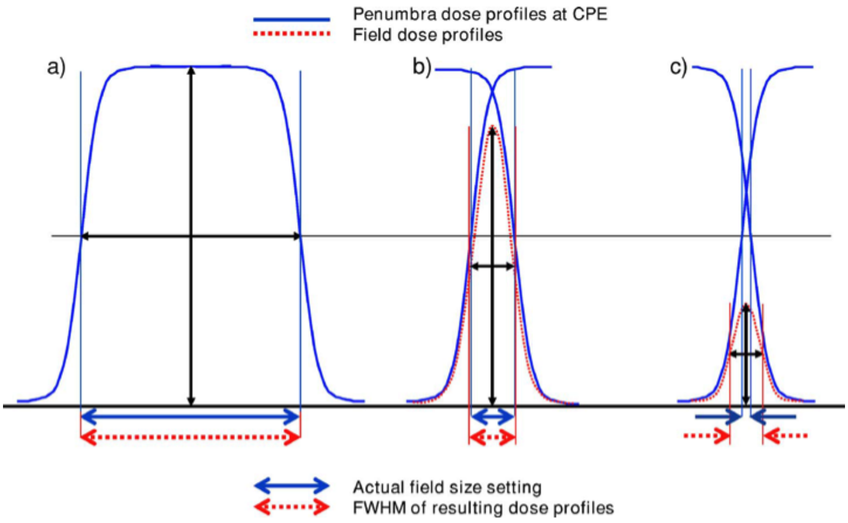

FIGURE 3.6: Apparent field widening observed in small field sizes. Adapted by Das, Ding, and Ahnesjö, 2008 with permission by AIP publishing.

3.2.2 Detector-specific perturbations

The discussion in the previous section assumed that the output factors and dose profiles are measured with an “ideal” detector which for the purposes of clinical radiation dosimetry would be a small water cavity. However, such a detector does not exist. Real dosimeters may often include material components with significantly different atomic composition and density properties than water. These components may perturb the electron fluence towards or inside the sensitive volume and therefore the measured signal may be different than what a water cavity would have reported.

The perturbations in small fields should mostly be attributed to deviations of the material density rather than atomic number, as shown by Scott et al., 2012. Specifically, detectors with material densities higher than water will cause an over-response on the OFs. Silicon diodes ($\rho = 2.33\frac{gr}{cm^3}$) and diamond ($\rho = 3.5\frac{gr}{cm^3}$) detectors fall in this category. However, even liquid-filled ionization chambers may include high density components, such as the graphite electrode ($\rho = 1.7\frac{gr}{cm^3}$) (Wagner et al., 2013). The above perturbations become significant under loss of CPE conditions. Beddar, Mason, and O'Brien, 1994 observed perturbations on diode profile measurements, which they attributed to the reduced range of electrons in high density materials.

Silicon diodes are expected to present an energy dependence due to the higher atomic number of silicon to water ($Z_{\mathrm{Si}} = 14$). This will result in an increasing over-response as the field size becomes larger and the energy spectrum softer due to the photoelectric effect. This fact is of concern even in small fields as the choice of the reference field (f_{ref}) will alter the relative over-response observed by diodes in the clinical small fields (f_{clin}). The geometry and thickness of the material surrounding the cavity will alter significantly the above effects and hence detailed detector modeling and MC simulations are essential for accurate calculation of the detector response.

A second important perturbation observed in real dosimeters is attributed to the physical size (or resolution) of the sensitive volume. If the sensitive volume is measuring a signal in a gradient dose region then the average detector response will be lower than the average in a uniform dose region. The volume averaging effect can be better understood by looking at figure 3.7. Even a volume of radius of 0.5 mm is expected to show some volume averaging effects for the smallest field size of 0.5 × 0.5 cm^2, while larger radii will cause even more significant effects. For the 1 × 1 cm^2 a radius of 1 mm is sufficient for measuring in a uniform dose region. Such figures are therefore important, even if we are only interested in OFs, as they can serve as a guide on the resolution limits of each detector system. Furthermore, a convolution kernel can be possibly extracted to correct volume averaging effects as shown by Laub and Wong, 2003. Volume averaging effects is one major limitation for air-filled ionization chambers, since due to their low sensitivity they need to be manufactured in relative large volumes. However, it should not be assumed that volume averaging is the sole perturbation observed in air-filled chambers. Other effects, such as the central electrode, may also perturb the fluence as shown by Pappas et al., 2006 and Crop et al., 2009 for dose profiles. On the other hand diodes, film, scintillators and liquid ionization chambers can be manufactured in smaller volumes and from that perspective their advantageous for small field dosimetry.

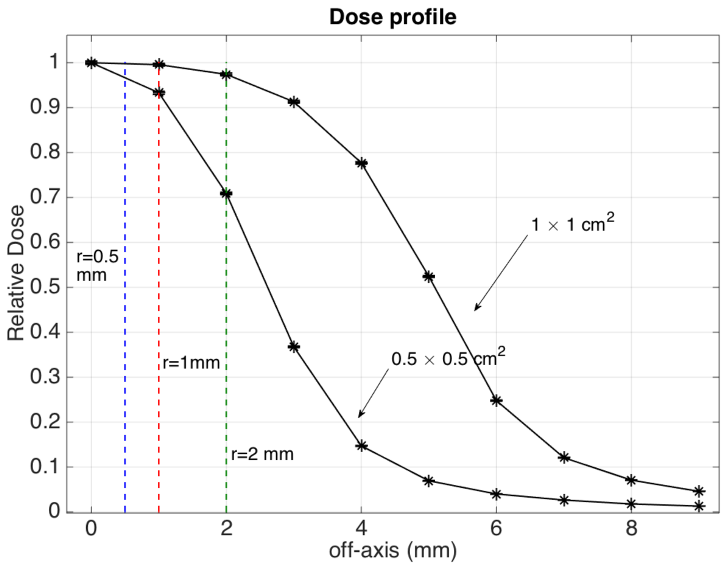

FIGURE 3.7: Dose profiles of the two smallest fields sizes of 0.5 × 0.5 cm^2 and 1 × 1 cm^2 as they compare to the radius of the sensitive volume of a detector.

The most clear way for extracting the detector-specific perturbation factors is based on Monte Carlo techniques (Bouchard et al., 2009a). To that purpose, MC codes, such as egs_chamber, can be utilized to model the full detector geometry. Each detector layer (shell, electrode etc) is then removed sequentially and the calculations repeated.

The calculated dose ratio between two subsequent steps provides the perturbation factor for the specific layer removed. Eventually the active volume is replaced with water which represents the fluence perturbation and stopping power ratio variation. As a final step the water active volume is replaced with a point (small volume) in water that represents the volume averaging perturbation. It is important to note that since a point in water is ill-defined, the "small" volume chosen needs to be small enough so that no volume averaging effects are observed for the field size of interest.

3.2.3 The Alfonso formalism

In 2008, Alfonso et al., 2008 suggested a new formalism for the dosimetry of small and non-standard beams. According to the formalism, detector-specific and field-specific correction factors can be extracted. The correction factors can then be directly applied on measurements to take into account the detector-specific material perturbations and volume averaging effects.

In relative dosimetry the Alfonso formalism defines the term *field factor*, $\Omega^{\mathrm{f_{clin},f_{msr}}}_{\mathrm{Q_{clin},Q_{msr}}}$, as the ratio of absorbed dose to water $\mathrm{D^{f_{clin}}_{w,Q_{clin}}}$ at a reference point in water for a clinical field $\mathrm{f_{clin}}$ and a beam quality $\mathrm{Q_{clin}}$ to the absorbed dose to water $\mathrm{D^{f_{msr}}_{w,Q_{msr}}}$ at a reference point in water for a machine-specific reference field $\mathrm{f_{msr}}$ and a beam quality $\mathrm{Q_{msr}}$:

$$\Omega^{\mathrm{f_{clin},f_{msr}}}_{\mathrm{Q_{clin},Q_{msr}}} = \frac{\mathrm{D^{f_{clin}}_{w,Q_{clin}}}}{\mathrm{D^{f_{msr}}_{w,Q_{msr}}}} \tag{3.3}$$

The machine-specific reference field could be a 10 × 10 cm^2 or the largest possible, if that can not be realized in a specific treatment unit. For example the CyberKnife system can produce a circular field up to a diameter of 6 cm, thus this should be defined as the msr field. The definition of a field factor follows closely the definition of output factor, commonly used in the clinic, with the subtlety that it explicitly refers to dose in a point in water.

In a similar manner, the *detector specific output factor*$\mathrm{OF}_{\mathrm{det}}$, also referred as output ratio or reading ratio, is defined as an average measured signal $\mathrm{M}_{\mathrm{Q_{clin}}}^{\mathrm{f_{clin}}}$ at a reference point for a clinical field $\mathrm{f_{clin}}$ and a beam quality $\mathrm{Q_{clin}}$ to the average measured signal $\mathrm{M}_{\mathrm{Q_{msr}}}^{\mathrm{f_{msr}}}$ at a reference point for a machine-specific reference field $\mathrm{f_{msr}}$ and a beam quality $\mathrm{Q_{msr}}$.

$$\mathrm{OF}_{\mathrm{det}} = \frac{\mathrm{M}_{\mathrm{Q_{clin}}}^{\mathrm{f_{clin}}}}{\mathrm{M}_{\mathrm{Q_{msr}}}^{\mathrm{f_{msr}}}} \tag{3.4}$$

The previous definitions assist greatly in removing the ambiguity that often exist between detector-specific and water cavity output factors. A detector-specific correction factor, $\mathrm{k}_{\mathrm{Q_{clin},Q_{msr}}}^{\mathrm{f_{clin},f_{msr}}}$, can then be defined for a specific field ($\mathrm{f_{clin}}$) and beam quality ($\mathrm{Q_{clin}}$) as:

$$\mathrm{k}_{\mathrm{Q_{clin},Q_{msr}}}^{\mathrm{f_{clin},f_{msr}}} = \frac{\mathrm{D}_{\mathrm{w,Q_{clin}}}^{\mathrm{f_{clin}}}/\mathrm{D}_{\mathrm{w,Q_{msr}}}^{\mathrm{f_{msr}}}}{\mathrm{M}_{\mathrm{Q_{clin}}}^{\mathrm{f_{clin}}}/\mathrm{M}_{\mathrm{Q_{msr}}}^{\mathrm{f_{msr}}}} = \frac{\Omega_{\mathrm{Q_{clin},Q_{msr}}}^{\mathrm{f_{clin},f_{msr}}}}{\mathrm{OF}_{\mathrm{det}}} \tag{3.5}$$

Since, in general, the measured signal is expected to be proportional to the absorbed dose ($\mathrm{M} \propto \mathrm{D}$), $\mathrm{k}_{\mathrm{Q_{clin},Q_{msr}}}^{\mathrm{f_{clin},f_{msr}}}$ can be re-written as:

$$\mathrm{k}_{\mathrm{Q_{clin},Q_{msr}}}^{\mathrm{f_{clin},f_{msr}}} = \frac{\mathrm{D}_{\mathrm{w,Q_{clin}}}^{\mathrm{f_{clin}}}/\mathrm{D}_{\mathrm{w,Q_{msr}}}^{\mathrm{f_{msr}}}}{\mathrm{D}_{\mathrm{det,Q_{clin}}}^{\mathrm{f_{clin}}}/\mathrm{D}_{\mathrm{det,Q_{msr}}}^{\mathrm{f_{msr}}}} \tag{3.6}$$

This points towards a MC methodology for deriving the $\mathrm{k}_{\mathrm{Q_{clin},Q_{msr}}}^{\mathrm{f_{clin},f_{msr}}}$ correction factors, which can be summarized in the following steps:

1. Calculate the dose in a small volume of water ($\mathrm{D_w}$) for the ($\mathrm{f_{clin}, Q_{clin}}$) and ($\mathrm{f_{msr}, Q_{msr}}$) field sizes and beam qualities.

2. Model the detector design using the technical sketches provided by the manufacturer.

3. Calculate the dose in the sensitive volume of the detector model ($\mathrm{D_{det}}$) for the ($\mathrm{f_{clin}, Q_{clin}}$) and ($\mathrm{f_{msr}, Q_{msr}}$) field sizes and beam qualities.

4. Calculate the $\mathrm{k^{f_{clin},f_{msr}}_{Q_{clin},Q_{msr}}}$ correction factor using equation 3.6.

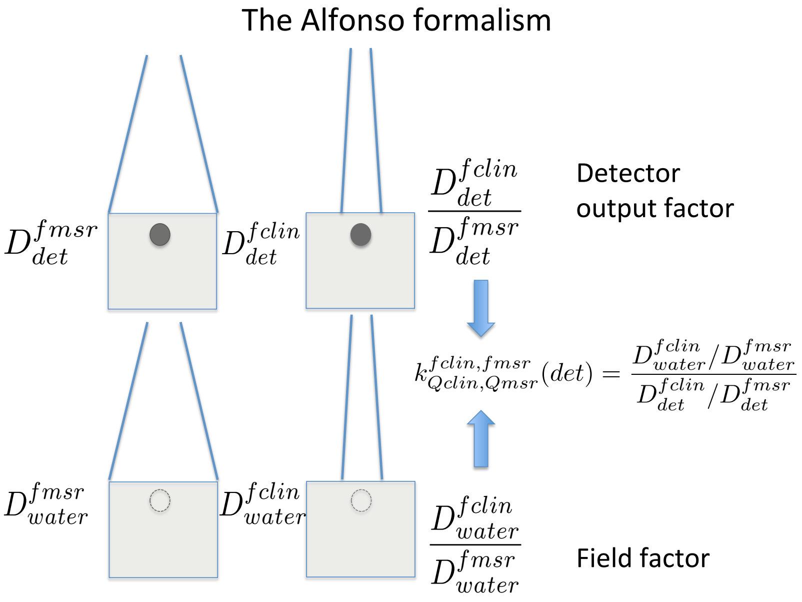

FIGURE 3.8: Based on the Alfonso formalism a detector- and field-specific correction factor, $\mathrm{k^{f_{clin},f_{msr}}_{Q_{clin},Q_{msr}}}$, can be calculated as the ratio of field factor $\mathrm{\Omega^{f_{clin},f_{msr}}_{Q_{clin},Q_{msr}}}$ to detector output factor. The field factor can be estimated by Monte Carlo or experimental methods.

It is important to emphasize that the assumption of $\mathrm{M} \propto \mathrm{D}$ may not always be true and corrections to the measured signal may need to be taken into account first. For example liqiud ionization chambers suffer from ion recombination effects and plastic scintillators from Cherenkov radiation produced in the fiber. These effects are difficult to simulate and are not usually included in the MC calculation. Nevertheless the MC methodology provides a clear path for extracting $k^{f_{clin},f_{msr}}_{Q_{clin},Q_{msr}}$ factors as related to the material perturbations and volume averaging effects.

The Alfonso formalism suggests an alternative pathway for extracting the correction factor: if a specific detector is shown to require minimal corrections ($k^{f_{clin},f_{msr}}_{Q_{clin},Q_{msr}} \simeq 1$), then it could potentially be used as a reference detector for extracting correction factors for other dosimeters. In such a case equation 3.5 can be used with the field factor $\Omega^{f_{clin},f_{msr}}_{Q_{clin},Q_{msr}}$ approximated by the reference detector reading ratio. Such a detector should be water-equivalent and provide high resolution measurements so that material and volume averaging perturbations could be neglected. Potential candidates for this role include radiochromic film, alanine pellets, polymer gels, thermoluminescent dosimeters (TLD) and plastic scintillators (Pantelis et al., 2012).

There are disadvantages and advantages in both the MC and experimental approaches for deriving the $k^{f_{clin},f_{msr}}_{Q_{clin},Q_{msr}}$ factors. The MC approach offers much higher precision and accuracy level, if the material composition and geometry is accurately known. For that purpose, detector technical sketches are needed from the manufacturers. Uncertainties in the detector model will propagate as a systematic error in the $k^{f_{clin},f_{msr}}_{Q_{clin},Q_{msr}}$ calculation. In order for the calculations to be representative of a realistic radiation beam, the linear accelerator should be also modeled, using perhaps a MC user code such as BEAMnrc, followed by a careful tuning of the linac beam parameters. The dose calculations themselves are computationally challenging and the use of large computer clusters is still essential, even if variance reduction techniques are applied.

On the other hand, the experimental approach appears to be more practically implemented in the clinic. Furthermore, it inherently includes any detector-related effects that may not be easily simulated. However, most of the dosimeters suggested as candidate reference detectors are not accessible in the clinic. For radio-chromic film and polymer gels, calibration and scanning protocols are needed. Others, such as alanine and TLDs, need to be sent to an external standard lab for read-out. Plastic scintillation dosimeters are perhaps the most promising real-time dosimeter that can be offered in the clinic, if the Cherenkov issue is properly addressed.

3.2.4 Detector-specific correction factors

Monte Carlo approach

Francescon, Cora, and Cavedon, 2008 and Araki, 2006 were some of the first that extracted correction factors for the Cyberknife system using Monte Carlo methods. They observed an over-response for silicon diodes and under-response of air-filled ionization chambers and diamond detectors relative to water. Furthermore, they emphasized the need for accurate modeling of the linear accelerator and fine-tuning of the main beam parameters associated with them, especially the electron source energy and intensity distribution. Francescon, Cora, and Cavedon, 2008 demonstrated that there is a strong dependence of the output factor to the source FWHM parameter, especially for the smallest field size of 0.5×0.5 cm^2, while smaller dependencies were observed to the energy of the source.

In a later study Francescon, Cora, and Satariano, 2011 calculated $k_{Q_{clin},Q_{msr}}^{f_{clin},f_{msr}}$ factors for two linear accelerators (Siemens Primus and Elekta Synergy) for a series of small field detectors including unshielded silicon diodes (PTW Diode 60012), shielded diodes (Sun Nuclear Edge), air-filled ionization chambers (Exradin A16, PTW Pinpoint 31014) and liquid ionization chambers (PTW microLion). They also investigated the sensitivity of the correction factors on the source size, energy and distance of exit window on the target, which they included in their total uncertainty analysis. The smallest corrections were observed for the microLion, which exhibited a slight under-response (-2.4%) relative to water for the 0.5 × 0.5 cm^2 field size. Silicon diodes presented significant corrections ranging from +3.2 % (unshielded) to +6.8 % (shielded) for the same field. However, an interesting finding in this study was that the $k_{Q_{clin},Q_{msr}}^{f_{clin},f_{msr}}$ corrections seem to be relative insensitive to source size variations, especially for the case of diodes. The reported corrections were even similar among the two different accelerator types. This important conclusion implies that a "universal" application of the Alfonso formalism may be possible and the same correction factors could be applied to different systems without the need of accurate knowledge of the specific beam characteristics.

In a related study, Cranmer-Sargison et al., 2011 performed measurements and MC calculations of output factors for a comprehensive set of silicon diodes including the PTW's 60008, 60012, 60016, 60017 and the IBA SFD. the measurements were performed for a Varian iX linac using the secondary collimators (jaws). All diodes presented significant over-responses up to 11.5 % relative to a 0.5 × 0.5 cm^2 field size. The correction factors appeared consistent as a function of depth within a level of 1.4 %. In a follow-up study (Cranmer-Sargison et al., 2012) they simplified their detector models by gradually removing each layer in order to evaluate the most important detector components. They concluded that the dosimetric accuracy for the simplified models was preserved as long as all components, especially those with high density, that reside close to the cavity are properly modeled.

The accurate knowledge of the density of materials surrounding the cavity might, however, not be as straightforward as one would think. In an updated study on the CyberKnife system, Francescon et al., 2012 reported that it was impossible to obtain consistent data regarding the epoxy material surrounding some of the silicon diode designs. They estimated that the epoxy density may be within the range of 1.2-1.8 gr / cm^3, which would have an effect of 3-4 % on the output factor of the 5 mm field size. Eventually they followed an optimization procedure for identifying the epoxy density in each detector model based on corrected output factors measured using air-filled ionization chambers. They found that the optimized densities in all cases converged in the region of 1.4 -1.5 gr / cm^3. This matter may be of considerable concern for the MC detector modeling and it might imply that some detector model tuning might be necessary, even if technical sketches are provided by the manufacturers.

In a recent study Wagner et al., 2013 studied the output factor correction and perturbation factors for the PTW liquid ionization chamber (PTW microLion). The overall correction amounted to a small under-response of about 2.4 - 2.7 % confirming the previous calculations by Francescon et al., 2012. However, the perturbation factors revealed a significant volume averaging correction (-5.2 %), relative to the reference field, which was partly compensated by the graphite electrode perturbation (+3.2 %).

Thus the overall small correction observed for this type of detector should not be attributed to its “water-like” behaviour but mainly to the cancellation of two opposing effects. Similarly, Charles et al., 2013 and Underwood et al., 2013 improved the performance of diode and diamond detectors by inserting a small cavity of air on top of the high density areas. The air cavity compensated the expected over-response of the diode and diamond substrates in small fields and minimized the overall correction factor.

Experimental approach

In parallel to the previous studies, Pantelis et al., 2010 followed the experimental approach of extracting $\mathrm{k}_{\mathrm{Q_{clin},Q_{msr}}}^{\mathrm{f_{clin},f_{msr}}}$ factors. As reference dosimeter they used radiochromic film, polymer gels, alanine pellets and TLDs. They also performed measurements using the same diodes and air-filled ion chambers and applied the MC corrections calculated previously by Francescon, Cora, and Cavedon, 2008 directly on the detector reading ratios, as suggested by the Alfonso formalism. The field factors were estimated by calculating the weighted average of all the corrected measurements. Alanine dosimeters needed a significant volume averaging correction up to 24.9 % for the smallest field size of 0.5 × 0.5 cm^2, as the pellet diameter is about the same size to the FWHM of that field. For the same field size radiochromic film and polymer gels presented the highest uncertainties in the range of 2.6 - 3 %. The output factor of the MC-corrected readings between all chambers and diodes presented an agreement within 1.6 % of the alanine result, after volume averaging correction and within the experimental uncertainties of the TLD and EBT film measurements. Thus, this work validated the MC method for extracting the $k_{Q_{clin},Q_{msr}}^{f_{clin},f_{msr}}$ factors and provided evidence for consistency between MC and experimental approaches. In a follow up study, (Pantelis et al., 2012) the $k_{Q_{clin},Q_{msr}}^{f_{clin},f_{msr}}$ correction factors were derived also as a function of source-to-detector distance (SDD). They observed a significant reduction ($< 14.7\ \%$) in the $k_{Q_{clin},Q_{msr}}^{f_{clin},f_{msr}}$ factor of an air-filled ionization chamber (PTW Pinpoint 31014) and a smaller, but noticeable reduction on some diodes ($< 3\ \%$) as the SDD increased. Similar effects were also observed with Monte Carlo calculations (Francescon, Kilby, and Satariano, 2014).

Bassinet et al., 2013 determined $k_{Q_{clin},Q_{msr}}^{f_{clin},f_{msr}}$ correction factors for shielded diodes (Sun Nuclear EDGE and PTW 60016), unshielded diodes (PTW 60017 and IBA SFD), air filled ionization chambers (PTW PinPoint 31014), liquid ionization chambers (PTW microLion) and a diamond detector (PTW 60003). EBT radiochromic film and TLDs were used as reference detectors. The measurements were performed on several accelerator types and collimation systems including a CyberKnife system, a Varian Novalis with circular cones and MLCs and a Clinac 2100 equiped with a microMLC. Similarly to previous findings they observed a significant over-response for most of the silicon diodes, especially for the shielded types, and an under-response for the air-filled ionization chambers and diamond detectors. The diode correction factors appeared not to depend significantly on the accelerator type and collimation level with the exceptions of the Pinpoint 31014 and the diamond detector. The smallest correction factors for the $0.6 \times 0.6\ \mathrm{cm}^2$ field size were observed for the IBA SFD diode and the PTW microLion.

Recent studies have also focused their attention in the development and evaluation of plastic scintillation dosimeters (PSDs) in small field dosimetry. Morin et al., 2013 was able to reproduce the correction factors previously calculated by Francescon et al., 2012 and Araki, 2006 for the CyberKnife system within 1.8 % using a 0.5 mm diameter PSD. For a similar 1 mm diameter PSD a small under-response was observed (< 1.1 %) which was attributed to volume averaging. In that work the Cherenkov radiation produced in the fiber was corrected by the spectral discrimination technique originally proposed by Fontbonne et al., 2002 and later on formulated by Guillot et al., 2011. An alternative approach was presented by Ralston et al., 2012 using a scintillator coupled with an air-core fiber, which is not expected to produce any Cherenkov radiation and thus no further corrections are needed. The scintillator measurements agreed well with radiochromic film and diode correction factors were extracted.

Off-axis corrections

In later years, several researchers have extracted $\mathrm{k}_{\mathrm{Q_{clin},Q_{msr}}}^{\mathrm{f_{clin},f_{msr}}}$ output factor correction factors following either the MC approach (Czarnecki and Zink, 2013; Kamio and Bouchard, 2014; Benmakhlouf, Sempau, and Andreo, 2014) or experimental approach (Azangwe et al., 2014). However, not many researchers studied dose profile correction factors, which might be necessary as well. In fact, these corrections may be needed even in large fields as explained in section 3.1.2. Air-filled ionization chambers are expected to present volume averaging effects due to their relative low resolution which would result in a broadening of the penumbra width. This effect could potentially be corrected by de-convolving the measurements with an analytical volume averaging kernel (Garcia-Vicente, Delgado, and Rodriguez, 2000). However, volume averaging may not account fully for all the effects observed. For example material perturbations may alter the kernel or correction factor required. Thus, the deconvolution kernel should model the full detector response, as shown by Pappas et al., 2006. Monte Carlo methods would appear to be the most appropriate method for deriving such corrections with the detector fully modeled.

Crop et al., 2009 studied the response of two air-filled ionization chambers (PTW PinPoint 31006 and 31016) as the detector moves laterally off-axis by MC calculations. The two detectors were similar to each other, but with different central electrode materials (Steel and Al) and lengths (4.5 mm and 1.6 mm). Even though volume averaging was found to be one of the most important effects, the central electrode, the wall and the air to water conversion presented important perturbations as well. The volume averaging effect exhibited a significant variation as a function of distance, source size and cavity length. The central electrodes presented smaller dependencies on source size, but a systematic 1% increase of the correction was observed if the electrode material was steel rather than Al. They concluded that extensive calculations would be needed to study the perturbations and corrections presented in modern small field detectors, such as liquid filled ionization chambers.

3.3 Reconstructing the source distribution

The previous section focused on the dosimetry of small fields and the derivation of correction factors that could be directly applied on measurements. The Alfonso formalism provided a specific guideline for the derivation of such corrections using MC or experimental methods. However, both methods are not easily implemented. The MC approach demands large computational resources which are not commonly available in a clinical environment. On the other hand the experimental approach relies heavily on the accuracy of special dosimeters that are considered to be "correction-free". However, the uncertainty in the measurements and calibration procedures for such detectors may be prohibitive for small radiation fields. Possible dependencies of the detector-specific correction factors on the field size, collimation system, linear accelerator type, SSD and depth of measurements complicates matters even more. A long list of correction factors will eventually be needed to account for all cases which would need to be frequently updated with new detectors, accelerator types, collimation systems etc. This approach might not be practically possible.

It is important to realize that output factor and dose profiles measurements are needed for the commissioning of the beam models used in a treatment planning system (TPS). After commissioning, the TPS is used for dose calculations on the patient-specific geometry and subsequently optimization of the treatment plan. Any errors occurring during commissioning will result in erroneous dose calculations to the patients and unavoidably affect the treatment outcome. Thus, the detector-specific correction factors serve towards this goal. However, commissioning of the TPS for small fields is mostly related to the determination of the source size and shape of the linear accelerators. In principle if we know the exact source distribution of the linear accelerator and the collimator field settings as well as the particle transport is accurately calculated in a linac, we should be able to reproduce the correct output factor and dose profiles, without the need of any correction factors. This idea can be seen as an alternative path for the accurate commissioning of linear accelerators. In addition the development of a source reconstruction technique could greatly assist in linac quality assurance procedures.

Several researchers have attempted to reconstruct the source size and/or distribution. In the following a brief review of the previous work is presented with the reconstruction techniques separated to *direct* methods, referring to techniques that allow the reconstruction of the full source distribution without the use of another dose metric and *indirect* methods, referring to techniques that reconstruct the FWHM of the source (source size) by evaluating the relative effect of source variations on another dose metric.

3.3.1 Direct reconstruction techniques

The first method suggested for direct measurement of the linac source distribution was the foil activation technique (P.D. La Riviere, 1980). The foil activation method utilizes a metal foil, such as tantalum (Ta), which upon irradiation is activated for photon energies above a threshold (7.64 MeV for Ta). If the foil is placed directly in contact with the target while the radiation beam is generated then the foil will be activated in the position where photons were emitted. The source intensity distribution can be measured by a film placed directly on the activated foil. Even though this technique offered a true direct reconstruction of the source distribution it was restricted by the fact that the target is not easily accessible without dismantling the linac. Furthermore, the energy threshold does not allow measurements in low energy beams, such as 6 MV or 4 MV.

Another suggested approach was the “beam-spot” camera (Lutz, Maleki, and Bjärngard, 1988). The camera is composed by alternating thin sheets of lead (Pb) and cardboard of 0.25 mm thickness each. The idea is that only photons traveling in straight lines from the source will pass through the cardboard openings while others will be blocked in the Pb foils (figure 3.9). For the measurements the accelerator gantry is rotated 180 degrees in the beam up position and the collimation jaws closed sufficiently so that the camera can be placed on them. A film is placed behind the camera to measure the photon distribution. Even though this device could be a practical solution in the clinic, it appeared to lack the needed accuracy, since the FWHM broadening of the dose distribution caused by the camera was about the same order of magnitude as a typical linac source (1-2 mm). This could partly be attributed to photons travelling in oblique angles and passing through the Pb sheets. Furthermore, the camera measured strip integrals of the distribution instead of points. Nevertheless, such a tool could still be useful for qualitatively evaluating source changes as part of a linac quality assurance procedure. Huang et al., 2005 used this technique to improve the dosimetry of large electron fields.

Munro, Rawlinson, and Fenster, 1988 suggested a slit collimator technique which up to date is probably the most accurate and robust direct source reconstruction technique. The method relies on the measurements of strip integrals of the X-ray source using large slit collimators (figure 3.10). The slit is formed by two pairs of blocks of lead/antimony alloy of length of 20 cm or 50 cm (figure 3.10). The slit width was 0.13 mm. The blocks were mounted on a dove-tailed slide controlled by stepper motors. The dove-tailed slide could rotate allowing the slit to measure projections at different angles. The strip source integral was measured by a diode placed underneath the slit. A CT reconstruction algorithm was used to reconstruct the source intensity distribution from the source line integrals. The total measurement time for measuring one

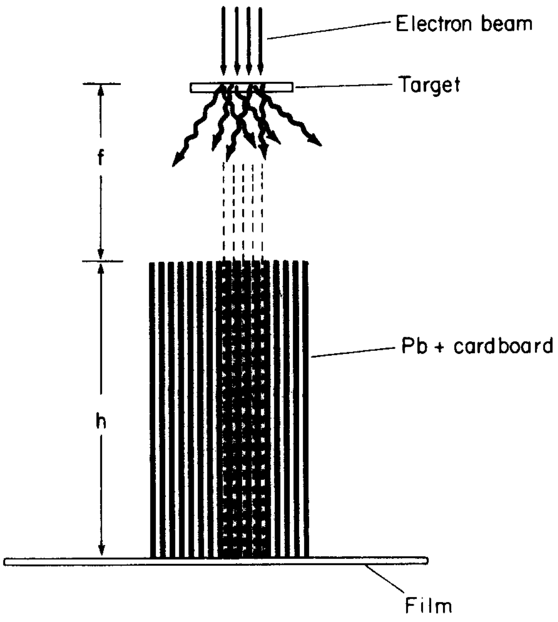

FIGURE 3.9: A schematic diagram of the "beam-spot" camera used by Lutz, Maleki, and Bjärngard, 1988 for measuring the source intensity distribution. Adapted by Lutz, Maleki, and Bjärngard, 1988 with AIP permission.

source varied between 2-12 hours.

The source distribution of three different Atomic Energy of Canada, Limited (AECL) Therac accelerators was measured for nominal beam energies of 6, 18 and 25 MV. The results presented source sizes ranging from 2 to 3 mm in FWHM and they seemed to decrease in size as the nominal energy increased. Furthermore the source shape was found to be elliptical with varying eccentricities. The authors demonstrated that the source distribution changes as the electron beam currents are altered. Measurements performed on a ^{60}Co machine indicated that the source output was not uniform as expected.

In a later study Jaffray et al., 1993 used the slit collimator technique to measure the source distributions of 9 different accelerators including Therac, Varian and Siemens

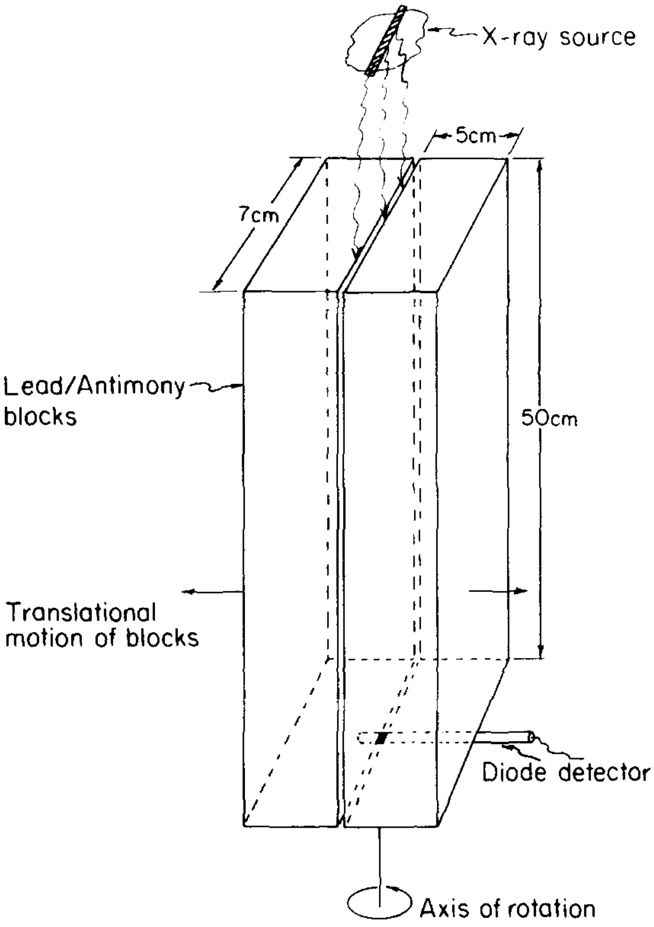

FIGURE 3.10: A schematic diagram of the slit collimator apparatus used in Munro, Rawlinson, and Fenster, 1988 and Jaffray et al., 1993 for measuring the X-ray intensity distribution of linear accelerators. Adapted by Munro, Rawlinson, and Fenster, 1988 with AIP permission.

accelerators (figure 3.11). They also repeated the measurements at different times on the same machines to investigate if the sources have changed or moved. The results showed that the Varian sources presented sources ranging in FWHM from 0.9 to 1.6 mm and confirmed the elliptic nature of the distribution. The Siemens accelerator sources had FWHM ranging from 0.7 to 1.2 mm, while the Therac machines from 0.5 to 3.4 mm. The Varian accelerators presented high stability, as the source distribution changed only marginally, despite the fact that the accelerators were continuously used in the clinic during that time. The position of the source distribution appear to change as the accelerator energy is switched from 6 MV to 18 MV.

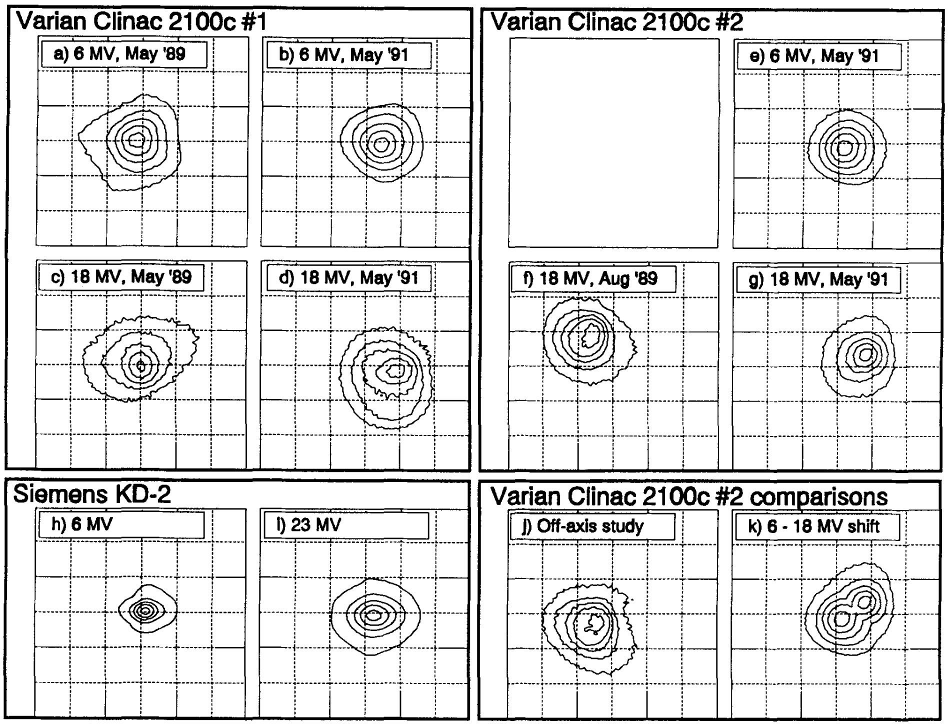

FIGURE 3.11: X-ray sources measured by Jaffray et al., 1993 using the slit collimator technique for Varian and Siemens linear accelerators. Measurements were repeated about 2 years later and as the nominal energy switched on the same accelerator. Adapted with AIP permission.

The researchers also attempted to estimate the extra-focal radiation, referring to the contribution of scatter sources such as the primary collimator and flattening filter, by performing measurements at an extended SSD of 245 cm. Additional Pb collimators of varying diameter were placed at an SSD of 150 cm to reduce the contribution of scattered radiation from the secondary collimators. As the Pb collimator diameter increases the measured signal is expected to increase mainly due the contribution of these scatter sources. The reported results indicated that approximately 8 % of the accelerator output should be attributed to extra-focal radiation.

In a more recent study Caprile and Hartmann, 2009 applied the slit collimator technique to measure the source distribution of a TomoTherapy accelerator. They determined a FWHM of 0.5 mm close to the sources measured by Jaffray et al., 1993 for a Siemens accelerator. The reconstructed source was subsequently used as an input to a convolution/superposition algorithm to calculate output factor and dose profiles. The beam model was capable of reproducing the OFs and dose profiles within the acceptance criteria of 2%/2 mm relative to measured data for large and small fields.

A slightly different slit collimator technique was performed by Loewenthal et al., 1992 and by Sham et al., 2008. In these studies the slit collimator was translated laterally and the focal spot distribution was determined through an analysis of the total and background signal. An interesting observation in the study by Sham et al., 2008 was that the source distribution appeared to be better described by a Pearson type VII peak function instead of a Gaussian distribution. The above result raises perhaps some questions whether the Gaussian distribution, commonly assumed as the source distribution in TPS and Monte Carlo beam models, is an adequate approximation. The resulting FWHM for a Varian Clinac was found to be about 1.54 mm in agreement with the reported values in the Jaffray et al., 1993 study for Varian accelerators.

In a study by Chen et al., 2011 the impact of the slit width, height and distance from the source was investigated. In general, it was recommended to minimize the slit width and maximize its height to increase measurement resolution. Furthermore, the slit collimator should be placed as close to the source as possible. However, technical challenges may become a limiting factor: reducing the slit will reduce also the signal-to-noise ratio and the slit collimator can not be placed too close to the source due to the existence of linac MLCs or covers. The researchers note that an erroneous choice of the parameters settings may lead to a significant over-estimation of the actual source size.

The above discussion highlights the complexity of the slit collimator method with difficulties rising in both the experimental apparatus and the set-up parameters used. Probably these differences have kept the slit collimator technique away from routine clinical practice. Treuer et al., 1993 suggested an alternative path which avoided the use of specialized equipment. In that work the source was reconstructed using information from dose profiles measured in water. The dose profiles were first deconvolved using a pre-calculated pencil beam kernel to acquire the expected photon fluence profile. The source distribution can be calculated by applying the inverse Abel transform on the first derivative of the fluence profiles. An intensity modulation function and an aperture function were applied to simulate the blurring due to the presence of a compensator and the effect of the field size. The reported FWHM of the sources of a Mevatron 77 and an SL 75/20 accelerator were found to be 2.54 mm and 4.63 mm respectively. The source intensity distribution was found to be better described by a double-Gaussian function. The Gaussian with the smaller variance was interpreted as the direct source and the Gaussian with the larger variance as the contribution from the flattening filter and other scatter sources.

3.3.2 Indirect reconstruction techniques

Indirect methods are defined here as the methods that establish a relationship between a dosimetric effect, such as penumbra width or output factor and and the source size. Thus, the source size can be determined by a sensitivity curve that characterizes this relationship.

Zhu, Bjärngard, and Shackford, 1995 evaluated the drop in output factor as the collimation field is reduced as a sensitive parameter to quantify the source size. Larger sources are expected to present a larger drop due to increased source occlusion. Measurements were performed in air using a diode and a lead cap to provide electron equilibrium. The field sizes were formed by gradually closing one collimator block, while keeping the opposing at 0.5 cm distance from the central axis. The inner collimation jaws (inplane) residing closer to the source were used to increase the sensitivity of the method. Assuming that the source distribution can be described by the sum of two Gaussian functions (one for the primary photons and the other for the scattered photons) and integrating it in the region projected on the source plane from the inner collimator opening, the output ratios can be expressed as the sum of two error functions. The model parameters (the two Gaussian variances and their relative contribution) can then be determined by non-linear curve fitting. They inferred that such a curve could be used as a source characteristic curve for quality assurance procedures.

The researchers applied this method on a Phillips SL75-5, a Phillips SL25 and a Varian 6/100 accelerator and determined the FWHM of the direct source in the range of 1.2 - 2.1 mm and the FWHM of the indirect source in the range of 13-17 mm. The relative ratio of indirect to direct contribution was between 6.8 - 9 %.

Treuer et al., 2003 used the microMLC to relate grid field dose profile measurements with the spot size. The grid fields were formed by keeping every second leaf of the microMLC open and the rest closed. Two Gaussian envelopes were segmented on the peaks and valleys of the measured grid profiles. The researchers observed a linear relationship between the ratio of the envelopes maxima and minima and the spot size by performing computer simulations. They inferred that such a curve could be used as a source characteristic curve for quality assurance procedures.

Wang and Leszczynski, 2007 used a Monte Carlo beam model to determine the source size and shape of a Siemens Primus accelerator. The researchers used the increase in penumbra width of dose profiles as the sensitive effect for estimating the source size. Dose profile calculations were performed in water using the BEAMnrc and DOSXYZnrc MC codes for electron source FWHM values ranging from 0.5 to 1.8 mm. From the calculated profiles the 80 - 20 % penumbra widths were extracted and a sensitivity curve was derived relating the penumbra width to the electron source FWHM. Profile measurements were performed at the same depth and the source size was estimated by the MC-derived sensitivity curve. The authors determined an electron FWHM of 1.1 mm for the crossplane and 1.7 mm for the inplane profiles, indicating a highly elliptical source distribution. A similar procedure was followed for the photon source (focal spot). In that case the sensitivity curves related the penumbra width to the photon source FWHM calculated at the exit of the target. The photon FWHM was found to be 3.2 mm and 3.7 mm for the crossplane and inplane profiles respectively. The researchers noted that the extracted photon FWHM appeared to be much larger than most values reported in the previous direct reconstruction studies. This discrepancy was attributed to the different planes were photon sources are reported in the various studies.

The non-consistency in the photon source reporting may lead to confusion. In the study by Wang and Leszczynski, 2007 the photon source was reported at the bottom of the target, at 2.3 mm from the incident electron source, but in other studies the thickness of the target may vary. This would result in differences between the reported source sizes mainly due to the divergence of the photon beam. There is also often a confusion in the literature if the reported source refers explicitly to the electron source incident on the target or to the generated photon source at some other plane (Scott, Nahum, and Fenwick, 2009).

Sterpin et al., 2011 performed a thorough investigation on the production of the primary photon source in the target and its relationship with the electron source. They studied targets of thicknesses of 1.5 mm and 1 cm, electron energies of 3, 5.5 and 18 MeV and electron source sizes of FWHM of 0.0, 0.5, 1.0 and 1.5 mm. Bremsstrahlung photons produced in the target were collected in the plane underneath the target. The photon source position could then be estimated by backprojecting all the photons with trajectories intersecting a 45 × 45 cm^2 plane at 85 cm SSD (figure 3.12). The photon fluence distribution was then reconstructed in various planes up to 5 mm above the target. The virtual source position and distribution was considered to be at the plane that the reconstructed FWHM was minimal.

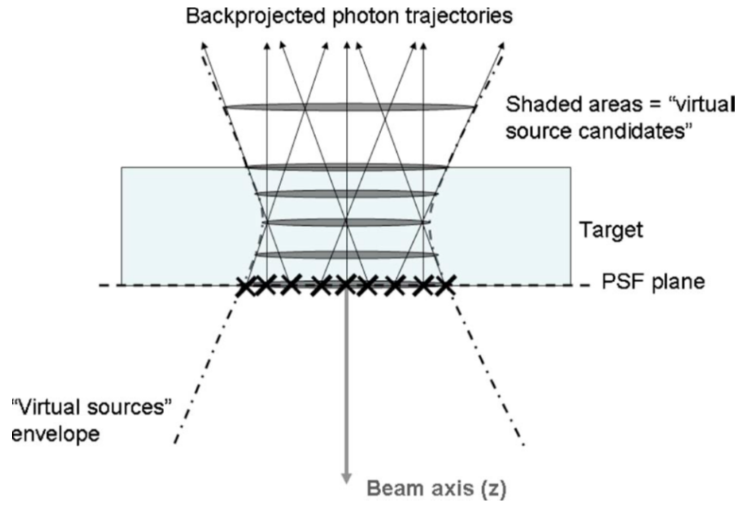

FIGURE 3.12: The virtual source position and distribution can be estimated by backprojecting photons from the bottom of the target upwards. The position that minimizes the FWHM of the reconstructed distribution can be considered as the virtual source position. Adapted by Sterpin et al., 2011 with AIP permission.

The results of that study exhibited that the photon source was basically generated within the first 0.13 mm of the target for the low energies (3 and 5.5 MeV) and within 0.25 mm for the high energy beams (18 MeV). The exact position was difficult to estimate since the FWHM values varied by less than 0.01 mm within a depth range of 0.5 mm in the target. However, the photon size would be significantly increased by beam divergence for planes downstream the target reaching 2.5 and 5 times its size for planes residing at 5 mm and 1 cm respectively from of the top of the target. The photon FWHM appeared to be close to the incident electron source FWHM in all cases, but broader by 0.02 mm to 0.06 mm. The researchers concluded that, with good approximation, the photon source of a clinical, linear accelerator can be considered very close in size to the electron source and that its virtual position can be estimated to be close to the beginning of the target. In fact if the effect of scattering sources can be removed then a direct measurement of the photon source could be considered as a measurement of the incident electron source as well. The above statement implies that if the previously reported sources using direct reconstruction techniques, such as a slit collimator, are used as an input to a MC beam model, which most often starts from the electron source incident on the target, then the dose distributions should be close to measurements and no further tuning would be required. Sham et al., 2008 did exactly that by performing a MC simulation using a Gaussian electron source of FWHM equal to 1.5 mm to approximate the reconstructed photon source of FWHM equal to 1.54 mm that was determined in that study. They reported good agreement between simulations and measurements for dose profiles and percent depth dose distributions.

Chapter 4

On the correction, perturbation and modification of small field detectors in relative dosimetry

Pavlos Papaconstadopoulos, Frederic Tessier and Jan Seuntjens Phys. Med. Biol. 59 (2014) 5937 - 5952

In this study on-axis and off-axis correction factors are extracted using Monte Carlo calculations for modern dosimeters including a liquid ionization chamber, an unshielded diode, a synthetic diamond and a plastic scintillator. The reported correction factors can be applied directly on the detector-specific output factors to improve the accuracy of relative dosimetry. In addition, component-specific perturbation factors for each detector system are reported and the design of some of the detectors is optimized to minimize the overall correction required.

Abstract The purpose of this study was to derive a complete set of correction and perturbation factors for output factors ($\mathrm{OF}_{\mathrm{det}}$) and dose profiles. Modern small field

detectors were investigated including a plastic scintillator (Exradin W1, SI), a liquid ionization chamber (microLion 31018, PTW), an unshielded diode (Exradin D1V, SI) and a synthetic diamond (microDiamond 60019, PTW). A Monte Carlo (MC) beam model was commissioned for use in small fields following two commissioning procedures: 1) using intermediate and moderately small fields (down to 2×2 cm^2) and 2) using only small fields (0.5×0.5 - 2×2 cm^2). In the latter case the detectors were explicitly modeled in the dose calculation. The commissioned model was used to derive the correction and perturbation factors with respect to a small point in water as suggested by the Alfonso formalism. In MC calculations the design of two detectors was modified in order to minimize or eliminate the corrections needed. The results of this study indicate that a commissioning process using large fields does not lead to an accurate estimation of the source size, even if a $2{\times}2$ cm^2 field is included. Furthermore, the detector should be explicitly modeled in the calculations. On the output factors, the scintillator W1 needed the smallest correction (+0.6%), followed by the microDiamond (+1.3%). Larger corrections were observed for the microLion (+2.4%) and diode D1V (-2.4%). On the profiles, significant corrections were observed out of the field on the gradient and tail regions. The scintillator needed the smallest corrections (-4%), followed by the microDiamond (-11%), diode D1V (+13%) and microLion (-15%). The major perturbations reported were due to volume averaging and high density materials that surround the active volumes. These effects presented opposite trends in both $\mathrm{OF}_{\mathrm{det}}$ and profiles. By decreasing the radius of the microLion to 0.85 mm we could modify the volume averaging effect in order to achieve a discrepancy less than 1% for of and 5% for profiles compared to water. Similar results were observed for the diode

D1V if the radius was increased to 1 mm.

4.1 Introduction

In modern radiation therapy small fields are often used during stereotactic radiosurgery (SRS), stereotactic body radiation therapy (SBRT) or intensity modulated radiation therapy (IMRT). However, several investigators have raised attention on the dosimetry in non-equilibrium conditions. Some of the major problems in small field dosimetry are a result of the partial occlusion of the X-ray source and the loss of charged particle equilibrium (Aspradakis, 2010). In addition, non-water materials and the finite size of the detector's active volume will often result in perturbations and volume averaging. Up to date, there has not been a detector that could reproduce the dose in a point in water and detector-specific corrections are needed. Otherwise, the measurement of detector-specific output factors ($\mathrm{OF_{det}}$) will be erroneous and this will propagate as a systematic error in the treatment planning system during beam commissioning.

Alfonso et al., 2008 have presented a formalism for the correction of the ratio of the detector reading in a small clinical (clin) field ($\mathrm{M^{f_{clin}}_{Q_{clin}}}$) to a larger, machine specific reference (msr) field ($\mathrm{M^{f_{msr}}_{Q_{msr}}}$). In this work we will refer to this ratio as the detector output factor ($\mathrm{OF_{det}}$). Based on this protocol, the output factor should be corrected by a detector-specific correction factor $\mathrm{k^{f_{clin},f_{msr}}_{Q_{clin},Q_{msr}}}$ in order to provide the field factor

$\Omega^{f_{clin},f_{msr}}_{Q_{clin},Q_{msr}}$ (equation 4.1).

$$\Omega^{f_{clin},f_{msr}}_{Q_{clin},Q_{msr}} = \frac{M^{f_{clin}}_{Q_{clin}}}{M^{f_{msr}}_{Q_{msr}}} \cdot k^{f_{clin},f_{msr}}_{Q_{clin},Q_{msr}} \tag{4.1}$$

In this work we will refer to the field factor as the ratio of the dose in water for the clin field to the dose in water in the msr field ($\Omega^{f_{clin},f_{msr}}_{Q_{clin},Q_{msr}} = \frac{D^{f_{clin}}_{w,Q_{clin}}}{D^{f_{msr}}_{w,Q_{msr}}}$). The $k^{f_{clin},f_{msr}}_{Q_{clin},Q_{msr}}$ factors can be accurately calculated by performing a Monte Carlo (MC) simulation of the linear accelerator and detector model. In such a case the corrections are derived as:

$$k^{f_{clin},f_{msr}}_{Q_{clin},Q_{msr}} = \frac{D^{f_{clin}}_{w,Q_{clin}}/D^{f_{clin}}_{det,Q_{clin}}}{D^{f_{msr}}_{w,Q_{msr}}/D^{f_{msr}}_{det,Q_{msr}}} \tag{4.2}$$

,where $D^{f_{clin}}_{w,Q_{clin}}$ and $D^{f_{clin}}_{det,Q_{clin}}$ are the calculated doses in a small volume of water and in the active volume of the detector in a clin field and $D^{f_{msr}}_{w,Q_{msr}}$ and $D^{f_{msr}}_{det,Q_{msr}}$ are the respective doses for the msr field. In recent years many investigators have applied this technique to derive $k^{f_{clin},f_{msr}}_{Q_{clin},Q_{msr}}$ corrections for a large number of detectors (Francescon, Cora, and Cavedon, 2008; Francescon, Cora, and Satariano, 2011; Cranmer-Sargison et al., 2011; Czarnecki and Zink, 2013; Benmakhlouf, Sempau, and Andreo, 2014). However, limited research has been presented for dose profile corrections (Crop et al., 2009). In addition, previous work was mainly targeted towards air-filled ion chambers. Off-axis positions, especially out-of-field, are also in non-equilibrium conditions and thus are expected to suffer from the same challenges as OF. In fact the problem might be even more complex due to the varying spectrum and source occlusion effect as a function of distance from the central axis.

Furthermore, there has been limited research reporting component-specific perturbations for $\mathrm{OF}_{\mathrm{det}}$ and dose profiles of modern, small field detectors (Cranmer-Sargison et al., 2012; Wagner et al., 2013). Perturbation factors are not only important for understanding the origin of the correction, but can also be used as a guide for designing future detectors, which ideally will require no correction. Underwood et al., 2013 and Charles et al., 2013 have explored this possibility by modifying the mass surrounding the active volume of diamond and diode detectors respectively.

The commissioning process for small fields also appears to be troubling. Pena et al., 2007 have suggested that the inclusion of a relatively small field profile in the commissioning process (such as a 2×2 cm^2 field) would reduce the uncertainty of the source size estimation compared to just using large field profiles. However, Scott, Nahum, and Fenwick, 2008 noticed significant discrepancies between calculated and measured output factors using an unshielded diode, even after the model was commissioned using both small and large field profiles. They also noted that any further tuning made to the model in order to reduce the discrepancy with the diode would result in discrepancies with a pinpoint air-filled chamber. In principle, if the actual source size is determined, the detectors are properly modeled, and the particle transport is accurately simulated (such as in MC codes), the output factors should agree in all cases, even for small fields.

The purpose of this work is fourfold: 1) To establish if a commissioning procedure using intermediate and moderately small fields (down to 2×2 cm^2) is adequate for proper small field commissioning. Also, to verify if the detector should be explicitly

TABLE 4.1: Detector active volume specifications. The manufacturers are reported in the parenthesis.

Detector	radius (mm)	length (mm)	medium	ρ ($g \cdot cm^{-3}$)
scintillator W1 (SI)	0.50	3.000	polystyrene	1.05
diode D1V (SI)	0.50	0.050	silicon	2.33
microLion (PTW)	1.25	0.350	iso-octane	0.69
microDiamond (PTW)	1.10	0.001	diamond	3.50
point in water	0.15	0.300	water	1.00

modeled during the commissioning. 2) To derive a set of output factor and profile corrections for modern small field dosimeters including a plastic scintillator, a liquid ion chamber, an unshielded diode and a synthetic diamond, 3) to derive a detailed set of perturbation factors for on-axis and off-axis positions and finally 4) to suggest, based on the reported perturbations, simple modifications to some of the detector designs that would minimize or eliminate the need for applying corrections.

4.2 Methods

4.2.1 Detectors

The detectors investigated in this work included a plastic scintillator (Exradin W1, SI), an unshielded diode (Exradin D1V, SI), a liquid ionization chamber (microLion 31018, PTW) and a synthetic diamond (microDiamond 60019, PTW). All detectors are commercially available and recommended for use in small fields. The active volume of the scintillator W1 is composed of polystyrene. It has a cylindrical shape with a radius of 0.5 mm and a length of 3 mm. The scintillator is coupled with a plastic optical fiber which transfers the signal to a photodiode. During irradiation Cherenkov radiation is produced in the optical fiber. Experimentally derived corrections are needed to be applied to account for this effect as a function of field size. The active volume of the diode D1V is composed by silicon and has a cylindrical shape with a radius of 0.5 mm and length of 50 μm. The active volume is embedded in a silicon substrate and surrounded by a plastic (C552) wall. The microLion's active volume is composed by iso-octane and has a cylindrical shape with a radius of 1.25 mm and length of 0.3 mm. It is surrounded by a graphite electrode. The microDiamond detector is a synthetic single crystal detector. The active volume embedded in the diamond crystal has a cylindrical shape of radius of 1.1 mm and length of 1 μm.

The diode D1V, microLion and microDiamond are recommended to be placed parallel to the central axis (CAX) when measuring $\mathrm{OF}_{\mathrm{det}}$ and profiles. In such orientation the diameter of the active volume becomes the detector's limiting resolution. The scintillator W1 can be positioned either perpendicularly to the CAX (in a solid water phantom) either parallel to the CAX in a water tank. In the former orientation the limiting resolution is 3 mm and in the latter 1.0 mm. Table 4.1 presents a summary of the specifications of each detector's active volume.

4.2.2 Monte Carlo simulations settings and parameters

The EGSnrc/BEAMnrc (Rogers et al., 1995) MC code was used for the modeling of a Varian Novalis Tx linear accelerator. The fields were defined by the secondary collimator jaws as projected at a source to surface distance (SSD) of 100 cm. The Bremsstrahlung Splitting variance reduction technique was used with a splitting number of 1000. An elliptical gaussian distribution was chosen as the electron source incident on the target. For the accelerator simulation part the electron (ECUT) and photon

(PCUT) cut-off values were set to 700 and 10 keV respectively. For the commissioning using intermediate fields, the EGSnrc/DOSXYZnrc code (Walters, Kawrakow, Rogers, et al., 2005) was used for the dose calculation part with an ECUT=521 keV. For the calculations where the detector was explicitly modeled and for the dose in a point in water, the egs_chamber code (Kawrakow et al., 2009) was used with an ECUT=512 keV. The detectors were modeled based on technical sketches provided by the manufacturers. An intermediate phase-space file was used to save the particles around all possible detector positions. The cross-section enhancement technique (CSE) was applied within a cylindrical shell of water surrounding the detector by at least 1 cm with a CSE factor of 256 (Wulff, Zink, and Kawrakow, 2008). The number of histories varied according to the field size in order to achieve a statistical uncertainty better than 0.3% on the deposited dose in the active volume on the CAX. Both cross-plane and in-plane profiles were calculated with a resolution of 1 mm.

4.2.3 Commissioning of the MC beam model

An initial commissioning procedure was followed using intermediate and moderately small fields. Percent depth doses (PDDs) were measured for a 5×5 cm^2 and 10×10 cm^2 field size using a Farmer type chamber (IBA CC-13) with a scanning resolution of 1 mm. The data were shifted to the effective point of measurement. Profiles of a 2×2, 5×5 and 10×10 cm^2 were measured using the microLion. The operating voltage was set to +800 V to reduce ion recombination effects. Dose rate dependence effects were corrected as suggested by Chung, Davis, and Seuntjens, 2013. The profiles were measured 3 times, each time repositioning the jaws. For the PDDs the voxel geometry was chosen to be $2.5 \times 2.5 \times 1$ mm^3 and for the profiles $2.5 \times 2.5 \times 0.3$ mm^3. The commissioning process started by determining the energy from the PDD curves and the angular spread by the 10×10 cm^2 profile similarly to the methodology presented by Almberg et al., 2012. As a second step the source's Full Width Half Maximum (FWHM) was tuned in the cross-plane (x) and in-plane (y) direction, in order to achieve good agreement with the 2×2 cm^2 and 5×5 cm^2 profiles. The 10×10 cm^2 profile was repeated to verify that it still agrees with measurements after tuning the source.

The second commissioning procedure included only small field profiles (0.5×0.5, 1×1 and 2×2 cm^2). The measurements were performed 4 times (within a period of approximately 4 months) using the microLion and the unshielded diode D1V. Each set included 4 profile scans and output factor measurements. Therefore, the total standard deviation presented on each point included the jaw and detector re-positioning uncertainties as well as possible time evolution changes of the source. For the dose calculation part the detectors were explicitly modeled using the egs_chamber code. The source's FWHM(x,y) was initially set to the values found in the large field commissioning process and then was further tuned until both detector measurements agreed with their respective simulations within the reported uncertainties.

All profiles and output factors were measured at a depth of 5 cm and for a SSD of 100 cm. Each profile was flipped and then averaged in order to account for beam asymmetries.

4.2.4 Correction factors

Output factor corrections

$\mathrm{k}^{\mathrm{f_{clin}},\mathrm{f_{msr}}}_{\mathrm{Q_{clin}},\mathrm{Q_{msr}}}$ output factor corrections were derived for the detectors exhibited in table 4.1. The corrections were calculated following the Aflonso protocol (eq.4.2) for field sizes of 0.5×0.5, 1×1 and 2×2 cm^2. The msr field was the 10×10 cm^2. The main properties of the detectors have been presented in section 2.1 and in table 4.1. A cylindrical voxel of radius of 0.15 mm and length of 0.3 mm was considered to be the point in water. A further reduction of the water voxel, in either dimensions, did not exhibit any statistically significant differences in $\mathrm{OF_{det}}$ or profiles. All detectors were placed parallel to the CAX, as suggested by the manufacturers. For the case of the W1 scintillator, output factor measurements can also be performed in solid water with the detector oriented perpendicular to the CAX. Since this is an attractive clinical option we have calculated corrections for that orientation as well.

Profile corrections

In a similar fashion as the $\Omega^{fclin,fmsr}_{Qclin,Qmsr}$ field factor, we can define an off-axis factor, $O^{fclin(d),fclin(0)}_{Qclin(d),Qclin(0)}$, which would provide the relative dose in a perpendicular off-axis distance d (d=x or y) normalized to the dose on the central axis (d=0) for the same clinical field $\mathrm{f_{clin}}$:

$$\mathrm{O}^{\mathrm{fclin(d),fclin(0)}}_{\mathrm{Qclin(d),Qclin(0)}} = \frac{\mathrm{M}^{\mathrm{fclin(d)}}_{\mathrm{Qclin(d)}}}{\mathrm{M}^{\mathrm{fclin(0)}}_{\mathrm{Qclin(0)}}} \cdot \mathrm{k}^{\mathrm{f_{clin}(d),f_{clin}(0)}}_{\mathrm{Q_{clin}(d),Q_{clin}(0)}} \tag{4.3}$$

Following a similar nomenclature as in the Alfonso protocol, the off-axis corrections can be defined as:

$$\mathrm{k}^{\mathrm{f_{clin}(d),f_{clin}(0)}}_{\mathrm{Q_{clin}(d),Q_{clin}(0)}} = \frac{\mathrm{D}^{\mathrm{f_{clin}(d)}}_{\mathrm{w,Q_{clin}(d)}}/\mathrm{D}^{\mathrm{f_{clin}(d)}}_{\mathrm{det,Q_{clin}(d)}}}{\mathrm{D}^{\mathrm{f_{clin}(0)}}_{\mathrm{w,Q_{clin}(0)}}/\mathrm{D}^{\mathrm{f_{clin}(0)}}_{\mathrm{det,Q_{clin}(0)}}} \tag{4.4}$$

,where $\mathrm{D}^{\mathrm{f_{clin}(d)}}_{\mathrm{w,Q_{clin}(d)}}$ and $\mathrm{D}^{\mathrm{f_{clin}(d)}}_{\mathrm{det,Q_{clin}(d)}}$ are the calculated doses in the point in water and in the active volume of the detector in a perpendicular off-axis distance d and $\mathrm{D}^{\mathrm{f_{clin}(0)}}_{\mathrm{w,Q_{clin}(0)}}$ and $\mathrm{D}^{\mathrm{f_{clin}(0)}}_{\mathrm{det,Q_{clin}(0)}}$ are the respective doses for the same clinical field on the CAX. Profile corrections were calculated for field sizes of 0.5×0.5, 1×1 and 2×2 cm^2 for the detectors presented in table 4.1.

4.2.5 Perturbation factors

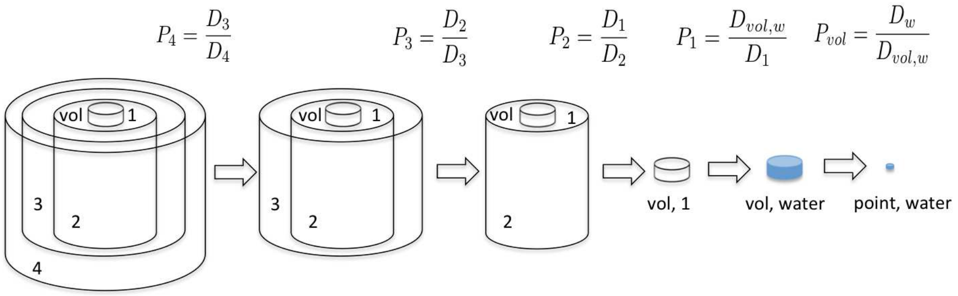

FIGURE 4.1: The chain technique for deriving perturbation factors for a simplistic detector model

The perturbation factors were derived by the chain technique, as has been described by previous researchers (Seuntjens and Rogers, 2009; Bouchard et al., 2009a). On this technique each detector material component is replaced gradually by water, starting from the outermost layer down to the active volume. The perturbation of a specific component layer j can thus be calculated as:

$$P_j = \frac{D_{j-1}}{D_j} \tag{4.5}$$

,where D_j is the dose deposited with the j-th layer present and j-1 with the j-th layer removed and replaced with water (fig. 4.1). At the final step the volume perturbation can be calculated as $P_{vol} = \frac{D_w}{D_{vol,w}}$, where $D_{vol,w}$ is the dose deposited in the active volume in water and D_w is the dose deposited in a point in water. The conversion of the material in the active volume to water (P_1 in fig. 4.1) should be better understood as the product of the cavity (or fluence) perturbation and the restricted stopping power ratio of the water to medium ($P_1 = P_{med} = (\frac{\bar{L}}{\rho})^{w}_{med} P_{cav}$) and not as a true perturbation.

The product of all perturbation factors will result in the total perturbation caused by replacing the detector with a point in water:

$$\prod_{j=1}^{N} P_j P_{vol} = \frac{D_{N-1} D_{N-2} \ldots D_1 D_{vol,w} D_w}{D_N D_{N-1} D_{N-2} \ldots D_1 D_{vol,w}} = \frac{D_w}{D_N} \tag{4.6}$$

,where N= total number of material layers and $D_N = D_{det}$. Thus, the $k^{f_{clin},f_{msr}}_{Q_{clin},Q_{msr}}$ factors can be linked with the perturbations by the following relationship:

$$k^{f_{clin},f_{msr}}_{Q_{clin},Q_{msr}} = \frac{(\prod_{j=1}^{N} P_j P_{vol})^{f_{clin}}_{Q_{clin}}}{(\prod_{j=1}^{N} P_j P_{vol})^{f_{msr}}_{Q_{msr}}} = \prod_{j=1}^{N} P^{f_{clin},f_{msr}}_{j,Q_{clin},Q_{msr}} P^{f_{clin},f_{msr}}_{vol,Q_{clin},Q_{msr}} \tag{4.7}$$

,where $P^{f_{clin},f_{msr}}_{Q_{clin},Q_{msr}}$ is the relative perturbation in the clin field to the respective perturbation in the msr field. In a similar manner the off-axis perturbations can be linked to the off-axis corrections $k^{f_{clin}(d),f_{clin}(0)}_{Q_{clin}(d),Q_{clin}(0)}$ by the following equation:

$$k^{f_{clin}(d),f_{clin}(0)}_{Q_{clin}(d),Q_{clin}(0)} = \frac{(\prod_{j=1}^{N} P_j P_{vol})^{f_{clin(d)}}_{Q_{clin(d)}}}{(\prod_{j=1}^{N} P_j P_{vol})^{f_{clin(0)}}_{Q_{clin(0)}}} = \prod_{j=1}^{N} P^{f_{clin(d)},f_{clin(0)}}_{j,Q_{clin(d)},Q_{clin(0)}} P^{f_{clin(d)},f_{clin(0)}}_{vol,Q_{clin(d)},Q_{clin(0)}} \tag{4.8}$$

,where $P^{f_{clin(d)},f_{clin(0)}}_{Q_{clin(d)},Q_{clin(0)}}$ is the relative perturbation at the off-axis distance d to the respective perturbation at the CAX. The relative perturbation factors $P^{f_{clin},f_{msr}}_{Q_{clin},Q_{msr}}$ and $P^{f_{clin(d)},f_{clin(0)}}_{Q_{clin(d)},Q_{clin(0)}}$ were calculated for all detectors presented in Table 4.1 for the smallest field size (0.5×0.5 cm^2) and for both cross-plane and in-plane directions.

4.2.6 Modification of detector geometries

Modified geometries of the PTW microLion and Exradin D1V diode were created by varying the radius of the active volume from 0.5 up to 1.25 mm for the smallest field size of 0.5×0.5 cm^2. Small fields present regions of steep gradients, even within the active volume. An increase in the detector's radius on the scanning direction is expected to increase the volume averaging effect (P_{vol}) and consequently reduce the OF_{det} and increase the penumbra. Thus, this effect could be enhanced or reduced according to the specific material perturbations to be compensated. Ideally, this could result in a minimal overall correction. The $k^{f_{clin},f_{msr}}_{Q_{clin},Q_{msr}}$ and $k^{f_{clin}(d),f_{clin}(0)}_{Q_{clin}(d),Q_{clin}(0)}$ corrections were recalculated for the modified geometries and compared with the previous results of the actual detector designs.

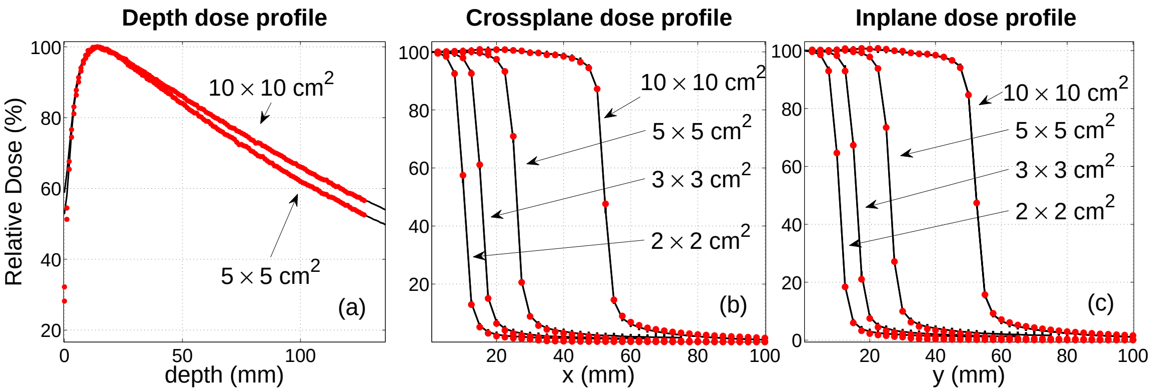

FIGURE 4.2: Comparison of the MC beam model (circles) to measurements (lines) for depth (a), cross-plane (b) and in-plane (c) profiles and for field sizes ranging from 2×2 up to 10×10 cm^2. The detectors were not explicitly modeled in these calculations.

4.3 Results

Figure 4.2 presents the profile comparison of the MC beam model to the measurements after commissioning using the 2×2, 5×5 and 10×10 cm^2 field sizes. A 3×3 cm^2 field size was also calculated for verification of the model. The agreement was within 0.5% in most of the points. The parameter values were found to be: FWHM (x) = 0.9 mm, FWHM (y) = 1 mm, energy = 6.1 MeV and angular spread = 1^o.

Figure 4.3 presents the profile comparison between MC simulations and measurements after commissioning using only the 0.5×0.5, 1×1 and 2×2 cm^2 field sizes. The detectors were explicitly modeled in the dose calculation and the measurements were compared to the calculated dose deposited within the active volume of the corresponding detector model. The local agreement was within 3% for both detectors. The maximum discrepancies were observed in the gradient region. In this case, the optimum source size had a FWHM (x) = 1.25 mm and FWHM (y) = 1.1 mm. The energy and angular spread were not found to be sensitive parameters for the small fields.

TABLE 4.2: Comparison of Monte Carlo (MC) calculated output factors to measured values for the PTW microLion and Exradin diode D1V. Uncertainties (1 σ) are presented in the parenthesis. The field sizes are reported as projected by the secondary collimator jaws at a SSD=100 cm and as the FWHM at a depth of 5 cm.

Detector	Field (cm^2)	FWHM (cm^2)	MC	Measured	% diff
microLion	0.47×0.49	0.53×0.57	0.565 (0.002)	0.567 (0.005)	-0.4
	0.96×0.98	1.01×1.04	0.786 (0.002)	0.787 (0.001)	-0.1
	1.95×1.99	2.05×2.08	0.871 (0.002)	0.871 (0.001)	$+0.0$
diode D1V	0.47×0.49	0.52×0.55	0.592 (0.001)	0.598 (0.004)	-1.0
	0.96×0.98	1.01×1.03	0.782 (0.002)	0.775 (0.003)	$+0.9$
	1.95×1.99	2.05×2.09	0.864 (0.002)	0.851 (0.002)	$+1.5$

A 10×10 cm^2 field MC simulation was repeated using the final source size and verified that the model still agrees for large fields. Table 4.2 presents the of comparison between the MC model and the measurements.

As can be seen in fig.4.3 and table 4.2, the experimental uncertainties appear relative larger for the small fields in the gradient region and for the smallest field's $\mathrm{OF_{det}}$. This is mainly a result of the repeated measurements which included jaw and detector repositioning. The maximum local dose uncertainty was found to be about 3.5% on the gradient region close to the point where the field is defined. For the 0.5×0.5 cm^2 $\mathrm{OF_{det}}$ measurements, the total experimental uncertainty was found to be 0.9% and 0.7% for the microLion and D1V respectively.

Figures 4.4 and 4.5 present the $\mathrm{k^{f_{clin},f_{msr}}_{Q_{clin},Q_{msr}}}$ and $\mathrm{k^{f_{clin}(d),f_{clin}(0)}_{Q_{clin}(d),Q_{clin}(0)}}$ corrections for all the detectors presented in table 4.1 and for field sizes of 0.5×0.5, 1×1 and 2×2 cm^2. For the case of the scintillator, $\mathrm{k^{f_{clin},f_{msr}}_{Q_{clin},Q_{msr}}}$ factors were also performed for the perpendicular orientation in a solid water phantom. The profile corrections are presented up to approximately 3 mm out of field which corresponds to a dose level of 4 - 10% depending on the field side.

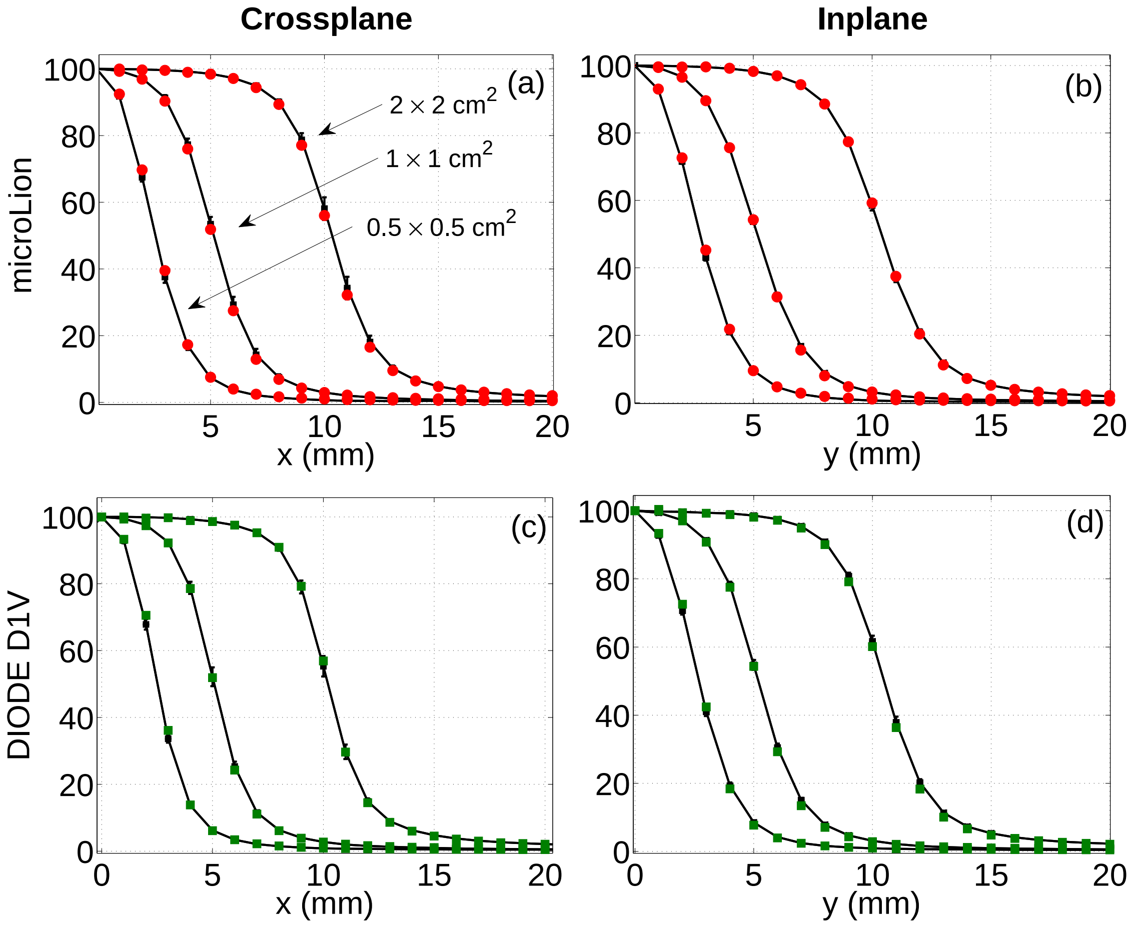

FIGURE 4.3: Comparison of the MC simulations of the dose deposited in the active volume of the PTW microLion detector (circles) and of the Exradin diode D1V (squares) to their respective measurements (lines) for the cross-plane (a,c) and in-plane (b,d) profiles and for field sizes of 0.5×0.5, 1×1 and 2×2 cm^2.

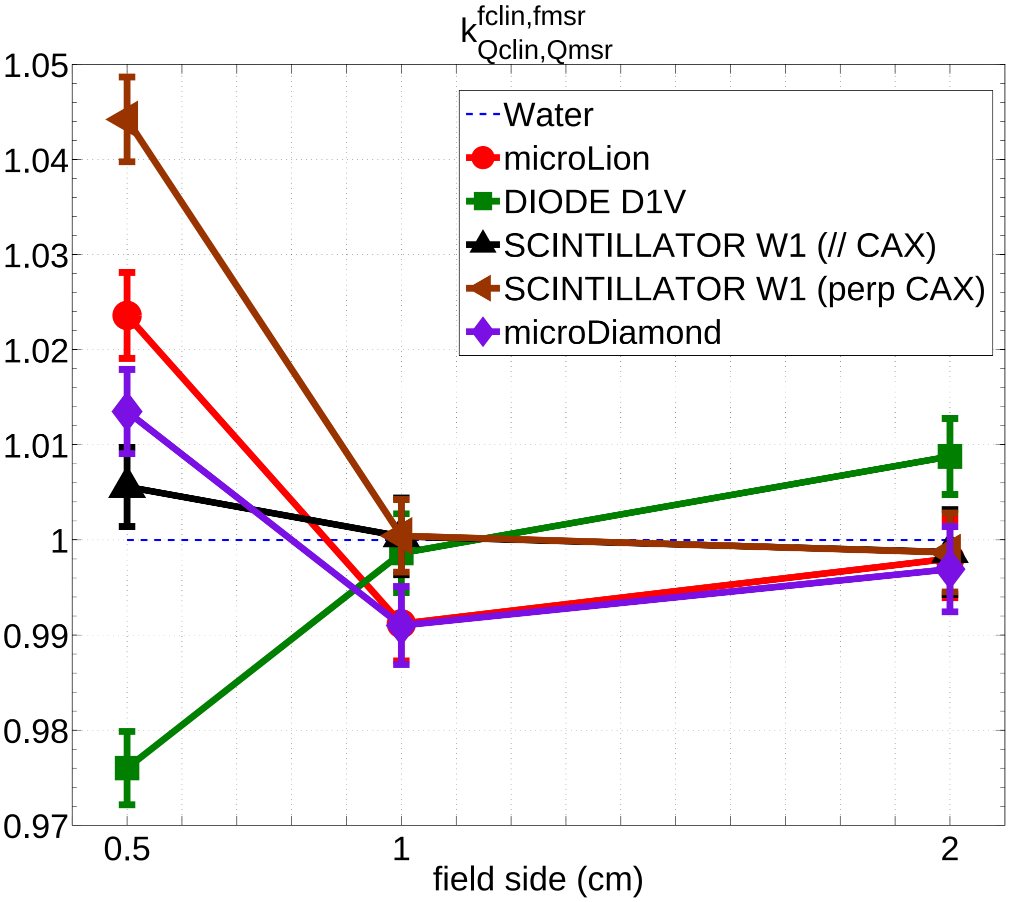

FIGURE 4.4: $k^{f_{clin},f_{msr}}_{Q_{clin},Q_{msr}}$ correction factors as a function of field side. The machine-specific reference (msr) field was the 10×10 cm^2.

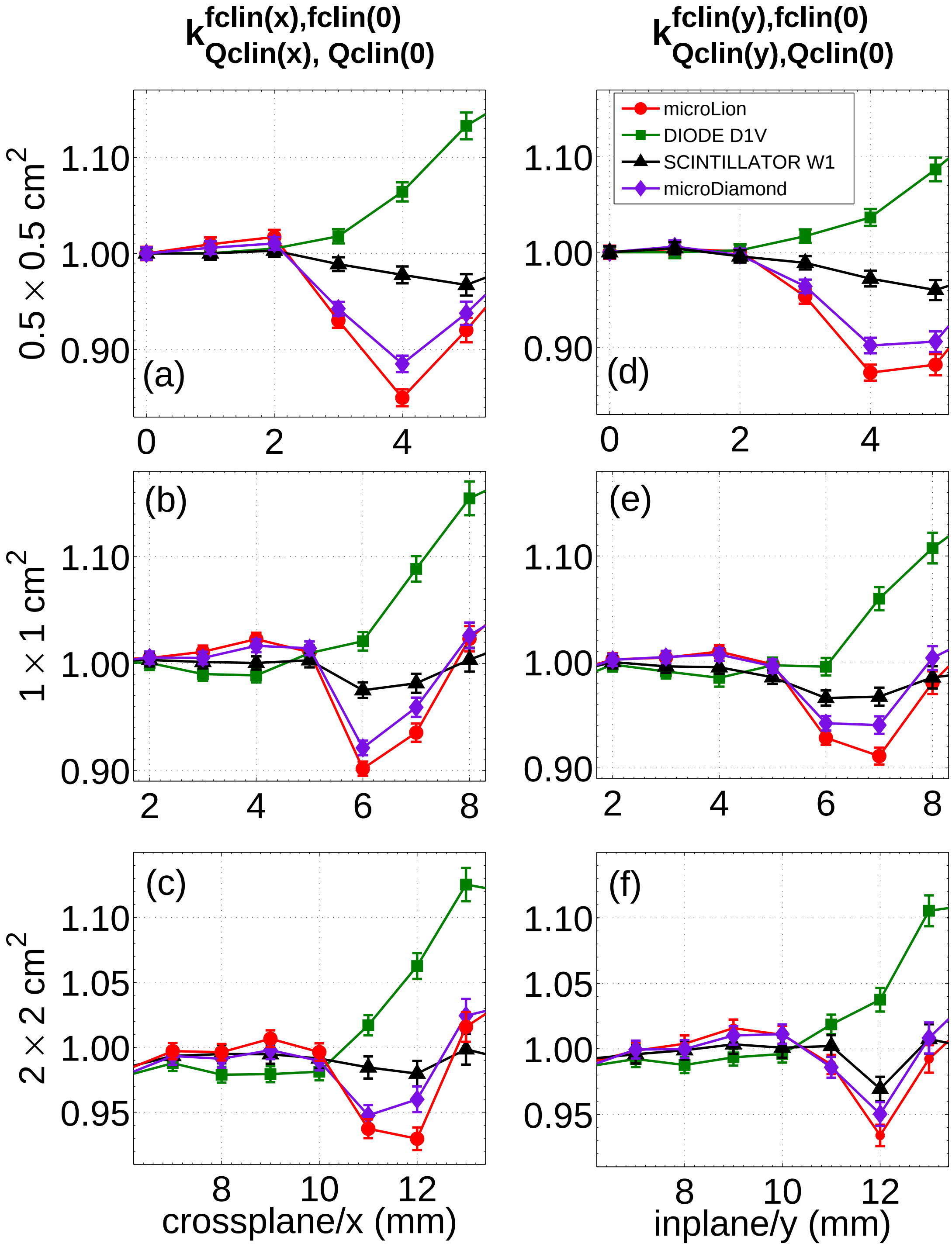

FIGURE 4.5: $k_{Q_{clin}(d),Q_{clin}(0)}^{f_{clin}(d),f_{clin}(0)}$ correction factors for the cross-plane (a - c) and in-plane profiles (d - f) as a function of off-axis distance and for field sizes of 0.5×0.5, 1×1 and 2×2 cm^2.

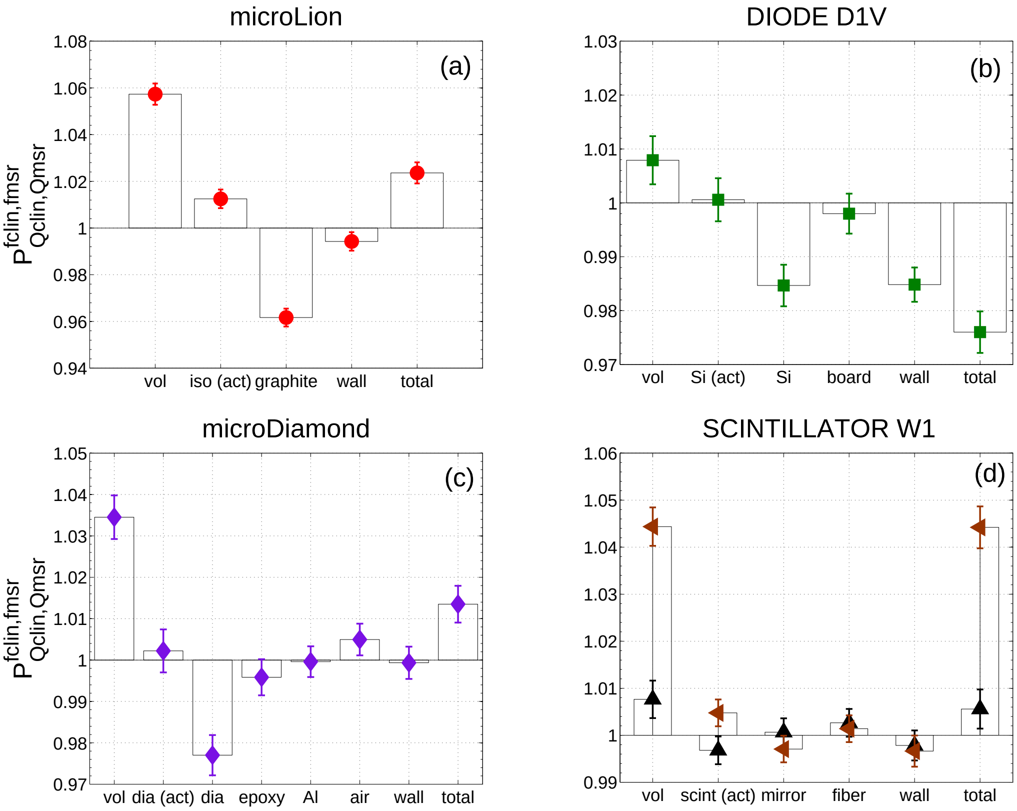

FIGURE 4.6: Relative on-axis perturbation factors, $P^{f_{clin},f_{msr}}_{Q_{clin},Q_{msr}}$ for each detector component for a field size of 0.5×0.5 cm^2. The scintillator W1 presents two cases: parallel on CAX (up triangles) and perpendicular to CAX (left triangles). The total perturbation represents the $k^{f_{clin},f_{msr}}_{Q_{clin},Q_{msr}}$. The active volumes are indicated in the parenthesis.

Figure 4.6 exhibits the relative on-axis perturbation factors $P^{f_{clin},f_{msr}}_{Q_{clin},Q_{msr}}$ for the smallest field size of 0.5×0.5 cm^2. The total perturbation is equal to the $k^{f_{clin},f_{msr}}_{Q_{clin},Q_{msr}}$ factor. Similarly, figure 4.7 exhibits the relative perturbations $P^{f_{clin(d)},f_{clin(0)}}_{Q_{clin(d)},Q_{clin(0)}}$ as a function of the off-axis distance for the cross-plane and in-plane direction. The total perturbation is equal to the $k^{f_{clin}(d),f_{clin}(0)}_{Q_{clin}(d),Q_{clin}(0)}$ factor.

Figure 4.8 presents the $k^{f_{clin},f_{msr}}_{Q_{clin},Q_{msr}}$ corrections for the PTW microLion and Exradin D1V diode as a function of the active volume radius. For comparison purposes, the actual radius of the microLion (1.25 mm) and of the D1V (0.5 mm) are also shown

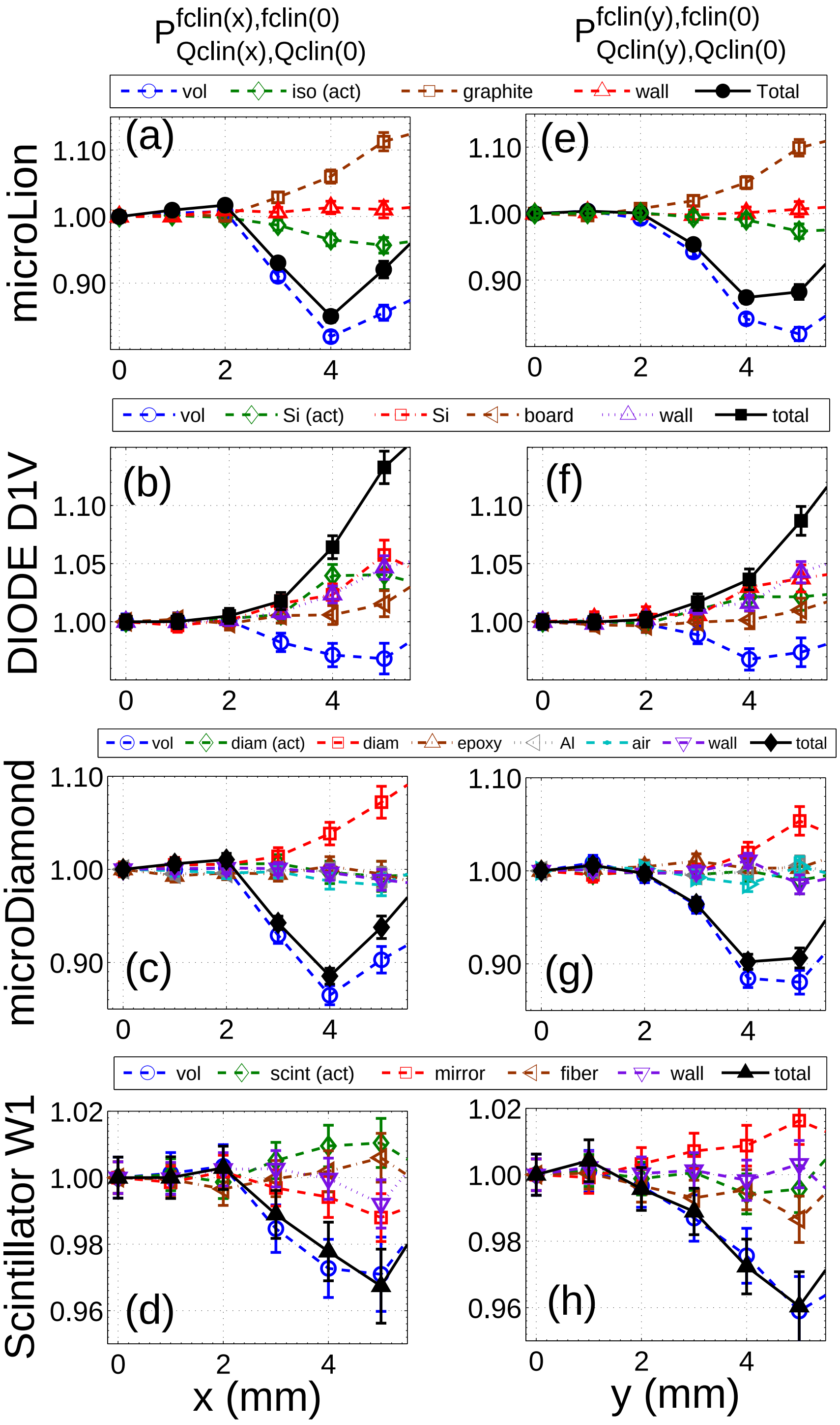

FIGURE 4.7: Relative off-axis perturbation factors, $P^{f_{\mathrm{clin(d)}},f_{\mathrm{clin(0)}}}_{Q_{\mathrm{clin(d)}},Q_{\mathrm{clin(0)}}}$, for each detector component as a function of off-axis distance for both cross-plane (a -d) and in plane (e - h) orientations. The field size was 0.5×0.5 cm^2. The total perturbation (solid lines) represent the $k^{f_{\mathrm{clin}}(d),f_{\mathrm{clin}}(0)}_{Q_{\mathrm{clin}}(d),Q_{\mathrm{clin}}(0)}$.

in the same graph. Similarly, figure 4.9 presents the results of the profile corrections $k^{f_{clin}(d),f_{clin}(0)}_{Q_{clin}(d),Q_{clin}(0)}$ for the same modified geometries. An optimum resolution can be found for both detector designs within the dashed lines which represent the 1% and 5% level of agreement, relative to the dose in a point in water, for on-axis and off-axis positions respectively.

The uncertainties of the correction and perturbation factors were calculated by the standard error propagation method of the statistical (type-A) dose uncertainties of the MC calculations. For the CAX corrections the propagated uncertainty was less than 0.5% in all cases. For the off-axis positions the propagated uncertainty was less than 1.5% in all cases. In all figures the errorbars represent the 1 standard deviation level of the propagated type-A uncertainty. Systematic (type-B) uncertainties due to cross-section and material geometry or density variations have been estimated to be less than 0.4% and 0.5% respectively for this type of calculations by Francescon, Cora, and Satariano, 2011.

4.4 Discussion

Both the large field and small field commissioning procedures (the latter including the detector model) exhibited excellent agreement with profile measurements. The small field procedure presented OF_{det} agreement within 1.5% for all field sizes for both the microLion and D1V diode. However, in the small field procedure the source size was estimated to be approximately 40% and 10% larger on the cross-plane (FWHM(x)) and in-plane directions (FWHM(y)) respectively, compared to the initial values. Repeating the calculations for the microLion model using the initial estimation of the source size, the $\mathrm{OF_{det}}$ appears over-estimated by 4.4% for the smallest field. Repeating the calculations for the final source estimation with the detector not explicitly modeled, but instead using a voxel with the exact dimensions of the microLion's active volume, the $\mathrm{OF_{det}}$ appears to be under-estimated by 5%.

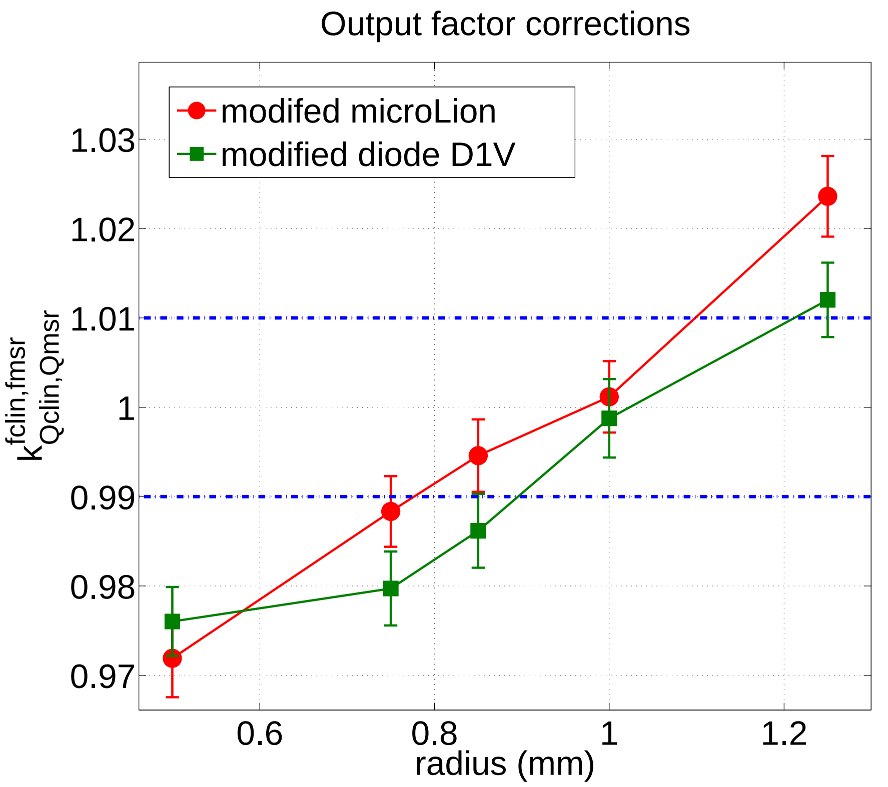

FIGURE 4.8: $\mathrm{k^{f_{clin},f_{msr}}_{Q_{clin},Q_{msr}}}$ correction factors as calculated for the modified geometries of the PTW microLion (circles) and of the Exradin diode D1V (squares). The field size was 0.5×0.5 cm^2. The resolution varied from 0.5 to 1.25 mm. The dashed lines indicate the 1 % level of agreement with a point in water.

On the $\mathrm{k^{f_{clin},f_{msr}}_{Q_{clin},Q_{msr}}}$ factors, all detectors studied in this work exhibited an agreement within 1% down to a field size of 1×1 cm^2 (figure 4.4). For the smallest field of 0.5×0.5 cm^2 larger corrections were observed. The microLion was found to under-respond by 2.4%. This result agrees, within uncertainties, with previous work by Francescon, Cora, and Satariano, 2011 and Benmakhlouf, Sempau, and Andreo, 2014 who reported

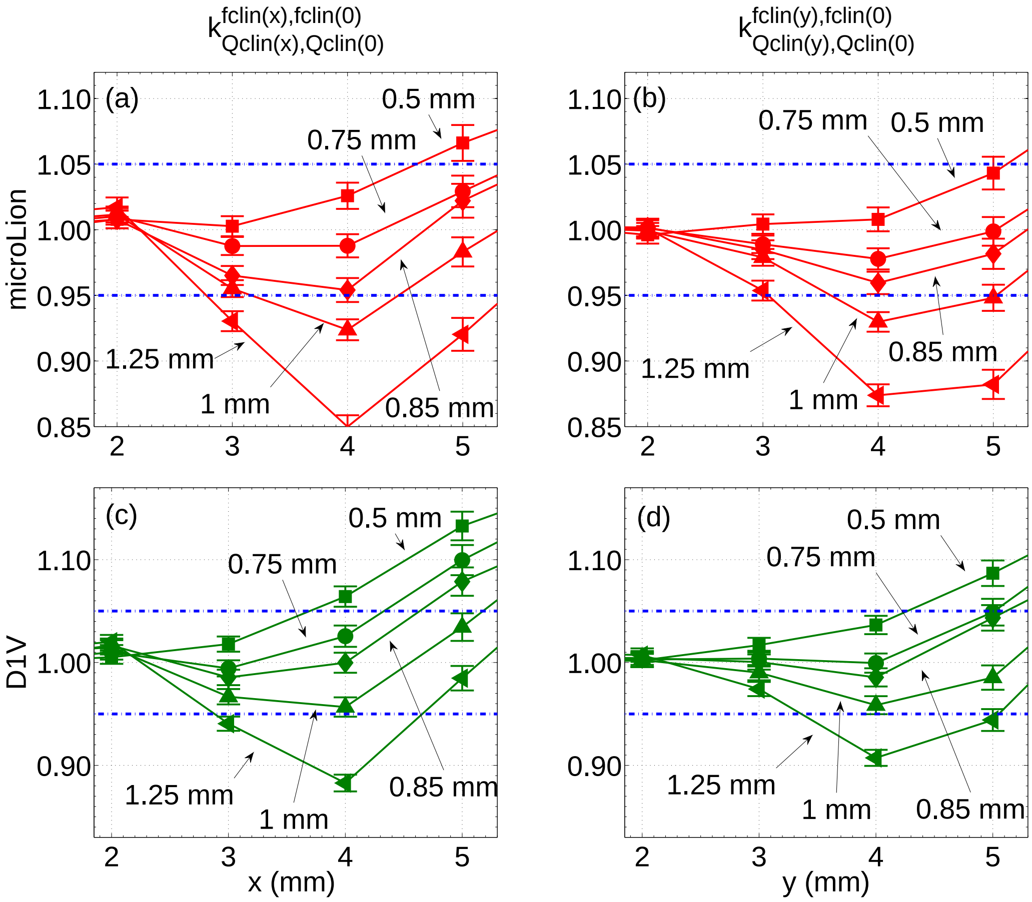

FIGURE 4.9: $k^{f_{clin}(d),f_{clin}(0)}_{Q_{clin}(d),Q_{clin}(0)}$ correction factors for the modified geometries of the microLion (a,b) and diode D1V (c,d) as a function of off-axis distance for the cross-plane (a,c) and in-plane (b,d) directions. The field size was 0.5×0.5 cm^2. The resolution varied from 0.5 to 1.25 mm. The dashed lines indicate the 5% level of agreement to a point in water.

corrections of 1.9%, 2.4% and 1.1% for a Siemens Primus, Elekta Synergy and Varian iX linear accelerators respectively. It should be noted that for the latter study the PENELOPE code (Salvat, Fernández-Varea, and Sempau, 2006) was used and the correction was reported at a depth of 10 cm (instead of 5 cm). The Exradin D1V diode was found to over-respond by 2.4% for the smallest field. This result agrees very well with a recent study by Francescon, Kilby, and Satariano, 2014 who reported a correction of

2.5% for the CyberKnife system. Smaller corrections were needed for the PTW microDiamond (+1.3%) and the Exradin scintillator W1 (+0.6%). The latter also agrees very well with Francescon, Kilby, and Satariano, 2014 who reported a +0.3% correction for the CyberKnife system. However, if the scintillator is oriented perpendicular to the CAX the correction increases to +4.4% for the smallest field size. Even though this orientation is an attractive clinical option, since measurements can be easily performed in a solid water phantom, it is not recommended for the field size of 0.5 × 0.5 cm^2. For the microDiamond detector recent experimental results have shown an over-response relative to alanine dosimeters (Azangwe et al., 2014). However, that study exhibited some systematic discrepancies with previous experimental and MC work for the smallest fields. Further research is needed for this type of detector.

On the $k^{f_{clin}(d),f_{clin}(0)}_{Q_{clin}(d),Q_{clin}(0)}$ corrections, all the detectors exhibited minimal deviations within the field. Beyond the 50% dose level, significant corrections are observed in most cases. Only the scintillator was able to fully reproduce the profile to within 4% compared to water. The microDiamond and microLion detectors over-respond ($k^{f_{clin}(d),f_{clin}(0)}_{Q_{clin}(d),Q_{clin}(0)} < 1$) out of the field by up to 11% and 15% respectively. This behaviour seems to reverse as we move deeper in the tail region. On the contrary, the D1V diode under-responds ($k^{f_{clin}(d),f_{clin}(0)}_{Q_{clin}(d),Q_{clin}(0)} > 1$) up to about 13% in the tail region. This trend seems to increase as we move deeper in the tail region.

The detector behaviour can be better understood by looking at the relative perturbation factors. On the on-axis perturbations, $P^{f_{clin},f_{msr}}_{Q_{clin},Q_{msr}}$, the detectors that had a relative large radius, such as the microLion (r=1.25 mm) and microDiamond (r=1.1 mm), exhibited an increased volume averaging effect. This effect was partially compensated by the high density materials that surround the active volume, such as the graphite electrode and diamond substrate in the previous cases. Thus, the total $k^{f_{clin},f_{msr}}_{Q_{clin},Q_{msr}}$ corrections presented are eventually smaller. The unshielded diode also exhibits an over-response due to the high density materials surrounding the active volume (silicon and wall). However, the effect here is not compensated by the volume perturbation since the diode's radius is small (r=0.5 mm). For the scintillator W1 negligible perturbations are presented if it is oriented parallel to the CAX. The larger correction observed for the perpendicular orientation can almost exclusively be attributed to the increased volume averaging due to the relative long active volume under this orientation (3 mm). It is interesting to note that the active volume material does not perturb the output factor more than 1% in any case. This verifies the fact that the stopping power ratios do not change significantly as a function of field size.

On the off-axis perturbations, $P^{f_{clin(d)},f_{clin(0)}}_{Q_{clin(d)},Q_{clin(0)}}$, the high density materials, such as the graphite electrode (microLion), silicon (D1V) and diamond (microDiamond) cause an under-estimation of the dose relative to the CAX ($P^{f_{clin(d)},f_{clin(0)}}_{Q_{clin(d)},Q_{clin(0)}} > 1$). This effect is dominant to the diode D1V. The volume averaging effect presents an over-response in the regions of steep gradient changes out of the field ($P^{f_{clin(d)},f_{clin(0)}}_{Q_{clin(d)},Q_{clin(0)}} < 1$). The effect is reduced as the gradient becomes smaller in the deeper tail region. This effect is dominant to the microLion and microDiamond designs. The scintillator W1 exhibits a small perturbation due to volume averaging.

The OF_{det} over-response of high density materials can be explained if we consider that the $P^{f_{clin},f_{msr}}_{Q_{clin},Q_{msr}}$ is a relative perturbation of a smaller field (f_{clin}) to a larger field (f_{msr}). For example, in the case of the microDiamond, removing the diamond substrate results in a perturbation of $P^{0.5\times0.5}_{\mathrm{diam}} = 0.97$ for the 0.5×0.5 cm^2. This is expected since the diamond substrate increases the electron fluence towards the active volume. Repeating the calculation for the msr field (10×10 cm^2) results in a smaller perturbation ($P^{10\times10}_{\mathrm{diam}} = 0.99$). This could be due to the lateral shielding of the active volume by the diamond substrate. In the case of the large fields, a significant contribution of the dose originates from photons scattering in the phantom and eventually creating charged particles around the active volume. If the active volume is surrounded laterally by a high density material, then it is partially shielded by these secondary charged particles. Thus, the relative perturbation $P^{f_{\mathrm{clin}},f_{\mathrm{msr}}}_{Q_{\mathrm{clin}},Q_{\mathrm{msr}}} = P^{0.5\times0.5}_{\mathrm{diam}}/P^{10\times10}_{\mathrm{diam}}$ will be smaller than 1. A similar argument can be posed for the profile perturbations $P^{f_{\mathrm{clin(d)}},f_{\mathrm{clin(0)}}}_{Q_{\mathrm{clin(d)}},Q_{\mathrm{clin(0)}}}$. In this case, the off-axis positions are mainly affected by the shielding of the active volume. Thus, the detector under-responds off-axis and leads to a relative perturbation $P^{f_{\mathrm{clin(d)}},f_{\mathrm{clin(0)}}}_{Q_{\mathrm{clin(d)}},Q_{\mathrm{clin(0)}}} > 1$. Further studies, including a phase-space analysis of the particles depositing dose in the cavity, could potentially provide us a better understanding of these effects.

By changing the active volume radius and thus the volume averaging effect, we can achieve a complete compensation of the high density material perturbation. This is an equivalent, but perhaps simpler, approach of designing correction-free detectors compared to changing the surrounding mass of the cavity as suggested previously by Charles et al., 2013 and Underwood et al., 2013. In the case of the microLion this was achieved by reducing the radius, while in the case of the diode by increasing it. As it can be seen in figure 4.8, the smallest $k^{f_{\mathrm{clin}},f_{\mathrm{msr}}}_{Q_{\mathrm{clin}},Q_{\mathrm{msr}}}$ corrections are observed for a radius of 1 mm in both cases. A radius of 0.85 mm for the microLion would still provide

$k^{f_{clin},f_{msr}}_{Q_{clin},Q_{msr}}$ within 1 % compared to water. On the profiles (figure 4.9) the microLion presents $k^{f_{clin}(d),f_{clin}(0)}_{Q_{clin}(d),Q_{clin}(0)}$ corrections less than 5 % compared to water for a radius of 0.75 or 0.85 mm. For the diode, a 1 mm radius is again optimal.

4.5 Conclusions

The commissioning of small fields should include small field profiles and output factors in order the source size to be properly estimated. Large fields, even including a 2 × 2 cm^2 field, are not adequate for that purpose. Furthermore, the detector's response should be explicitly modeled in the dose calculation part including all high density materials surrounding it. Robust direct source reconstruction methods are still needed to be developed. Such a development would substantially reduce the time and input data required during commissioning.

For the modern dosimeters investigated in this work the smallest corrections were observed primarily for the scintillator W1 and secondly for the microDiamond. These results should also be verified by experiments, especially in the case of the scintillator where the Cherenkov emission within the optical fiber may distort the measurement. A method has been suggested recently for correcting this effect in plastic scintillators (Morin 2013). The accuracy of this method on the W1 scintillator in small fields is yet to be evaluated.

The most significant perturbations were due to the finite size of the active volume and the presence of high density materials surrounding the cavity. Since these perturbations cause opposite effects, detectors can be optimally designed so that they present minimal corrections in both OF_{det} and profiles. For the case of the microLion this could be achieved by reducing the radius to 0.85 mm, while for the case of the diode D1V by increasing the radius to 1 mm.

Further work is still needed in designing detectors which would present minimal corrections both on CAX and off-axis. The importance of out-of-field dosimetry should not be neglected, as the absolute doses delivered in these regions are still high during hypo-fractionated SRS treatments. Furthermore, these doses will mainly affect organs at risk and healthy tissues.

Acknowledgments

The authors would like to acknowledge Compute Canada/Calcul Quebec for providing computing resources as well as Dr. Stephane Bedwani and Daniel Stubbs for technical assistance. PP gratefully acknowledges the financial support by the Alexander S. Onassis Public Benefit Foundation in Greece and by the CREATE Medical Physics Research Training Network grant of the Natural Sciences and Engineering Research Council (Grant number: 432290).

Chapter 5

Experimental investigation on the accuracy and precision of plastic scintillation dosimeters and on the spectral discrimination calibration method in small photon fields

Pavlos Papaconstadopoulos, Louis Archambault and Jan Seuntjens This study follows previous work on Monte Carlo calculated detector-specific correction factors (chapter 4). Based on the findings in that work, plastic scintillation dosimeters are the closest to "correction-free" dosimeters currently available in the clinic, if the Cherenkov problem is adequately addressed. In this work a commercial scintillation dosimeter is investigated experimentally and compared to liquid ionization chamber, unshielded diode and synthetic diamond detector output factor measurements after the appropriate correction factors are applied. The commercial scintillator is also directly compared to a similar prototype system in small photon fields. The effect of fiber orientation and wavelength threshold choice of the spectrum calibration method is examined and related to the output factor measurements.

Abstract The purpose of this study is to investigate the accuracy and precision of plastic scintillation dosimeters (PSD) and especially the commercial Exradin W1 (SI) in small photon fields. Repetitive output factor $\mathrm{OF_{det}}$ measurements were performed in water (parallel CAX) using two W1 PSDs (SI), a PTW microLion, a PTW microDiamond and an unshielded diode D1V (SI) and appropriate corrections factors were applied. Four sets of repetitive measurements were also performed with the W1 PSD positioned parallel and perpendicular to the CAX, each set on a different week, and analytically calculated volume averaging corrections were applied. The W1 $\mathrm{OF_{det}}$ measurements were also directly compared to measurements using an "in-house" developed PSD in water (CHUQ). The performance of the spectrum discrimination calibration procedure was evaluated under the different fiber orientations and wavelength threshold choices and the impact on the respective $\mathrm{OF_{det}}$ was reported. For all detectors in the study an excellent agreement was observed down to a field size of 1 × 1 cm^2. For the smallest field size of 0.5 × 0.5 cm^2 the W1 PSDs presented a $\mathrm{OF_{det}}$ higher by +3.8 to 5.0 % relative to the mean corrected $\mathrm{OF_{det}}$ of the rest of the detectors and by +5.8 % relative to the CHUQ PSD. The repetitive W1 $\mathrm{OF_{det}}$ measurements in water (parallel CAX) were higher by +3.9 % relative to the $\mathrm{OF_{det}}$ measurement in $\mathrm{Solid\,Water^{TM}}$(perpendicular CAX) after volume averaging corrections were applied. The spectrum discrimination method provided reproducible Cherenkov spectra under

the different calibration set-ups with a small systematic shift towards higher wavelengths when the calibration is performed in water (parallel CAX). The impact of fiber orientation and wavelength threshold on $\mathrm{OF_{det}}$ was in general minimal. Further research is needed to determine the origin of the observed differences between the different PSD systems.

5.1 Introduction

Accurate dosimetry in small radiation fields has been a challenging problem and an active area of research for medical physicists. Non-water material components in a detector are expected to significantly significantly the output factor measurements, while the finite detector volume may result in an under-response due to volume averaging (Laub and Wong, 2003).

In 2008, Alfonso et al., 2008 presented a new formalism for small fields. According to the formalism, a detector-specific correction factor $\mathrm{k^{f_{clin},f_{msr}}_{Q_{clin},Q_{msr}}}$ can be applied on the detector-specific output factor measurements, $\mathrm{OF_{det}} = \frac{\mathrm{M^{f_{clin}}_{Q_{clin}}}}{\mathrm{M^{f_{msr}}_{Q_{msr}}}}$, to derive the field factors, $\Omega^{\mathrm{f_{clin},f_{msr}}}_{\mathrm{Q_{clin},Q_{msr}}} = \frac{\mathrm{D^{f_{clin}}_{w,Q_{clin}}}}{\mathrm{D^{f_{msr}}_{w,Q_{msr}}}}$:

$$\Omega^{\mathrm{f_{clin},f_{msr}}}_{\mathrm{Q_{clin},Q_{msr}}} = \frac{\mathrm{D^{f_{clin}}_{w,Q_{clin}}}}{\mathrm{D^{f_{msr}}_{w,Q_{msr}}}} = \frac{\mathrm{M^{f_{clin}}_{Q_{clin}}}}{\mathrm{M^{f_{msr}}_{Q_{msr}}}} \cdot \mathrm{k^{f_{clin},f_{msr}}_{Q_{clin},Q_{msr}}}, \tag{5.1}$$

,where $\mathrm{D^{f_{clin}}_{w,Q_{clin}}}$ and $\mathrm{M^{f_{clin}}_{Q_{clin}}}$ are the calculated dose in a small volume of water and the detector reading in a clinical field ($\mathrm{f_{clin}}$) and $\mathrm{D^{f_{msr}}_{w,Q_{msr}}}$ and $\mathrm{M^{f_{msr}}_{Q_{msr}}}$ are the respective dose and detector reading in a machine-specific reference field ($\mathrm{f_{msr}}$).

The $\mathrm{k^{f_{clin},f_{msr}}_{Q_{clin},Q_{msr}}}$ factors can be accurately derived by an explicit Monte Carlo (MC) simulation of the linear accelerator and the detector of interest. However, such an approach is time-consuming and requires MC expertise. An alternative approach would be the development of a real-time, non-perturbing dosimeter which would require no correction ($k^{f_{clin},f_{msr}}_{Q_{clin},Q_{msr}} \simeq 1$). Plastic scintillation dosimeters (PSD) are good candidates for fulfilling this role, since their radiation absorption characteristics are similar to water (Archambault et al., 2007; Beddar, Mackie, and Attix, 1992a; Beddar, Mackie, and Attix, 1992b). Furthermore, PSDs can be manufactured in small volumes, thus minimizing the volume averaging effect. Previous researchers have shown, using prototype systems, that PSDs can be used as reference detectors in small fields (Morin et al., 2013; Ralston et al., 2012). Recently, the first commercial PSD was introduced for clinical use (Exradin W1, Standard Imaging). MC studies have shown that the geometrical and material properties of the W1 are such that a negligible correction relative to dose in water is required (Francescon, Kilby, and Satariano, 2014; Papaconstadopoulos, Tessier, and Seuntjens, 2014; Kamio and Bouchard, 2014).

PSDs are composed by a scintillating volume, an optical fiber and a photodetector. As charged particles deposit energy in the scintillating volume, visible light is emitted. The light is then propagated via total reflection in an optical fiber and collected in a a photo-detector system, which could be a photodiode (PD) or a photomultiplier tube (PMT). However, charged particles traveling with velocities higher than the speed of light in the medium will also cause Cherenkov photons to be emitted mainly in the visible and ultraviolet region. This effect is expected to occur in plastic-based materials for electron energies above 145-180 keV (Beaulieu et al., 2013). Therefore, the Cherenkov signal produced in the optical fiber and scintillating volume will contaminate the scintillation signal and perturb the measurements. To date, several researchers have suggested and evaluated numerous solutions to the Cherenkov problem (Beddar, Mackie, and Attix, 1992a; Beddar, Mackie, and Attix, 1992b; Clift, Johnston, and Webb, 2002; De Boer, Beddar, and Rawlinson, 1993; Fontbonne et al., 2002; Lambert et al., 2008). One of the most practical methods for correcting the Cherenkov signal is the spectral discrimination technique (Fontbonne et al., 2002; Frelin et al., 2005; Guillot et al., 2011).

According to the spectral discrimination method, the $\mathrm{OF}_{\mathrm{det}}$ can be derived by the following expressions:

$$\mathrm{OF}_{\mathrm{det}} = \frac{\mathrm{M}_{\mathrm{Q_{clin}}}^{\mathrm{f_{clin}}}}{\mathrm{M}_{\mathrm{Q_{msr}}}^{\mathrm{f_{msr}}}} = \frac{\mathrm{B}_{\mathrm{Q_{clin}}}^{\mathrm{f_{clin}}} - \mathrm{CLR} \cdot \mathrm{G}_{\mathrm{Qclin}}^{\mathrm{fclin}}}{\mathrm{B}_{\mathrm{Q_{msr}}}^{\mathrm{f_{msr}}} - \mathrm{CLR} \cdot \mathrm{G}_{\mathrm{Qmsr}}^{\mathrm{fmsr}}}, \tag{5.2}$$

with

$$\mathrm{CLR} = \frac{\mathrm{B_C}}{\mathrm{G_C}}, \tag{5.3}$$

where $\mathrm{B}_{\mathrm{Q_{clin}}}^{\mathrm{f_{clin}}}$: signal of the blue channel in the fclin field, $\mathrm{G}_{\mathrm{Qclin}}^{\mathrm{fclin}}$: signal of the green channel in the fclin field, $\mathrm{B}_{\mathrm{Q_{msr}}}^{\mathrm{f_{msr}}}$: signal of the blue channel in the fmsr field and $\mathrm{G}_{\mathrm{Qmsr}}^{\mathrm{fmsr}}$: signal of the green channel in the fmsr field, $\mathrm{B_C}$: Cherenkov signal in the blue channel and $\mathrm{G_C}$: Cherenkov signal in the green channel. The blue and green signals are extracted from the scintillation spectrum by choosing a wavelength threshold, often considered to be about 500 nm (figure 5.1). However, it should be emphasized that the principles of the spectral discrimination method can be applied using any combination of two different wavebands, regardless if the wavebands refer to the actual blue and green spectral region.

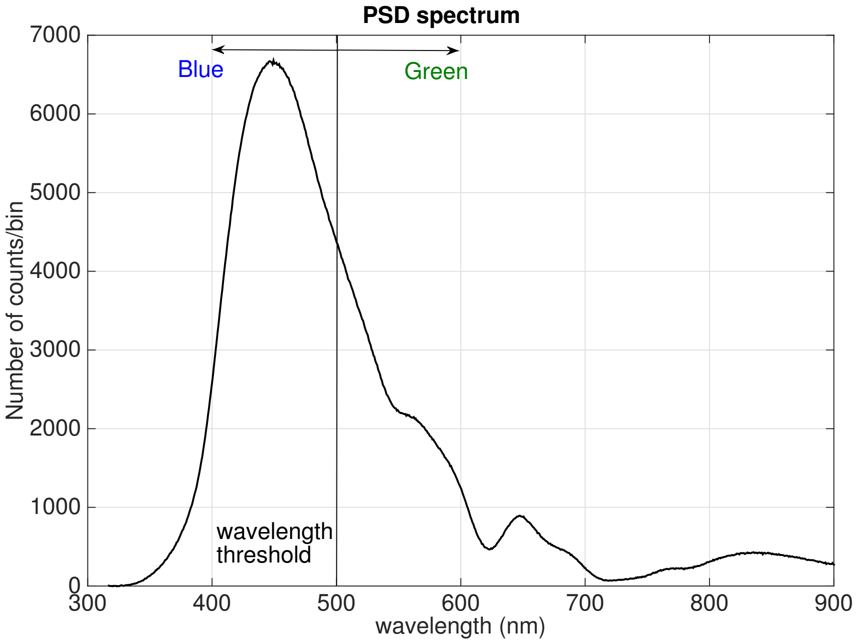

FIGURE 5.1: An example of the photon spectrum collected in a photodetector. The blue and green channels are separated by a wavelength threshold around 500 nm.

The Cherenkov Light Ratio (CLR) is defined as the ratio of the Cherenkov signal emitted in the blue channel, B_C, to the Cherenkov signal emitted in the green channel, G_C. The CLR serves as a correction on the relative difference of the Cherenkov fluence observed in the blue region to the green region. The CLR can be derived by performing first a measurement in a field with a large portion (max) of the fiber irradiated (figure 5.2a). The measurement is then repeated, keeping the scintillator in the same position and in the same field, but with less fiber (min) irradiated (figure 5.2b). Since the dose delivered to the scintillator in both cases is the same, any differences observed can be attributed only to the Cherenkov signal. The CLR can then be derived by eq. 5.4:

$$\mathrm{CLR} = \frac{\mathrm{B_C}}{\mathrm{G_C}} = \frac{\mathrm{B_{max}} - \mathrm{B_{min}}}{\mathrm{G_{max}} - \mathrm{G_{min}}} \tag{5.4}$$

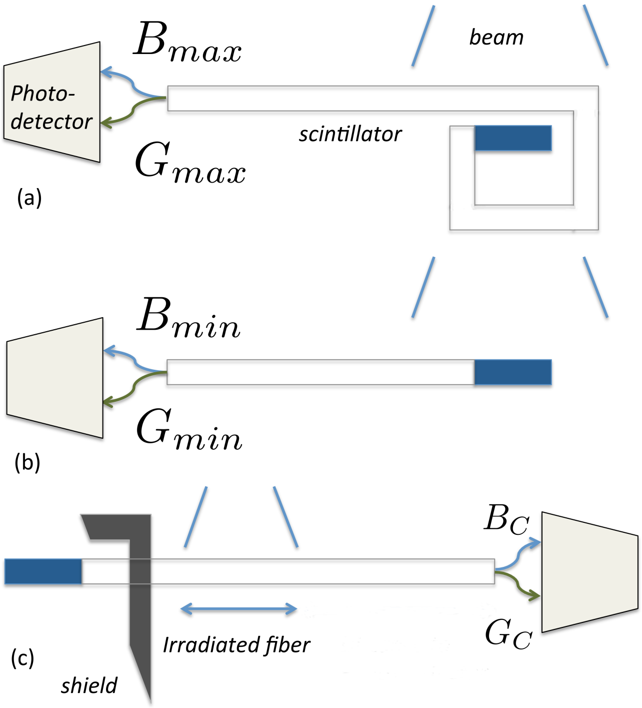

FIGURE 5.2: Graphical representation of the calibration set-up configuration with max fiber (a) and min fiber (b) irradiated. In both cases the dose to the scintillator is the same. A direct measurement of the pure Cherenkov signal can be performed by irradiating only the fiber, while the scintillator is shielded (c).

An alternative approach for deriving the CLR is by a shielded measurement (figure 5.1c). In such a case, the scintillator is placed out of the field and completely shielded from radiation. A portion of the plastic fiber is directly irradiated producing pure Cherenkov signal, assuming negligible absorbed dose in the scintillator. The CLR can then be directly calculated by eq. 5.3.

A requirement of the spectral discrimination method is that the CLR value should not vary with field size, irradiated fiber length or orientation. Possible changes in the shape of the Cherenkov spectrum reaching the photodetector, under different irradiation conditions, may result in a change of the CLR value and consequently affect the dosimetric accuracy. Furthermore, since the distance to the photodiode changes depending on where the Cherenkov signal is produced, attenuation in the fiber should have a similar impact on the $\mathrm{B_C}$ and $\mathrm{G_C}$ signals. An inappropriate choice of the fiber material and technical specifications may result in variations of the CLR and compromise the accuracy of the system (Guillot et al., 2011).

The purpose of this work was primarily to investigate the accuracy and precision of the commercial Exradin W1 system in measuring field factors $\Omega^{\mathrm{f_{clin},f_{msr}}}_{\mathrm{Q_{clin},Q_{msr}}}$ in small field sizes of 0.5×0.5, 1×1 and 2×2 cm^2. The W1 $\mathrm{OF_{det}}$ were compared to the expected field factors $\Omega^{\mathrm{f_{clin},f_{msr}}}_{\mathrm{Q_{clin},Q_{msr}}}$ derived using liquid ion chamber, diode and a synthetic diamond $\mathrm{OF_{det}}$ after MC calculated $\mathrm{k}^{\mathrm{f_{clin},f_{msr}}}_{\mathrm{Q_{clin},Q_{msr}}}$ factors were applied (Papaconstadopoulos, Tessier, and Seuntjens, 2014). The W1 $\mathrm{OF_{det}}$ were also directly compared to measurements performed with a similar "in-house" developed PSD, manufactured at the Centre hospitalier universitaire de Québec (CHUQ). In addition potential dependencies of the spectrum calibration method and of the extracted Cherenkov spectra on the PSD orientation and wavelength threshold choice are investigated and their impact on the $\mathrm{OF_{det}}$ is reported.

5.2 Methods

5.2.1 The W1 PSD system

The W1 scintillating volume is composed of polystyrene and has a cylindrical shape of diameter of 1 mm and length of 3 mm. The scintillating light is transferred via a 3 m long optical fiber composed by PMMA to a photodiode (PD). The PD is shielded with brass and should be placed at least 1 m away from the beam to reduce signal contamination from scattered radiation. The PD produces a signal proportional to the number of photon counts received in each spectral region (blue and green). The signals should are read simultaneously from both channels.

5.2.2 The CHUQ PSD system

The CHUQ PSD scintillating volume has similar geometrical (diameter = 1 mm, length = 3 mm) and material composition (polystyrene) characteristics as the W1. The optical fiber length is 15 m and and is composed by EKSA Premier PMMA (Mitsubishi Rayon Co., Ltd., Tokyo, Japan). The signal is collected by an Ocean Optics QE65 Pro spectrometer with a wavelength acceptance range of 185 - 1100 nm. Therefore, the full spectrum can be analyzed with the CHUQ PSD system. The spectrometer is placed outside the treatment room to avoid contribution from scattered radiation. A wavelength threshold is chosen to separate the blue to the green channels, usually set at about 500 nm.

5.2.3 Cherenkov calibration procedure

Calibration measurements with the W1 and CHUQ PSDs can be performed in $\mathrm{Solid\ Water}^{\mathrm{TM}}$ (GAMMEX, Middleton, WI) or in water. In the former case, the PSD is firmly placed within the calibration slab provided by the manufacturer (SI). In such configuration the detector lies perpendicular to the beam central axis (⊥ CAX) and has a resolution of 3 mm. For this resolution a volume averaging effect is expected to occur for the 0.5×0.5 cm^2 field size (Papaconstadopoulos, Tessier, and Seuntjens, 2014). The Cherenkov calibration procedure consists of a measurement in the max fiber set-up (fig. 5.2a) where 65 cm of optical fiber are rolled around the scintillating volume and a measurement in the min fiber set-up (fig. 5.2b) where 15-20 cm of fiber are irradiated. A large field size (30×30 or 40×40 cm^2) can be used for these measurements. For the calibration in water, the PSD is placed parallel to the beam central axis ($\parallel$ CAX). In this orientation the detector's resolution is 1 mm, which results in a small volume averaging correction even for the smallest field size. The Cherenkov calibration is performed by placing at least 30 cm of fiber in the beam for the max fiber set-up and 10 cm of fiber for the min fiber set-up. It should be noted that the total irradiated fiber length is more restricted for the parallel orientation than for the perpendicular orientation. For the former case a rigid glass rod was utilized to provide support to the fiber and ensure that exactly 30 cm of fiber were irradiated. This procedure increased the reproducibility of the CLR measurements. A large field size of 10×10 cm^2 can be used for these measurements. The CLR values can be calculated in both cases by eq. 5.4.

For the shielded calibration (fig. 5.2c), the scintillating volume is completely shielded using lead blocks and placed at a distance of 2 m away from the beam's CAX. A background measurement is first performed with the full length of the fiber behind the shield, to ensure that there is no scattered radiation reaching the scintillating volume. Then, a section of the optical fiber of a length of 20 cm is irradiated in Solid Water™. In this case the CLR can be calculated directly by equation (3). All calibration measurements were performed at a depth of 5 cm and at a source to surface distance (SSD) of 100 cm.

5.2.4 $\mathrm{OF_{det}}$ measurements

$\mathrm{OF_{det}}$ water tank measurements were performed for the $\mathrm{f_{clin}}$ fields of 0.5×0.5, 1×1 and 2×2 cm^2 using two W1 PSD system (SN: 32385 and 30452), the PTW microLion, the Exradin diode D1V (SI) and the PTW microDiamond. The $\mathrm{f_{msr}}$ field was 10×10 cm^2. For the PTW microLion the operating voltage was set to +800 V to reduce ion recombination effects. Dose rate dependence effects were corrected as suggested by Chung, Davis, and Seuntjens, 2013. The measurements were performed within the same day using a Varian Novalis Tx linear accelerator in stereotactic mode (6 MV). The SSD was set to 100 cm. The measurements were repeated in total four times with the secondary collimator/jaws re-positioned prior to each measurement. The detectors were first aligned to the center of radiation field using the linac laser alignment system and then by iteratively moving the detector on the cross-plane and in-plane orientations until the point of maximum signal was found. The geometrical center of the sensitive volume was positioned at a depth of 5 cm. Detector-specific correction factors $\mathrm{k^{f_{clin},f_{msr}}_{Q_{clin},Q_{msr}}}$ were applied on each detector system, as suggested by the Alfonso protocol (Alfonso et al., 2008). Ideally the corrected $\mathrm{OF_{det}}$ should converge to the same field factor $\Omega^{\mathrm{f_{clin},f_{msr}}}_{\mathrm{Q_{clin},Q_{msr}}}$ as shown by previous researchers (Francescon et al., 2012; Pantelis et al., 2012). The $\mathrm{k^{f_{clin},f_{msr}}_{Q_{clin},Q_{msr}}}$ factors were adopted from previous work using MC simulations under the same experimental conditions (Papaconstadopoulos, Tessier, and Seuntjens, 2014).

In order to include the effects of detector positioning, jaw positioning and possible accelerator or detector output variations as a function of time in the uncertainty analysis, four sets of $\mathrm{OF_{det}}$ measurements were repeated in different weeks with the

W1 system in the $\mathrm{Solid\,Water^{TM}}$ ($\perp$ CAX) and in the water ($\parallel$ CAX) set-up configurations. For the $\mathrm{Solid\,Water^{TM}}$ measurements ($\perp$ CAX), the W1 was positioned on the crossplane orientation. In order to include possible CLR variations in the total uncertainty, the spectrum discrimination calibration procedure was repeated for each set-up configuration prior to each set of measurement. The total uncertainty was calculated as the standard deviation of the mean of all measurements. Since for the PSDs only a volume averaging effect should be expected, volume averaging correction factors $\mathrm{P_{vol}}$, were calculated analytically for the parallel and perpendicular orientations and applied directly on the $\mathrm{OF_{det}}$ (section 5.2.5). Assuming that the PSD response is independent of the orientation of the fiber during the measurements, the $\mathrm{OF_{det}}$ in the parallel and perpendicular orientation are expected to converge to the same factors after the $\mathrm{P_{vol}}$ corrections are applied.

5.2.5 Volume averaging corrections

The volume averaging corrections were calculated analytically based on four sets of diode D1V crossplane and inplane profile measurements (Papaconstadopoulos, Tessier, and Seuntjens, 2014). A 2D biquadratic polynomial function (4th order but without odd terms) was fitted on each measured profile set using a Trust-Region reflective least-squares algorithm. The fitting was performed in the local relative dose region from -2 mm to + 2 mm in the crossplane and inplane orientations. The volume averaging correction for the perpendicular orientation to the CAX, $\mathrm{P^{\perp}_{vol}}$, was calculated as:

$$P_{\mathrm{vol}}^{\perp} = \frac{\int_{x_{\min}}^{x_{\max}} \int_{y_{\min}}^{y_{\max}} w(x,y) D_{\mathrm{rel,fit}}(x,y) dxdy}{\int_{x_{\min}}^{x_{\max}} \int_{y_{\min}}^{y_{\max}} w(x,y) dxdy} \tag{5.5}$$

,where min and max define the limits of the detector's sensitive volume in the crossplane and inplane orientation and w(x,y) are the relative weights. The relative weights were calculated as $w(x,y) = \sqrt{1-(\frac{y}{r})^2}$ to account for the change in the curvature in the inplane orientation (y) when the detector is positioned in the crossplane orientation (x). The volume averaging for the parallel orientation to the CAX, $P_{\mathrm{vol}}^{\parallel}$, was calculated in cylindrical coordinates, similarly to the work by Morin et al., 2013:

$$P_{\mathrm{vol}}^{\parallel} = \frac{\int_{0}^{r} \int_{0}^{2\pi} D_{\mathrm{rel,fit}}(r,\theta) r dr d\theta}{\pi r^2} \tag{5.6}$$

,where r is the radius of the sensitive volume. In both cases, the volume averaging correction and 1 σ uncertainty level was estimated as the mean and standard deviation respectively of the calculated P_{vol} values calculated for each diode profile used.

5.2.6 CHUQ PSD spectra and $\mathrm{OF}_{\mathrm{det}}$ measurements

A set of $\mathrm{OF}_{\mathrm{det}}$ measurements was performed using the CHUQ PSD under the same conditions described previously for the W1. In this case, the light spectrum was measured for each field size. In total five repetitions of the spectral measurements were performed. Background readings were performed periodically and subtracted from the respective measurements. The blue and green channels were separated by setting a wavelength threshold in the region between 450 and 550 nm. The total number of counts below the threshold were considered to compose the blue channel, while the total number of counts above the threshold were assigned to the green channel. The $\mathrm{OF_{det}}$ can then be calculated by equation 5.2. In order to evaluate the impact of the threshold choice on the $\mathrm{OF_{det}}$, the wavelength threshold value varied from 450 to 550 nm with a step of 1 nm and the $\mathrm{OF_{det}}$ were re-calculated each time and compared to each other. The spectral discrimination calibration method was performed in water (fig. 5.2a), in $\mathrm{Solid\,Water^{TM}}$(fig. 5.2b) and using the shielded method (fig. 5.2c). In order to evaluate the impact of the CLR calibration procedure on the $\mathrm{OF_{det}}$ measurements, the $\mathrm{OF_{det}}$ were recalculated using the CLR values derived by each calibration method. The spectral calibration method was repeated in total 5 times in order to include the CLR variations in the uncertainty analysis. $\mathrm{OF_{det}}$ using the W1 PSD system were also performed during the same day with the CHUQ PSD in order to reduce possible systematic uncertainties. For the W1 PSD the calibration was performed in water (∥ CAX) and in $\mathrm{Solid\,Water^{TM}}$ (⊥ CAX) and the $\mathrm{OF_{det}}$ recalculated for each calibration set-up.

5.3 Results and Discussion

Table 5.1 and fig. 5.3 present the $\mathrm{OF_{det}}$ measurements performed with all detectors during the same day before and after applying the respective $\mathrm{k^{f_{clin},f_{msr}}_{Q_{clin},Q_{msr}}}$ factors. In order to evaluate the accuracy of the MC model, the respective MC calculated $\mathrm{OF^{MC}_{det}}$ for each detector system and the dose in a small volume of water (diameter=0.3 mm, length=0.3 mm) are also presented in table 5.1. It can be observed that for the smallest field size of 0.5 × 0.5 $\mathrm{cm^2}$, the corrected readings for the microLion, microDiamond and diode D1V

TABLE 5.1: Detector output factor measurements and Monte Carlo calculations for the microLion, diode D1V, microDiamond and two W1 scintillators (SN:32385 and 30452). The corrected measurements are also presented after applying the $k^{f_{clin},f_{msr}}_{Q_{clin},Q_{msr}}$ factors. All uncertainties in the parenthesis refer to the 1 standard deviation level.

Detectors	Output factors	0.5×0.5 cm^2	1×1 cm^2	2×2 cm^2
microLion	$\mathrm{OF}_{\mathrm{det}}$	0.561 (0.007)	0.785 (0.001)	0.870 (0.001)
	$\mathrm{OF}^{\mathrm{MC}}_{\mathrm{det}}$	0.565 (0.002)	0.786 (0.002)	0.871 (0.002)
	$\mathrm{OF}_{\mathrm{det}} k^{f_{clin},f_{msr}}_{Q_{clin},Q_{msr}}$	0.573 (0.008)	0.778 (0.003)	0.868 (0.005)
diode D1V	$\mathrm{OF}_{\mathrm{det}}$	0.594 (0.003)	0.773 (0.002)	0.850 (0.001)
	$\mathrm{OF}^{\mathrm{MC}}_{\mathrm{det}}$	0.592 (0.001)	0.782 (0.002)	0.864 (0.002)
	$\mathrm{OF}_{\mathrm{det}} k^{f_{clin},f_{msr}}_{Q_{clin},Q_{msr}}$	0.580 (0.004)	0.772 (0.004)	0.858 (0.003)
microDiamond	$\mathrm{OF}_{\mathrm{det}}$	0.579 (0.005)	0.783 (0.002)	0.862 (0.001)
	$\mathrm{OF}^{\mathrm{MC}}_{\mathrm{det}}$	0.570 (0.002)	0.788 (0.002)	0.874 (0.003)
	$\mathrm{OF}_{\mathrm{det}} k^{f_{clin},f_{msr}}_{Q_{clin},Q_{msr}}$	0.587 (0.006)	0.776 (0.004)	0.860 (0.004)
W1/32385	$\mathrm{OF}^{32385}_{\mathrm{det}}$	0.602 (0.006)	0.782 (0.001)	0.862 (0.004)
W1/30452	$\mathrm{OF}^{30452}_{\mathrm{det}}$	0.609 (0.002)	0.782 (0.007)	0.865 (0.007)
	$\mathrm{OF}^{\mathrm{MC}}_{\mathrm{det}}$	0.576 (0.001)	0.782 (0.002)	0.871 (0.003)
	$\mathrm{OF}^{32385}_{\mathrm{det}} k^{f_{clin},f_{msr}}_{Q_{clin},Q_{msr}}$	0.606 (0.007)	0.782 (0.003)	0.861 (0.005)
	$\mathrm{OF}^{30452}_{\mathrm{det}} k^{f_{clin},f_{msr}}_{Q_{clin},Q_{msr}}$	0.613 (0.003)	0.782 (0.008)	0.864 (0.008)
dose in water	$\mathrm{OF}^{\mathrm{MC}}_{\mathrm{H_20}}$	0.577 (0.002)	0.781 (0.002)	0.873 (0.003)

agree to within the experimental uncertainties with a mean $\overline{\mathrm{OF}_{\mathrm{det}}}$=0.580 and standard deviation (1 σ) of 1.2 %. The mean $\overline{\mathrm{OF}_{\mathrm{det}}}$ presented an excellent agreement, within 0.5 %, with the $\mathrm{OF}^{\mathrm{MC}}_{\mathrm{water}}$ calculation in water using the previously commissioned MC beam model. The W1 PSDs exhibited a $\mathrm{OF}_{\mathrm{det}}$ higher by +3.8 % (SN:32385) and +5.0 % (SN:30452) (before correction) and by +4.5 % (SN: 32385) and +5.7 % (SN: 30452) (after correction) relative to the mean $\overline{\mathrm{OF}_{\mathrm{det}}}$ of the rest of the detectors. A similar discrepancy is observed relative to the expected MC-calculated W1 $\mathrm{OF}^{\mathrm{MC}}_{\mathrm{det}}$ (+4.5 % and +5.7 %) and relative to the dose in a small voxel in water (+4.3 % and +5.6 %). As can be seen in fig. 5.3, the W1 $\mathrm{OF}_{\mathrm{det}}$ readings do not agree within the 1 σ experimental uncertainty after $k^{f_{clin},f_{msr}}_{Q_{clin},Q_{msr}}$ correction factors have been applied. For the field sizes of 1×1 cm^2 and 2×2 cm^2 an excellent agreement is observed between all detectors with a maximum

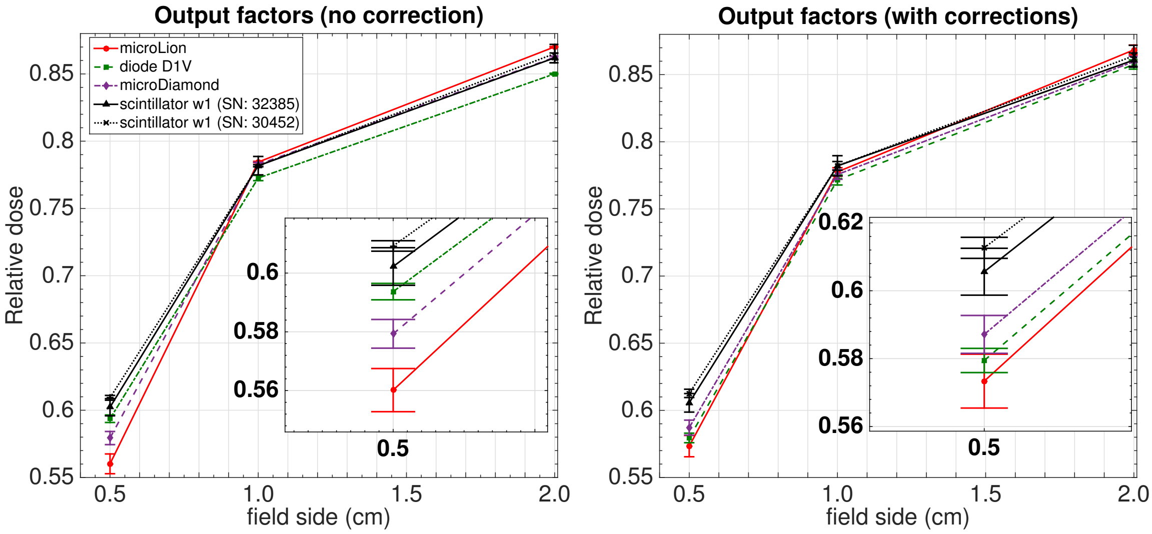

FIGURE 5.3: Detector output factor measurements for the microLion, diode D1V, microDiamond and two W1 scintillators (SN:32385 and 32385), before and after $k_{Q_{clin},Q_{msr}}^{f_{clin},f_{msr}}$ correction factor have been applied.

deviation better than 1.5 % and 1.3 % before and after corrections respectively.

Table 5.2 exhibits the mean W1 OF_{det} of the four sets of measurements performed in different weeks along with the total experimental uncertainties (1 σ). In this case the measurements were performed both in water tank (∥ CAX) and in the Solid Water™ slab (⊥ CAX) before and after applying volume averaging corrections (P_{vol}). The P_{vol} corrections, calculated using eq. 5.5 and 5.6, are presented in table 5.3 for both orientations. As expected the ∥ CAX orientation (resolution=1 mm) presents a minimal volume averaging correction of +0.9 %, while the ⊥ CAX orientation (resolution=3 mm) presents a much more significant correction of +6.3 % for the 0.5 × 0.5 cm^2 field size. Applying the P_{vol} corrections on the W1 OF_{det} revealed a relative discrepancy between the two orientations of 3.9 % for the smallest field size. Applying the MC-calculated $k_{Q_{clin},Q_{msr}}^{f_{clin},f_{msr}}$ factors on the W1 OF_{det} revealed a relative difference between the two orientations of 5.3 % for the smallest field sizes. In both cases the corrected W1 measurements on the ⊥ CAX orientation appeared to agree well (within 0.7 - 1.2

TABLE 5.2: Mean W1 output factor measurements in water (∥ CAX) and in Solid Water$^{\mathrm{TM}}$(⊥ CAX). The measurements were repeated in total four times, each set performed in a different week. The total experimental uncertainties include the effects of detector and jaw re-positioning as well as time evolution changes of the accelerator-detector system.

Orientation	Output factors	0.5×0.5 cm^2	1×1 cm^2	2×2 cm^2
∥ CAX	$\mathrm{OF_{det}}$	0.602 (0.005)	0.780 (0.008)	0.860 (0.008)
	$\mathrm{OF_{det}^{MC}}$	0.576 (0.001)	0.782 (0.002)	0.871 (0.003)
	$\mathrm{OF_{det}P_{vol}}$	0.607 (0.005)	0.780 (0.008)	0.860 (0.008)
	$\mathrm{OF_{det}k_{Q_{clin},Q_{msr}}^{f_{clin},f_{msr}}}$	0.605 (0.005)	0.780 (0.008)	0.859 (0.009)
⊥ CAX	$\mathrm{OF_{det}}$	0.549 (0.005)	0.780 (0.002)	0.869 (0.003)
	$\mathrm{OF_{det}^{MC}}$	0.553 (0.001)	0.784 (0.002)	0.875 (0.002)
	$\mathrm{OF_{det}P_{vol}}$	0.584 (0.006)	0.783 (0.003)	0.869 (0.003)
	$\mathrm{OF_{det}k_{Q_{clin},Q_{msr}}^{f_{clin},f_{msr}}}$	0.573 (0.006)	0.780 (0.004)	0.868 (0.004)

%) with the expected MC dose in water field factor and with the mean $\overline{\mathrm{OF_{det}}}$ of the microLion, microDiamond and diode D1V measurements (table 5.1).

The volume averaging perturbation ($\mathrm{P_{vol}}$) for the microLion, microDiamond and diode D1V detectors, calculated using eq. 5.6, are estimated to be 1.060 (0.002), 1.045 (0.001), 1.009 (0.001). These results agree within 0.3, 1.0 and 0.1 % respectively with the MC calculated volume averaging perturbations reported in previous work for the same detector designs (Papaconstadopoulos, Tessier, and Seuntjens, 2014), which validates the accuracy of the analytical method outlined in section 5.2.5.

Specifically, for the microLion and microDiamond detectors, if the $\mathrm{P_{vol}}$ is factored out of the overall correction ($\frac{\mathrm{k_{Q_{clin},Q_{msr}}^{f_{clin},f_{msr}}}}{\mathrm{P_{vol}}}$), then an over-response of 0.966 (microLion) and 0.969 (microDiamond) is revealed relative to dose in water. This is consistent with the findings of Azangwe et al., 2014 that reported an over-response of 0.965 (microLion) and 0.961 (microDiamond) and with the findings of Lechner et al., 2013 that reported over-response of 0.962 to 0.973 (microLion) and of 0.961 to 0.969 (microDiamond) for flattened and flattening filter free beams after volume averaging corrections

TABLE 5.3: Volume averaging corrections (Pvol) calculated for the W1 and CHUQ PSD sensitive volume geometries on the parallel (‖) and perpendicular (⊥) orientations to the CAX. The diameter of the PSDs sensitive volume is 1 mm (‖ CAX) and 3 mm (⊥ CAX) respectively. The estimated uncertainties (1 σ) are reported in the parenthesis.

Orientation	0.5×0.5 cm^2	1×1 cm^2	2×2 cm^2
‖ CAX	1.009 (0.001)	1.001 (0.001)	1.000 (0.001)
⊥ CAX	1.063 (0.005)	1.004 (0.001)	0.999 (0.001)

were taken into account. It should be noted that in both studies the measurements were performed in a field size of 0.6 × 0.6 cm^2 using an Elekta Precise accelerator and alanine pellets, corrected for volume averaging, were considered as the reference detector.

The relative detector $\mathrm{OF}_{\mathrm{det}}$ measurements of two similar PSDs (W1 and CHUQ) for field sizes of 0.5 × 0.5, 1 × 1 and 2 × 2 cm^2 are presented in fig.5.4 . Both detectors were calibrated using the spectrum discrimination method. For the field sizes of 1 × 1 and 2 × 2 cm^2, the PSDs agree within 1 % to each other. For the smallest field size of 0.5 × 0.5 cm^2 a relative difference of +5.8 % is observed. It should be noted that the W1 PSD exhibits significantly better precision (< 0.8 %) compared to the CHUQ PSD (< 1.8 %). The $\mathrm{OF}_{\mathrm{det}}$ for the same measurements were recalculated by repeating the calibration procedure in Solid Water™(⊥ CAX) and under the shielded configuration for the CHUQ PSD (table 5.4). A noticeable increase in the CLR values is observed for both PSDs in the level of 2.2 % - 2.5 % if the calibration is performed in the Solid Water™ slab (⊥ CAX). A similar increase is observed for the CHUQ PSD under the shielded calibration method. The CLR increase produces a small but noticeable effect on the $\mathrm{OF}_{\mathrm{det}}$ measurements with the $\mathrm{OF}_{\mathrm{det}}$ of the smallest field size increased by 0.8 % and 0.5 % for the W1 and CHUQ PSDs respectively. It is also observed that the CLR values obtained on the perpendicular calibration orientation exhibit higher precision than the respective calibration on the parallel orientation.

TABLE 5.4: W1 and CHUQ PSD measurements performed in water (∥ CAX orientation) (resolution=1 mm). The calibration procedure was performed both in water (∥ CAX) and in the Solid Water$^{\mathrm{TM}}$ slab (⊥ CAX) and the $\mathrm{OF}_{\mathrm{det}}$ recalculated. The shielded calibration method was also performed for the CHUQ PSD. All uncertainties presented in the parenthesis refer to the 1 σ level.

PSD	Calibration	CLR	0.5×0.5 cm^2	1×1 cm^2	2×2 cm^2
W1	∥ CAX	0.693 (0.005)	0.603 (0.005)	0.784 (0.002)	0.866 (0.002)
W1	⊥ CAX	0.710 (0.001)	0.608 (0.005)	0.790 (0.002)	0.871 (0.002)
CHUQ	∥ CAX	0.814 (0.010)	0.568 (0.008)	0.777 (0.008)	0.866 (0.007)
CHUQ	⊥ CAX	0.832 (0.005)	0.571 (0.009)	0.780 (0.006)	0.866 (0.008)
CHUQ	shielded	0.830 (0.004)	0.571 (0.009)	0.780 (0.006)	0.866 (0.008)

These observations are further explored in fig.5.5 which presents the light spectra collected from the CHUQ PSD under the different calibration set-up configurations. Figure 5.5a demonstrates that the spectra differentiation between max and min fiber irradiations is maximized when the calibration measurements are performed in the Solid Water$^{\mathrm{TM}}$ slab (⊥ CAX). On the contrary, if the max and min fiber irradiations are performed parallel to the CAX in the water tank smaller differences between the spectra are observed. Consequently, subtraction of similar spectra will unavoidably result in increased levels of noise, as observed in fig. 5.5b. Furthermore, the Cherenkov spectra extracted for the parallel CAX calibration method appear to be systematically shifted towards higher wavelengths (fig. 5.5b). Such a shift is expected to increase the relative Cherenkov signal in the green channel (G_{C}) over the blue channel (B_{C}) and consequently reduce the CLR value (eq. 5.4). The above observation explains the systematic shift in CLR values previously reported for the W1 and CHUQ PSDs under the different calibration configurations (table 5.4). However, the relative change of the

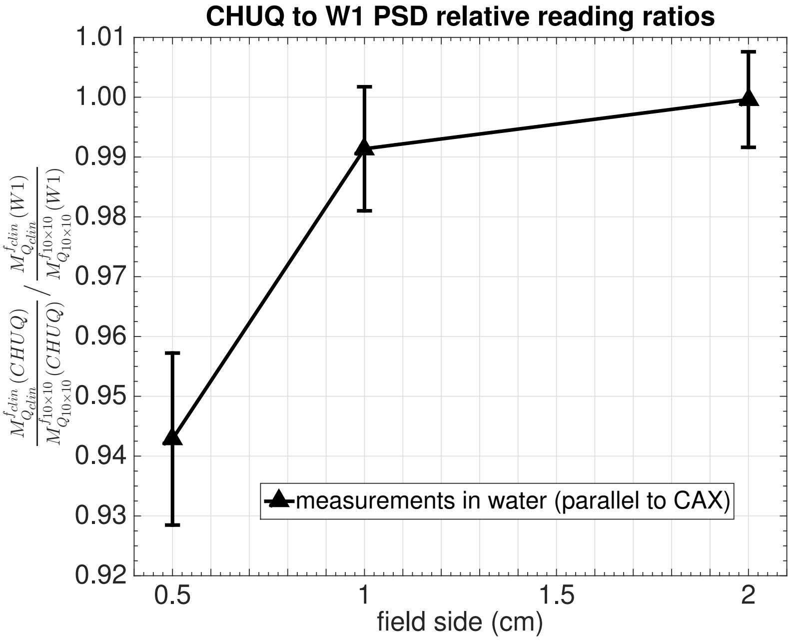

FIGURE 5.4: Relative detector $\mathrm{OF_{det}}$ readings using the W1 and CHUQ PSD. The error-bars present the total propagated (1 σ) standard deviation including jaw repositioning and CLR variations. For the CHUQ PSD the effect of wavelength threshold choice in the 450-550 nm range is also included.

CLR value results in only a small change in the $\mathrm{OF_{det}}$ and does not explain the much more significant discrepancy observed during the measurements under the different set-ups. Pure fiber irradiations under the shielded configuration present Cherenkov spectra in good agreement to the calibration in $\mathrm{Solid\,Water^{TM}}$($\perp$ CAX).

The effect of the wavelength choice to the CLR values is presented in figure 5.6a. The CLR appears to increase monotonically as the wavelength threshold is increased from 450 to 550 nm. This increase results in only a marginal decrease in the $\mathrm{OF_{det}}$ values by about 0.5 $\%$ and by 0.4 $\%$ for the $\parallel$ CAX and $\perp$ CAX calibrations. For the shielded calibration a more significant drop was observed by 1.9 $\%$.

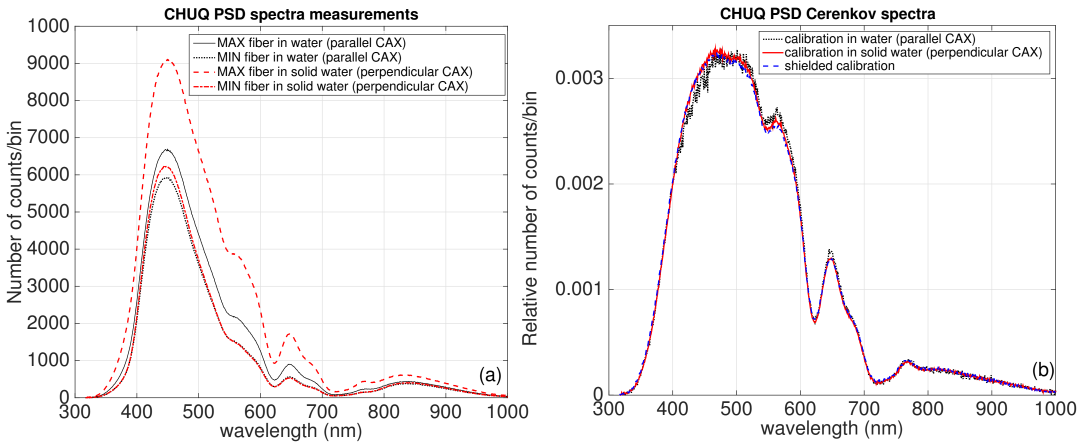

FIGURE 5.5: (a) CHUQ PSD spectra measurements with maximum and minimum fiber lengths irradiated in water (∥ CAX) and Solid Water$^{\text{TM}}$ (⊥ CAX). (b) The subtraction of the max and min fiber spectra results in an estimation of the emitted Cherenkov light spectrum. The Cherenkov spectrum extracted by a pure fiber irradiation (shielded configuration) is also presented.

5.4 Conclusion

In this study we investigated the accuracy of PSDs and especially the commercially available Exradin W1 and the spectrum discrimination calibration method in small photon field $\mathrm{OF}_{\mathrm{det}}$ measurements. The W1 PSD presented systematically higher $\mathrm{OF}_{\mathrm{det}}$ values for the smallest field size of 0.5×0.5 cm^2 relative to microLion, microDiamond and diode D1V readings, after MC-calculated $\mathrm{k}_{\mathrm{Q_{clin}},\mathrm{Q_{msr}}}^{\mathrm{f_{clin}},\mathrm{f_{msr}}}$ factors were applied. In addition, a dependancy on the orientation of the W1 PSD was observed even after appropriate volume averaging corrections were applied. Further research on PSDs is required that would explain the origin of these differences. A relative difference up to +5.8 % was also observed between the W1 PSD and the CHUQ PSD for the smallest field size. Both PSD systems are composed of similar water-like materials and have the same sensitive volume dimensions, thus from the perspective of material and volume averaging perturbations, a similar response was expected. In addition, the

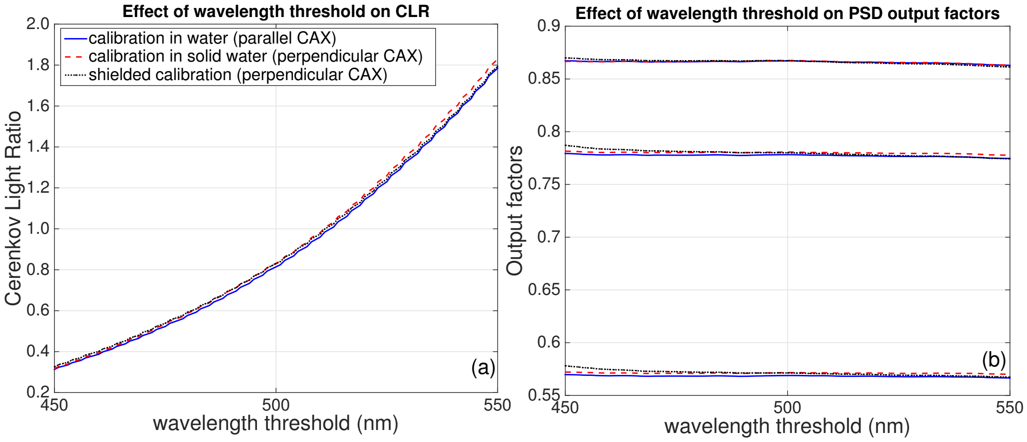

FIGURE 5.6: The effect of wavelength threshold choice on the CLR and $\mathrm{OF}_{\mathrm{det}}$ measurements for the CHUQ PSD under the different calibration set-up configurations

same Cherenkov calibration procedure was followed in both cases. Further research is needed on other components of a PSD system that may possibly affect significantly the response. Dependencies on the fiber material, orientation, numerical aperture, length, bending as well as on the photodetector type (photodiode or photomultiplier tube) and whether the photodetector is present or not in the measurement vault during irradiation should be carefully examined and related to the $\mathrm{OF}_{\mathrm{det}}$ results. The spectrum discrimination method appeared to be an accurate and precise method for extracting the Cherenkov spectrum as long as the fiber length difference between the max and min fiber configuration is maximized.

Acknowledgements

The authors would like to thank Andrea Zens, Shannon Holmes and Chris Bonde from Standard Imaging for valuable technical support. P.P. gratefully acknowledges financial support by the Alexander S. Onassis Public Benefit Foundation in Greece and by the CREATE Medical Physics Research Training Network grant of the Natural Sciences and Engineering Research Council (Grant number: 432290, RGPIN-2014-06475).

Chapter 6

A protocol for EBT3 radiochromic film dosimetry using reflection scanning

Pavlos Papaconstadopoulos, Gyorgy Hegyi, Jan Seuntjens and Slobodan Devic Med. Phys. 41 (12), December 2014

This study investigates potential benefits in radiochromic film dosimetry using the reflection scanning mode to increase the sensitivity and reduce calibration uncertainties in the low dose regions. This could potentially offer advantages in relative dose profile measurements especially in the tail regions. Accurate estimation of the dose in the tail region might be important for proper identification of the source parameters in a beam model. The calibration protocol suggested in this study is used in the next chapter for reconstructing the source intensity distribution using photon fluence profiles.

Abstract The purpose of this study is to evaluate the performance of the EBT3 radiochromic film dosimetry system using reflection measurements and to suggest a calibration protocol for precise and accurate reflection film dosimetry. A set of 14

Gafchromic EBT3 film pieces were irradiated to various doses ranging from 0 to 8 Gy and subsequently scanned using both the reflection and transmission mode. Scanning resolution varied from 50 to 508 dpi (0.5 - 0.05 mm/pixel). Both the red and green color channels of scanned images were used to relate the film response to the dose. A sensitivity, uncertainty and accuracy analysis was performed for all scanning modes and color channels. The total uncertainty, along with the fitting and experimental uncertainty components, were identified and analyzed. A microscope resolution target was used to evaluate possible resolution losses under reflection scanning. The calibration range was optimized for reflection scanning in the low (< 2 Gy) and high (> 2 Gy) dose regions based on the reported results. Reflection scanning using the red channel exhibited the highest sensitivity among all the modes, being up to 150% higher than transmission mode in the red channel for the lowest dose level. Furthermore, there was no apparent loss in resolution between the two modes. However, higher uncertainties and reduced accuracy was observed for the red channel under reflection mode, especially at dose levels higher than 2 Gy. These uncertainties were mainly attributed to saturation effects which were translated in poor fitting results. By restricting the calibration to the 0 - 2 Gy dose range, the situation is reversed and the red reflection mode was superior to the transmission mode. For higher doses the green channel in reflection mode presented comparable results to the red transmission. A two-color reflection scanning protocol can be suggested for EBT3 radiochromic film dosimetry using the red channel for doses less than 2 Gy and the green channel for higher doses. The precision and accuracy are significantly improved in the low dose region following such a protocol.

6.1 Introduction

Radiochromic film has proven to be an attractive dosimeter for quality assurance (QA) measurements of intensity modulated radiation therapy (IMRT) and for commissioning beam models in stereotactic radiotherapy. Some of the features that make a radiochromic film dosimetry system advantageous are the near to water material composition, high resolution, and energy independence in the megavoltage range.

The dosimetry using radiochromic film is based on an opacity change occurring to the film upon radiation due to the polymerization of diacetylene molecules. Traditionally, the dose information is retrieved by a light transmission measurement through the darkened area, $\mathrm{T} = \frac{\mathrm{I_T}}{\mathrm{I_0}}$, where $\mathrm{I_T}$= transmitted light intensity and $\mathrm{I_0}$= incident light intensity (figure 6.1a). It has been demonstrated that flat-bed document scanners can be used for that purpose (Devic et al., 2005). Since transmission exhibits a non-linear dependence to dose, it is often more practical to calibrate the dose to the optical density (OD), defined as $\mathrm{OD} = -\log(\frac{\mathrm{I_t}}{\mathrm{I_0}})$. A key evolution in radiochromic film dosimetry was achieved with the introduction of EBT films (GAFCHROMIC, International Specialty Products, Wayne, NJ). This type of film exhibited increased sensitivity for doses between 0 - 8 Gy, a range of particular interest for radiotherapy purposes. Up to date several researchers have investigated the uncertainty limits of radiochromic film dosimetry using transmission mode (Devic et al., 2005; Van Battum et al., 2008; Bouchard et al., 2009b). Van Battum et al., 2008 reported that an overall standard deviation (1 σ) of 1.8% is achievable for single film measurements. It should be emphasized that the reported uncertainties in most of the studies, refer to dose levels of 2 Gy or higher. Higher uncertainties are usually observed for low dose levels, especially below

2 Gy, mainly due to the lower signal to noise ratio. These dose levels may be important for precise dosimetry on the penumbra and tail regions of dose profiles in external beam radiotherapy (EBRT). Bouchard et al., 2009b have presented a comprehensive list of potential sources of uncertainty in radiochromic film dosimetry.

An alternative way of retrieving the dose information is by a reflection measurement. In such a case the film is placed against a flat, white surface and the light source resides on the same plane as the detector (figure 6.1b). The measurand would then be the total reflection, $\mathrm{R} = \frac{\mathrm{I_R}}{\mathrm{I_0}}$, where $\mathrm{I_R}$= reflected light intensity and $\mathrm{I_0}$= incident light intensity. The optical density can then be defined similarly as $\mathrm{OD} = -\log(\frac{\mathrm{I_R}}{\mathrm{I_0}})$.

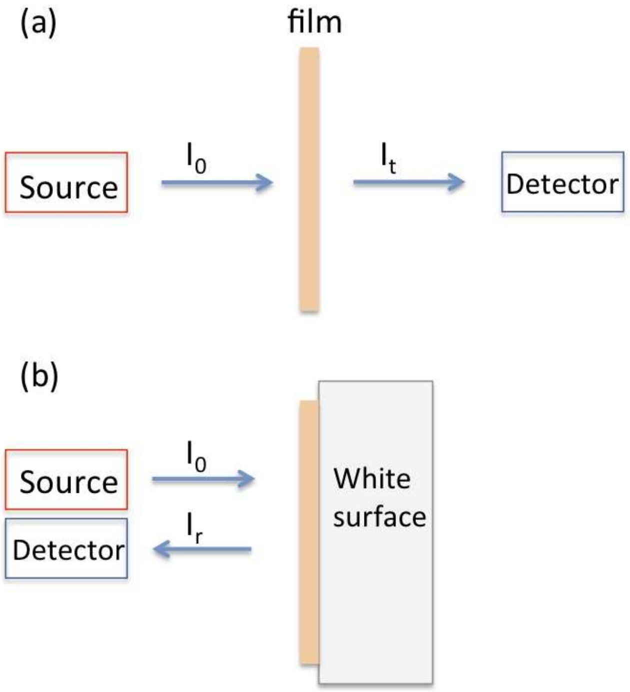

FIGURE 6.1: Graphical representation of film scanning using transmission (a) and reflection (b) measurements.

Alva et al., 2002 investigated the use of reflective scanners for MD-55 radiochromic film dosimetry. They concluded that the red channel exhibited the highest sensitivity and should be preferred for dose levels up to 50 Gy. Kalef-Ezra and Karava, 2008 compared the reflection to the transmission mode for the MD-55 film model. They concluded that the accuracy was comparable between the two scanning methods. More recently Richley et al., 2010 confirmed that the red colour in reflection mode exhibited the highest sensitivity for EBT2 model film. However, they inferred that the much steeper calibration curve under reflection mode will eventually increase the overall dose uncertainty.

The purpose of this work was: 1) to perform a rigorous sensitivity, uncertainty and accuracy analysis comparing the transmission to the reflection mode for the EBT3 radiochromic film model dosimetry system using a flat-bed document scanner. The analysis was performed for both the red and green color channels of scanned images and for multiple scanning resolutions. 2) To evaluate the influence of the fitting and experimental uncertainties to the final precision for each mode. 3) To investigate possible resolution loss under the reflection scanning mode and 4) to suggest an optimum calibration protocol, which would reduce the uncertainties, especially in the low dose levels (< 2 Gy).

6.2 Materials and Methods

6.2.1 Experimental procedure

A set of 14 Gafchromic EBT3 film pieces from the same batch were irradiated to dose levels of 0.00, 0.10, 0.20, 0.30, 0.50, 0.75, 1.00, 1.25, 1.50, 2.00, 3.00, 4.00, 5.00 and 8.00 Gy. Irradiations were performed on a Varian Novalis Tx linear accelerator with a source to surface distance (SSD) of 100 cm, a field size of 10×10 cm^2 and a depth of 5 cm in solid water (GAMMEX, Middleton, WI, USA). An ionization chamber NE2571 (Nuclear Enterprises, Fairfield, NJ) was placed at a depth of 10 cm during the measurements to monitor possible output variations. The nominal doses were scaled based on the chamber readings. The dimensions of each film piece were 6.35×5.08 cm^2 (2.5×2 inch^2). A 1.27×5.08 cm^2 (0.5×2 inch^2) area was allocated solely for labelling and handling purposes. Plastic gloves were used at all times during the measurements. The films were then stored within a black envelope in a controlled environment for a duration of approximately 20 hours to allow self-development. At all times the control film (0 Gy) was handled the same way as the irradiated films. An Epson Expression 11000XL (Epson Seiko Corporation, Nagano, Japan) document scanner was used for the transmission and reflection scans. Transmission and reflection scans were performed for resolutions of 50, 127, 254, 508 dpi (0.5, 0.2, 0.1 and 0.05 mm/pixel) of the unexposed (before the measurements) and exposed films. For the reflection mode, a white surface board was firmly placed behind the films. A scan of a black surface was also performed for each resolution assessment to acquire a background reading. A blank scan was performed for identifying defective pixels. All the scans were saved as 48-bit RGB TIFF images.

6.2.2 Image processing

The image processing was performed using MATLAB R2012b (MathWorks, Natick, MA). As a first step, the exposed pieces of film were rotated and co-registered to the upper left corner of the unexposed films. This was performed to ensure that the region-of-interest (ROI) selected on the unexposed scans coincided with the exposed scans. A 5×5 pixel Wiener filter was applied on the image. A matrix of defective pixels was created based on the blank scans. If a pixel value (PV) in the blank scan was less than 0.995 × maximum PV, then it was considered to be defective. For each resolution, 5 ROIs were randomly selected within the irradiated part of the film with dimensions of 0.4×0.4 cm^2. The mean PV and standard deviation was calculated for each ROI. If a defective pixel happened to reside within the selected ROI, then it was not included in the calculation. Finally, the weighted mean of a set of 5 measurements was calculated. The weights were determined as the inverse of the standard deviation of each ROI. In the following we will refer to the weighted mean of the PV as the measurement (M).

6.2.3 Calibration procedure and metrics

The netOD was calculated by the following formula:

$$\mathrm{netOD} = -\log_{10}\left(\frac{\mathrm{M_{exp}} - \mathrm{M_{bkg}}}{\mathrm{M_{unexp}} - \mathrm{M_{bkg}}}\right) \tag{6.1}$$

,where $\mathrm{M_{unexp}}$: unexposed measurement, $\mathrm{M_{exp}}$: exposed measurement and $\mathrm{M_{bkg}}$: background measurement. The background reading was found to be of the level of 1 - 1.5$\%$ of the measured signal of a blank scan. The netOD of the control film (0 Gy) was subtracted in order to take into account film darkening due to environmental and temporal effects:

$$\Delta\mathrm{netOD} = \mathrm{netOD} - \mathrm{netOD_{0Gy}} \tag{6.2}$$

The experimental dose was related to the $\Delta\mathrm{netOD}$ by the following polynomial function:

$$\mathrm{D} = \mathrm{p} \cdot (\Delta\mathrm{netOD}) + \mathrm{q} \cdot (\Delta\mathrm{netOD})^{\mathrm{n}} \tag{6.3}$$

,where D is the estimated dose, p,q are free parameters and n a problem-dependent parameter. The optimum parameter value n was manually determined for each resolution and color channel. For that purpose, the R^2 and adjusted R^2 values of the fitting process were iteratively examined. The fitting algorithm was based on the Trust-Region (TR) reflective least squares method. Rational and exponential functions were also examined, but did not exhibit significant differences compared to the polynomial case.

The sensitivity was calculated for each dose level as:

$$\mathrm{S} = \frac{\Delta\mathrm{netOD}}{\mathrm{D}^*}, \tag{6.4}$$

where D^* is the actual delivered dose. The dose uncertainties were estimated by applying the standard error propagation method on equation 6.3, assuming no correlation among the variables:

$$\delta\mathrm{D}^2 = \left(\frac{\mathrm{dD}}{\mathrm{dp}}\right)^2 (\delta\mathrm{p})^2 + \left(\frac{\mathrm{dD}}{\mathrm{dq}}\right)^2 (\delta\mathrm{q})^2 + \left(\frac{\mathrm{dD}}{\mathrm{d}\Delta\mathrm{netOD}}\right)^2 (\delta\Delta\mathrm{netOD})^2 \tag{6.5}$$

In the following the first two terms of equation 6.5 will be considered as the dose uncertainty due to fitting and the last term due to experiment, similarly to what has been described in previous work (Devic et al., 2004).

The accuracy of the calibration process can be evaluated by the following formula:

$$A = 100 \cdot \frac{|D - D^*|}{D^*}, \tag{6.6}$$

where D is the estimated dose by equation 6.3 and D^* is the actual delivered dose. The fitting process was repeated for the transmission and reflection mode for the red channel using a calibration range of 0 - 4 Gy and 0 - 2 Gy. The purpose was to investigate trends and potential benefits in the low dose region (0 - 2 Gy) as the calibration range is restricted in different scanning modes. The total uncertainty and accuracy of the different protocols were re-calculated for all scanning resolutions using equation 6.5 and 6.6. All uncertainties presented in this study refer to the level of 1 standard deviation. Uncertainties were propagated using the standard error propagation as suggested in GUM (Mesures, internationale, and normalisation, 1995). Table 6.1 summarizes all the uncertainties addressed in this work, their type (A or B) and the actions performed to reduce their effect.

6.2.4 Resolution analysis

In order to establish possible resolution loss under the different scanning modes, the modulation transfer function (MTF) was measured for both the transmission and reflection modes and for both the green and red channel. The MTF was calculated based on the procedure suggested by Droege and Morin, 1982 using a microscopy resolution target (Edmund Optics, NBS 1963A) with a resolution range of 1 -18 cycles/mm. The resolution target was scanned under the same conditions as the irradiated film pieces.

TABLE 6.1: Film sources of uncertainty and actions performed to reduce their effect.

Source of uncertainty	Type	Action
Linac output variations	A	Scale nominal doses according to ion chamber readings
Dose variations in flat dose region	A	Use of multiple ROIs and apply Wiener filter
Dose variations within ROI	A	Use of multiple pixels within ROI
Film registration	B	Rotate and align the exposed to the unexposed films
Temperature and humidity effects	B	Use of control film (0 Gy level)
Sensitivity to light	B	Store all films in a closed black envelope
Stabilization of chemical reaction	B	Allow 20 hours to pass before scanning
Dust, fingerprints, scratches etc	B	Use plastic gloves and allocate area for handling and labelling
Scanner homogeneity	B	Scan films in the middle of the scanner
Scanner orientation dependency	B	Scan parallel to the detector motion
Dark noise	B	Subtract background (zero-light intensity) reading
Defective detector elements	B	Derive a matrix of defective pixels
Fitting function	B	Examine different functional formulas
Fitting optimization	B	Trust-Region reflective least squares algorithm

A ROI was selected within each frequency bar pattern. The ROI's mean PV and the standard deviation (σ_{ROI}) were calculated. The MTF was then calculated as Droege and Morin, 1982:

$$\mathrm{MTF(f)} = \frac{\pi\sqrt{2}}{2}\frac{\sigma_{\mathrm{ROI}}(\mathrm{f})}{\mathrm{W}-\mathrm{B}} \tag{6.7}$$

,where W= mean PV of a uniform white region and B= mean PV of a uniform black region. The procedure was repeated 8 times in total for each frequency, color channel, scanning mode and scanning resolution. The final MTF and uncertainty reported were estimated as the mean and standard deviation of all measurements.

6.3 Results and Discussion

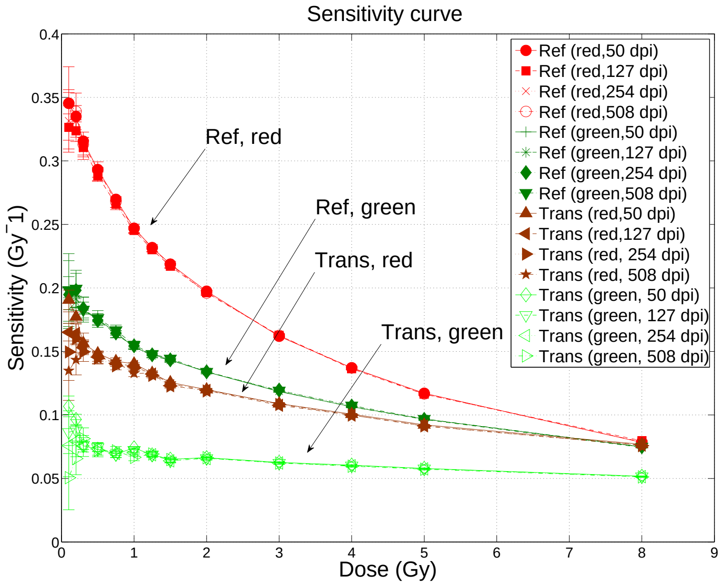

FIGURE 6.2: Sensitivity as a function of dose for reflection and transmission scanning modes.

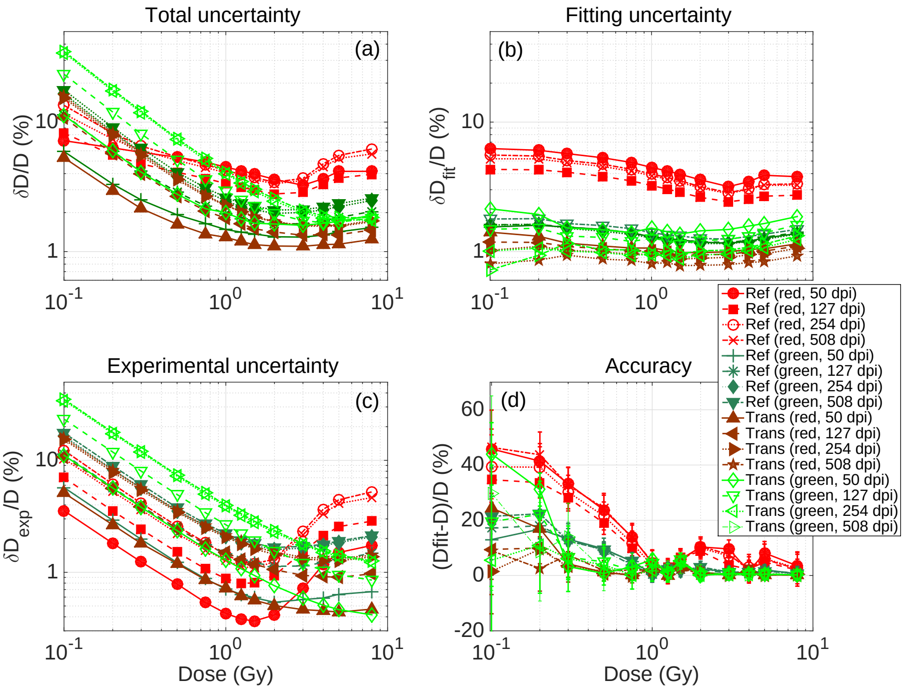

FIGURE 6.3: Total (a), fitting (b), experimental (c) relative uncertainties and accuracy (d) as a function of dose

Figure 6.2 compares the sensitivity of the transmission to the reflection mode as a function of dose for scanning resolutions ranging from 50 - 508 dpi (0.2 - 0.05 mm/pixel). It can be inferred that the red channel under reflection scanning exhibited the highest sensitivity for all resolutions and dose levels. The maximum sensitivity was reached for the lowest dose level and was higher than the red transmission mode by 80% (50 dpi), 97% (127 dpi), 120% (254 dpi) and 150% (508 dpi). The green reflection mode presented comparable results to the red transmission mode for the full dose range of 0 - 8 Gy. Finally, the green transmission mode exhibited the lowest sensitivity in all cases. For each scanning mode, all resolutions presented similar sensitivity above 0.5 Gy.

Figure 6.3a presents the total relative uncertainty for the transmission and reflection modes and for all scanning resolutions. The lowest uncertainties were found for

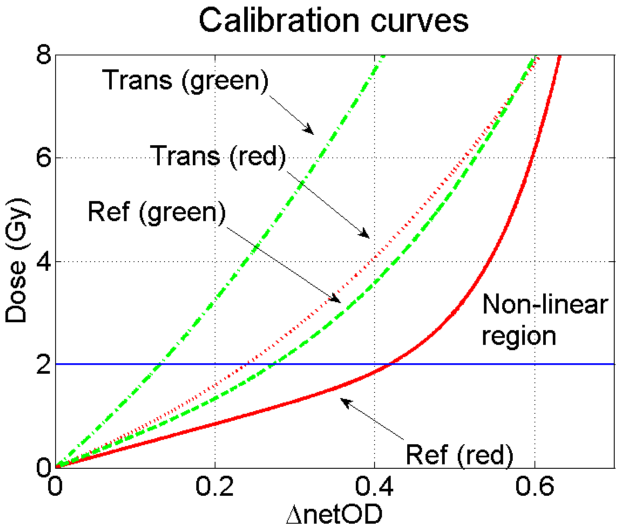

FIGURE 6.4: Calibration curves for the transmission and reflection modes for the red and green channel. A non-linear region is identified for doses higher than 2 Gy for the red reflection mode. The scanning resolution was 254 dpi.

the red transmission mode and was within 1.1 - 1.6 % depending on the scanning resolution. This generally agrees with the estimation provided by Van Battum et al., 2008 (1.8 %). It can be observed that the green reflection mode presented comparable results with the lowest uncertainties ranging between 1.3 - 2.1 %. The red reflection mode was in general inferior than the previous cases, especially for the 50 dpi. As the dose increased, the relative uncertainties were in general reduced. However, there was an interesting increase again of the total uncertainty of the red reflection mode as the dose level of 2 Gy was exceeded.

The previous observations can be better understood by analyzing the uncertainty components. Figures 6.3b and 6.3c present the relative uncertainties due to fitting and experiment. It can be seen that the fitting procedure was mainly responsible for the high total uncertainties of the red reflection mode. In fact, the experimental uncertainties indicate that the red reflection mode was superior compared to all other channels up to the level of approximately 2 Gy, where the experimental uncertainties started to

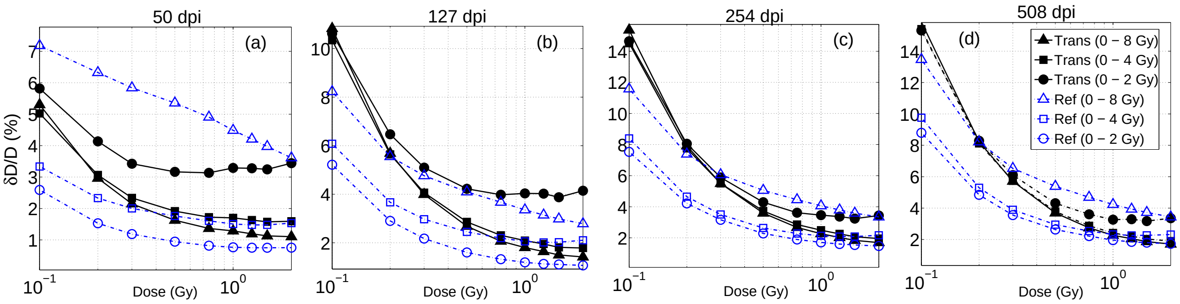

FIGURE 6.5: Total relative uncertainty as a function of dose for the red channel. The calibration procedure was performed within a dose range of 0 - 8 Gy , 0 - 4 Gy and 0 - 2 Gy.

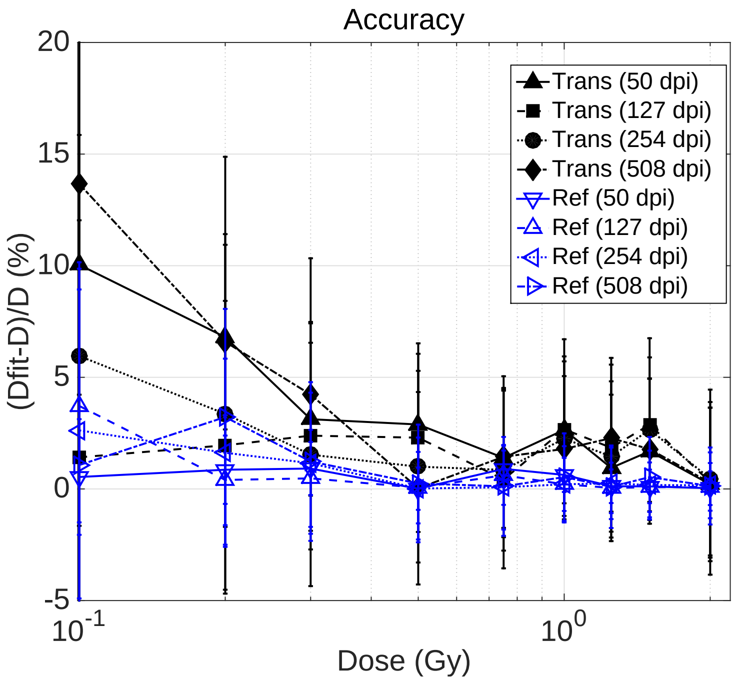

FIGURE 6.6: Accuracy analysis in the low dose region (< 2 Gy) for the red channel. The calibration was performed in the dose range of 0 - 2 Gy.

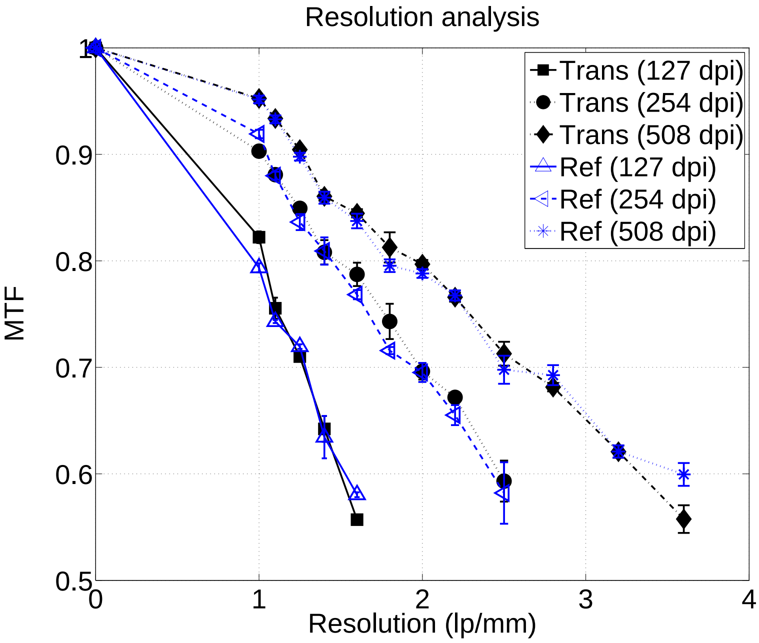

FIGURE 6.7: The modulation transfer function (MTF) calculated for the red channel and for resolutions of 127, 254 and 508 dpi.

increase again. For the rest of the scanning modes and color channels the fitting uncertainties were in general within a range of about 0.7 - 2.1 %. Besides the previously mentioned red reflection mode, the experimental uncertainties were the main contributor to the total uncertainty. The green transmission mode presented the worst case, as expected due to its relatively low sensitivity (figure 6.2).

Figure 6.3d shows the accuracy of the transmission and reflection modes. It was observed that for all resolutions and dose levels the red reflection mode was inferior to the rest of modes. For the low dose levels (< 2 Gy) the red transmission mode presented most often the best accuracy, which in most cases was within 10 %. For the higher dose levels the red transmission, green transmission and green reflection presented comparable results to each other with an accuracy level within 5 %. The high fitting uncertainties reported for the red reflection mode can be understood by looking at the calibration curves (figure 6.4). It can be observed that beyond a dose level of about 2 Gy the red reflection calibration curve becomes highly non-linear. This is mainly due to saturation effects and will unavoidably result in high uncertainties and accuracy loss during the fitting procedure. It should be noted that an alternative way of minimizing the fitting uncertainties would be the utilization of spline interpolation methods, even though this is not a commonly used method in film dosimetry. The remaining scanning modes did not present such steep non-linearities. This problem could potentially be bypassed if the calibration dose range was restricted to lower doses. Figure 6.5 presents the relative total uncertainties in the dose range of 0 - 2 Gy with the fitting procedure performed for ranges of 0 - 2 Gy, 0 - 4 Gy and 0 - 8 Gy. Only the red channel was investigated for the reflection and transmission mode. It can be observed that the red reflection mode presented the lowest uncertainties for all dose levels if the calibration is restricted between 0 - 2 Gy. Specifically, for the dose level of 0.1 Gy and for a resolution of 50 dpi the red reflection mode reached a total uncertainty of about 2.6 % (instead of 7.2 % for the red transmission mode), while for a resolution of 508 dpi and for the same dose level the red reflection showed uncertainties of about 8.8 % (instead of 15.3 % for the red transmission mode). If the calibration is restricted between 0 - 4 Gy the transmission mode presented comparable or slightly lower uncertainties than the reflection mode for doses higher than 1 Gy. For lower doses the reflection mode was still superior. It is also interesting to stress that transmission and reflection modes presented opposite trends: as the calibration range was gradually restricted the uncertainties on the transmission mode were increased, while for the reflection mode were reduced. Figure 6.6 represents the accuracy of transmission and reflection modes for the red channel if calibrated within the 0 - 2 Gy range. The reflection mode presented an accuracy level within 3.7 % in all cases, while the transmission mode showed discrepancies up to 10 %. Specifically in the clinically important region of 1 - 2 Gy, the reflection mode exhibited an accuracy within 0.6 % in all cases, while the transmission mode was within 2.7 % in the same region.

Figure 6.7 presents the MTF as calculated by equation (7) for the microscope resolution target. The reflection and transmission modes were investigated for the red channel and for resolutions of 127, 254 and 508 dpi. The case of the 50 dpi was also investigated, but not reported since none of the available frequencies could be resolved for this scanning resolution. The MTF agreed for both scanning modes within 1 standard deviation in most cases. Thus, it can be inferred that there was no resolution loss in the reflection mode compared to transmission.

6.4 Conclusions

In this work we investigated the performance of EBT3 model based radiochromic film dosimetry system in both the transmission and reflection scanning modes using either the red or green color channel of the scanned film images. A two-color protocol is suggested for EBT3 model based radiochromic film dosimetry system using solely the reflection mode in the dose range of 0 - 8 Gy: for low doses (0 - 2 Gy) the calibration is performed with the red channel, while for higher doses (2 - 8 Gy) the calibration is performed with the green color. Alternatively, the transmission scanning mode in the red channel could be used in the high dose region. However, this option would require to scan the films in both modes, thus doubling the workload. The improved performance of the reflection mode using the red channel in the low dose regions may result in more precise and accurate dosimetry in the penumbra and tail regions of stereotactic dose profiles or IMRT plans.

Acknowledgements

P.P. gratefully acknowledges financial support by the Alexander S. Onassis Public Benefit Foundation in Greece and by the CREATE Medical Physics Research Training Network grant of the Natural Sciences and Engineering Research Council (Grant number: 432290). This work was supported also in part by the Natural Sciences and Engineering Research Council of Canada Contracts No. 386009. S.D. is a Research Scientist supported by the Fonds de Recherche en Santè du Quebèc (FRSQ) 26856.

Chapter 7

Direct reconstruction of the source intensity distribution of a clinical linear accelerator using a maximum likelihood expectation maximization algorithm

Pavlos Papaconstadopoulos, Ives Levesque, Robert Maglieri, and Jan Seuntjens

accepted for publication in Phys. Med. Biol. 61 (2016) 1078–1094

This study suggests a method that can be used for directly reconstructing the source intensity distribution of clinical linear accelerators, without making any assumptions about the source functional form. This can serve as an alternative path to determine the appropriate source parameters than iterative tuning a beam model and applying detector-specific correction factors on measurements.

Abstract Direct determination of the source intensity distribution of clinical linear accelerators is still a challenging problem for small field beam modeling. Current techniques most often involve special equipment and are difficult to implement in the clinic. In this work we present a maximum-likelihood expectation-maximization (MLEM) approach to the source reconstruction problem utilizing small fields and a simple experimental set-up. The MLEM algorithm iteratively ray-traces photons from the source plane to the exit plane and extracts corrections based on photon fluence profile measurements. The photon fluence profiles were determined by dose profile film measurements in air using a high density thin foil as build-up material and an appropriate point spread function (PSF). The effect of other beam parameters and scatter sources was minimized by using the smallest field size (0.5×0.5 cm^2). The source occlusion effect was reproduced by estimating the position of the collimating jaws during this process. The method was first benchmarked against Monte Carlo simulations for a range of typical accelerator source sizes. The sources were reconstructed with an accuracy better than 0.12 mm in the full width at half maximum (FWHM) to the respective electron sources incident on the target. The estimated jaw positions agreed within 0.2 mm with the expected values. The reconstruction technique was also tested against measurements on a Varian Novalis Tx linear accelerator and compared to a previously commissioned Monte Carlo model. The reconstructed FWHM of the source agreed within 0.03 mm and 0.11 mm to the commissioned electron source in the crossplane and inplane orientations respectively. The impact of the jaw positioning, experimental and PSF uncertainties on the reconstructed source distribution was evaluated with the former presenting the dominant effect.

7.1 Introduction

Advanced radiotherapy techniques, such as stereotactic radiosurgery (SRS) and intensity modulated radiation therapy (IMRT), commonly utilize small radiation fields ($< 2 \times 2$ cm^2) in order to improve target coverage and reduce the dose to surrounding organs at risk (OAR). However, accurate commissioning of beam models for small fields still appears to be challenging. Most detectors often present significant perturbations in small fields due to volume averaging or the presence of high density materials. During beam model commissioning of linear accelerators, these perturbations may result in mis-configuration of crucial beam parameters in the treatment planning system (TPS). Systematic errors introduced at this step will eventually propagate as dosimetric errors at the patient dose calculation stage.

In order to address this issue, one approach is to apply detector-specific correction factors directly on the measurements (Alfonso et al., 2008). Several researchers have shown that corrections for output factors can be derived by Monte Carlo (MC) methods (Cranmer-Sargison et al., 2011; Francescon et al., 2012). Similar corrections may be needed for dose profiles as well, especially in the tail region (Papaconstadopoulos, Tessier, and Seuntjens, 2014; Francescon, Kilby, and Satariano, 2014). The MC-derived correction factors have been validated by experimental methods (Pantelis et al., 2012). However, deriving such corrections is a lengthy process and requires MC expertise as well as detailed knowledge of the design and materials of the detector. Furthermore, each time a new detector is produced, new correction factors are needed. It is clear that alternative pathways for determining the appropriate beam parameters would offer a great service in the dosimetry of small fields.

One of the most important beam parameters is the source size and shape of clinical linear accelerators. In MC beam models, the term source most often refers to the electron spatial distribution incident on the target. In other beam models, it may refer to the bremsstrahlung radiation that is produced in the target, often referred to as the primary X-ray source or focal-spot. In both cases, the source size is most often characterized by the full width at half maximum (FWHM) and the shape is assumed to be a 2D elliptical Gaussian distribution. Sterpin et al., 2011 showed that for a nominal 5.5 and 18.0 MeV incident electron energies, the primary X-ray source is located approximately at a depth of 0.13 and 0.25 mm respectively from the top of the target. It was also shown in that study that the photon source FWHM agrees within 0.06 mm to the electron source FWHM for typical source sizes of 0.5 to 1.5 mm. This important conclusion implies that if direct reconstruction techniques could be developed for the X-ray source, then the electron source could be reproduced as well within the previously stated level of accuracy. Other beam parameters, such as the energy of the incident electron source, have a limited effect in small fields. Furthermore, methods for determining the incident electron energy or even unfolding the full energy spectrum of linear accelerators have been suggested (Ali, McEwen, and Rogers, 2012).

As the field becomes small, the primary X-ray source, as seen from the point of measurement, starts to be partially occluded (Aspradakis, 2010). Photons originating from other scatter sources, such as the flattening filter and primary collimator (extra-focal spot), are almost completely blocked and their dosimetric impact is minimized. The magnitude of the source occlusion effect not only depends on the spatial extent of the primary X-ray source, but also on the exact position of the collimators that define the field (Scott, Nahum, and Fenwick, 2009). Thus, any model attempting to reproduce the source occlusion effect should reconstruct both the source and collimator positions at the time of measurements.

Several methods have been suggested for measuring the X-ray source directly. These methods may involve a multiple slit γ camera (Lutz, Maleki, and Bjärngard, 1988), determining the inverse Abel transformation of the derivative of fluence profiles (Treuer et al., 1993), output ratios (Zhu, Bjärngard, and Shackford, 1995) or a micro-leaf collimator (MLC) (Treuer et al., 2003). Perhaps the most widely known and accurate technique is using a rotating slit collimator and a CT reconstruction algorithm (Munro, Rawlinson, and Fenster, 1988; Jaffray et al., 1993; Caprile and Hartmann, 2009). Other researchers applied a similar method using a moving slit (Loewenthal et al., 1992; Sham et al., 2008). However, the experimental set-up of a slit collimator technique is difficult to implement and perform routinely in a clinical environment. Furthermore, Chen et al., 2011 exhibited that the accuracy of this technique depends strongly on the choice of slit width, height and distance to the source.

An interesting finding by some of the previous investigations was that the X-ray source may not follow a Gaussian functional form (Chen et al., 2011; Sham et al., 2008). Furthermore, the source distribution may vary with time (Jaffray et al., 1993) or as currents in the magnets of the electron beam are altered (Munro, Rawlinson, and Fenster, 1988). Despite the above facts, there is currently no requirement for the physicist to directly measure the source as part of the TPS commissioning or of the linac quality assurance procedure.

The purpose of this work is to suggest a method, including a model and an experimental procedure, that would allow the direct reconstruction of the primary X-ray source distribution as generated in the target using clinical measurements. The model is based on iteratively ray-tracing photons from the target to the measurement plane and vice-versa using a maximum-likelihood expectation-maximization (MLEM) algorithm. No prior assumptions on the source distribution or size are needed. The experimental procedure involves the determination of photon fluence profiles in small fields in air using film measurements and a thin lead (Pb) foil as a build-up material. Blurring effects due to the non-zero electron range and photon scatter are taken into account by convolution with pre-calculated point spread functions (PSF). The method also estimates the appropriate collimator settings that reproduce the source occlusion effect for the given accelerator geometry and measurement set. The accuracy of the method in reconstructing the correct source size and shape is first evaluated by performing MC simulations of the experimental set-up for a range of electron sources and then experimentally by performing measurements on a linear accelerator with known MC beam model parameters.

7.2 Methods

7.2.1 The inverse problem

Assuming that the photon fluence distribution can be measured at the bottom of the linear accelerator (exit plane, fig. 7.1a), the question we are seeking to answer is how the source fluence distribution can be reconstructed at the top of the target (source plane, fig. 7.1a). This question defines an imaging problem to derive an object representation from an initial blurred image. This is referred to as the inverse problem in image reconstruction and iterative methods are commonly applied to address it. In the following, the method will be explained as applied in the source reconstruction problem. In this work we will only consider 1-D fluence distributions and the reconstruction is performed on the crossplane and inplane orientations separately.

7.2.2 Extracting the system matrix

As a first step, the relationship between each pixel on the source plane needs to be associated, by geometric means, to each pixel on the exit plane. Let's assume the case of a source pixel j (figure 7.1a). Photons originating from pixel j can potentially reach any of the exit pixels $\{i, i+1, \ldots, i+k\}$ that are visible through the collimation aperture. Rays that exceed the collimation limits and are incident on a collimation block are assumed to be completely absorbed. This relationship can be expressed numerically by a matrix, commonly known in imaging as the system matrix. Each column of the matrix is associated to a source pixel, while each row to an exit pixel. Thus, in the previous example the column j will be assigned "0" everywhere except rows $\{i, i+1, \ldots, i+k\}$, where "1" is assigned. The process is then repeated for all source pixels. The system matrix essentially models geometrically the source occlusion effect, pixel-by-pixel, for the particular accelerator design. In this work the system matrix had a resolution of 0.01 mm on both the source and exit plane.

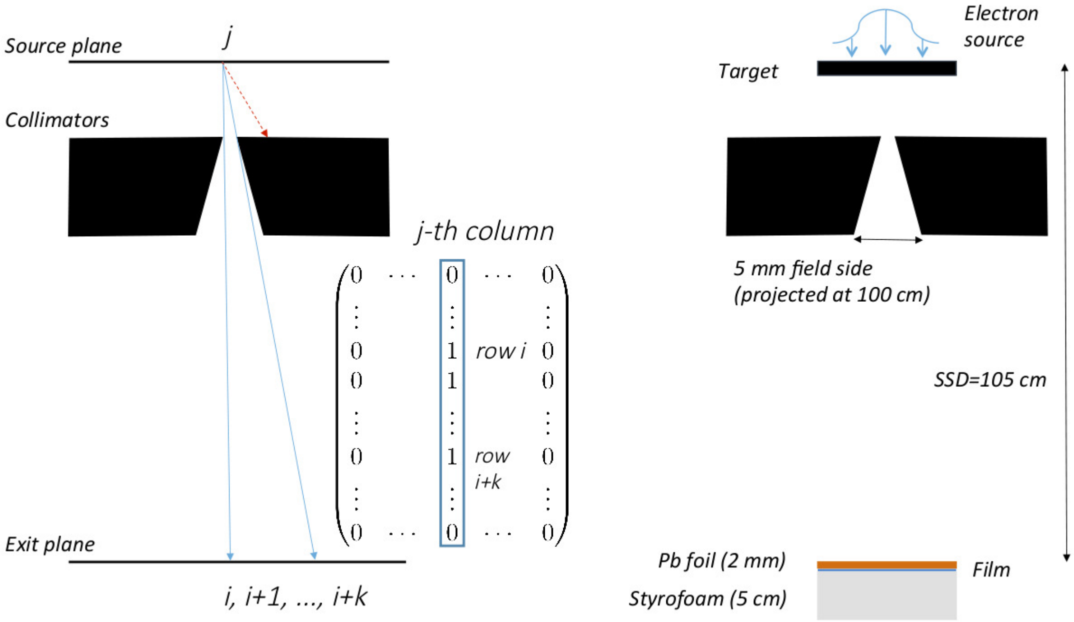

FIGURE 7.1: (a) Modeling the geometrical source occlusion by the system matrix. Rays passing through the collimation aperture (blue solid lines) and reach the exit plane are assigned "1", while rays completely blocked (red dashed line) are assigned "0" on the corresponding positions on the system matrix. (b) The experimental set-up for the measurement of the photon fluence in air. Dimensions in figures are not to scale.

7.2.3 The MLEM reconstruction algorithm

After the system matrix is derived it can be used to reconstruct the image of a given source distribution. The source fluence can be iteratively determined for a given measured exit fluence by the MLEM reconstruction technique (Shepp and Vardi 1982, Reader and Verhaeghe 2014). The following steps summarize the process:

1. First, make an arbitrary estimation of the source distribution vector. For example, assume $\varphi_j = 1$, for all j (uniform distribution).

2. Ray-trace the photons forward to the exit plane to determine the expected fluence distribution vector on the exit plane, $\boldsymbol{q}$. To do so, multiply the system matrix $\boldsymbol{A}$ with the latest source distribution vector estimation $\boldsymbol{\varphi}$.

$$\boldsymbol{q} = \boldsymbol{A}\boldsymbol{\varphi} \tag{7.1}$$

3. Derive the exit fluence profile correction vector $\boldsymbol{k}$ by dividing, pixel-by-pixel, the actual fluence measurements $\boldsymbol{m}$ by the latest estimation of the exit fluence profile $\boldsymbol{q}$.

$$\mathrm{k_i} = \frac{\mathrm{m_i}}{\mathrm{q_i}} \tag{7.2}$$

4. Ray-trace the correction ratios back to the source plane to determine the expected fluence corrections, $\boldsymbol{c}$, on the source plane. To do so, multiply the transpose

system matrix $\boldsymbol{A}^T$ with the latest profile correction $\boldsymbol{k}$ on the exit plane.

$$\boldsymbol{c} = \boldsymbol{A^T}\boldsymbol{k} \tag{7.3}$$

5. Normalize each source pixel correction, $\mathrm{c_j}$, to the number of exit pixels contributing to this pixel by dividing element-by-element with the sensitivity image, $\boldsymbol{s} = \boldsymbol{A^T}\boldsymbol{1}$.

$$\mathrm{c_j^n} = \frac{\mathrm{c_j}}{\mathrm{s_j}} \tag{7.4}$$

6. Finally, derive a new estimation of the source distribution vector $\boldsymbol{\varphi^{new}}$ by multiplying, pixel-by-pixel, the latest source estimation $\boldsymbol{\varphi}$ with the normalized source profile correction vector $\boldsymbol{c}^{\mathrm{n}}$.

$$\varphi_{\mathrm{j}}^{\mathrm{new}} = \varphi_{\mathrm{j}}\mathrm{c_j^n} \tag{7.5}$$

Steps (ii)-(vi) are repeated iteratively until some stopping criterion is met. In this work, we assume that the algorithm converges if the FWHM of the source has not changed more than 2% in the last 30 iterations. In a condensed form the MLEM algorithm can be written as:

$$\boldsymbol{\varphi^{new}} = \frac{\boldsymbol{\varphi}}{\boldsymbol{A^T}\boldsymbol{1}}\boldsymbol{A^T}\frac{\boldsymbol{m}}{\boldsymbol{A}\boldsymbol{\varphi}} \tag{7.6}$$

,where vector-vector multiplications and divisions are performed element-by-element.

7.2.4 Experimental set-up

The experimental set-up used in this work can be seen in figure 7.1b. To measure the photon fluence at the exit plane of the linear accelerator dose profile measurements were performed in air using radiochromic film. The measurements were performed on a Varian Novalis Tx linear accelerator (Varian Medical Systems, Palo Alto, CA, USA) at the SRS mode (6 MV). The contribution of backscattered radiation was minimized by placing the films on a 5 cm block of styrofoam. Monte Carlo simulations were performed to verify that the styrofoam block does not change the dose profile distribution. To reduce the impact of contaminant electrons incident on the surface and the blurring due to electron range, a Pb foil of 2 mm thickness was used as a build up material. The thickness of the build-up was chosen based on the average electron energy reaching the phantom surface. The Source to Surface Distance (SSD) at the top of the foil was set to 105 cm. In order to maximize the sensitivity to the primary X-ray source and reduce the impact of other beam parameters or scatter sources, the measurements were performed solely in the smallest field size of 0.5×0.5 cm^2. The field size was defined by the secondary collimators (jaws) as projected to a SSD of 100 cm. The top surface of the inplane (Y) and crossplane (X) jaws reside at 28.0 cm and at 36.7 cm respectively from the top of the target.

7.2.5 Blurring in the Pb foil

Even though the high density Pb foil reduces the blurring, due to the smaller electron range, it does not eliminate the effect. Furthermore, photon scattering in the phantom will contribute in penumbra broadening. This blurring can be modeled by a point spread function, $\mathrm{PSF}(x)$. The dose in water after the Pb foil, $(D_w)_{pb}(x)[\mathrm{Gy}]$, can then be expressed as a convolution operation between the photon fluence, $\Phi(x)[\mathrm{cm}^{-2}]$ and the $\mathrm{PSF}(x)[\mathrm{Gy\,cm}^2]$ (eq. 7.7). The latter includes the unit conversion from fluence to dose.

$$(D_w)_{pb}(x) = (\Phi * \mathrm{PSF})(x) = \int_{-\infty}^{+\infty} \Phi(\tau)\mathrm{PSF}(x-\tau)\, d\tau \tag{7.7}$$

To extract the optimum PSF, an optimization procedure based on MC simulations was followed. First, a Pearson VII functional form was chosen for parameterizing the PSF (eq. 7.8).

$$\mathrm{PSF}(x;\gamma,n) = \left(\frac{\gamma^2}{\gamma^2 + (2^{1/n}-1)\cdot x^2}\right)^n \tag{7.8}$$

As a second step, MC simulations using the accurate accelerator model were performed to calculate the photon fluence, $\Phi(x)$, and dose in water after the Pb foil, $(D_w)_{pb}(x)$. The values of γ and n were varied in a systematic manner following a brute-force approach. For each set of estimated parameter values $(\hat{\gamma},\hat{n})$ the dose profile was deconvolved with the PSF($x;\hat{\gamma},\hat{n}$), using a maximum likelihood algorithm, to extract an estimation of the photon fluence, $\hat{\Phi}(x;\hat{\gamma},\hat{n})$. The optimum set of parameter values $(\hat{\gamma},\hat{n})_{opt}$ were determined by minimizing the mean square relative error (MSRE) between estimated and MC calculated photon fluence (eq. 7.9).

$$(\hat{\gamma}, \hat{n})_{opt} = \arg\min_{\gamma,n} \frac{1}{N} \sum_{i}^{N} \left(\frac{\hat{\Phi}_i}{\Phi_i} - 1 \right)^2 \tag{7.9}$$

The above procedure was also performed for other PSF models, including Gaussian and Lorentzian functions, which presented inferior performance than the Pearson VII. The sensitivity of the extracted PSF to the electron source size used in the MC simulation was evaluated by repeating the above procedure for electron source FWHM values of 0.5, 1.0, 1.5 and 2.0 mm and calculating the average PSF and standard deviation (1 σ). The blurring effect was inherently included in the model by convolving each column of the system matrix with the average PSF.

7.2.6 Determining the collimator jaw position

The exact jaw position at the time of measurements defines the projected field size and thus affects the system matrix. In order to determine the jaw position for a nominal projected field size of 0.5×0.5 cm^2 at a SSD of 100 cm, the collimator position varied from 0.4 to 0.6 cm with a step of 0.01 cm. For each jaw position the system matrix was re-calculated and the source reconstruction repeated. The jaw position for which the extracted system matrix minimized the mean local error between calculated and measured dose profiles in the 90 $\%$ - 10 $\%$ dose range was selected as the closest to the true value.

7.2.7 Film measurements

The dose profile measurements were performed using Gafchromic EBT3 film (GAFCHROMIC, International Specialty Products, Wayne, NJ). The film calibration was performed using the red channel in the region of 0-2 Gy and the reflection scanning mode. This calibration protocol has shown to increase the sensitivity and reduce the uncertainties in the low dose regions (Papaconstadopoulos et al., 2014), such as those presented in the profile penumbra. A set of 5 film irradiations were performed. The dimensions of each film piece were 6.35×5.08 cm^2. Before each irradiation the jaws were repositioned to a nominal 0.5×0.5 cm^2, in order to include mechanical jaw positioning errors in the uncertainty analysis. An Epson Expression 11000XL (Epson Seiko Corporation, Nagano, Japan) document scanner was used for the scans in reflection mode. The scanning resolution was set to 127 dpi (0.2 mm/pixel). The profiles were re-sampled to a resolution of 0.01 mm using a cubic spline interpolation method.

7.2.8 Monte Carlo simulations

An accurate model of the Varian Novalis Tx was used for performing the MC simulations of the electron and photon transport in the accelerator using the EGSnrc/BEAMnrc user code (Rogers et al., 1995). An elliptical Gaussian distribution was chosen as the electron source incident on the target. The field sizes were defined by the secondary collimators (jaws) as projected to a SSD of 100 cm. The model was commissioned for small fields in previous work (Papaconstadopoulos, Tessier, and Seuntjens, 2014). The commissioning process resulted in an electron source of FWHM equal to 1.25 mm and 1.10 mm for the crossplane (X) and inplane (Y) orientations respectively. The optimal jaw positions were found to define a projected field side of 4.7 mm and 4.9 mm for the crossplane and inplane orientations respectively. The commissioned model presented a local dose accuracy level within 3 % for dose profiles and within 1.5 % for output factors compared to measurements in small and large fields. For the dose calculation part the EGSnrc/DOSXYZnrc code was used (Walters, Kawrakow, Rogers, et al., 2005). To extract the photon fluence distribution a phase-space file was saved at the bottom of the accelerator at a SSD of 105 cm. To simulate the experimental set-up, a Pb foil of 2 mm thickness was included in the accelerator model at a SSD of 105 cm. For all dose calculations the voxel dimensions were set to $1 \times 1 \times 1$ mm^3. For the accelerator and dose calculation simulation part the electron cut-off (ECUT) values were set to 700 keV and 521 keV respectively. The choice of a lower ECUT value for the DOSXYZnrc simulation was made in order to increase the accuracy of dose deposition during electron transport in small voxels. The photon cut-off (PCUT) value was set to 10 keV in all cases.

7.2.9 Method evaluation

The ability of the method to reconstruct the correct source size and shape was first benchmarked against MC simulations of the experimental set-up of known Gaussian electron sources. The collimating jaws were kept to the commissioned values. The calculated profiles $(\mathrm{D_w})_{\mathrm{Pb}}$ were first re-sampled to a resolution of 0.01 mm and then used as an input to the reconstruction algorithm. The reconstructed FWHM and jaw positions were then directly compared to the expected values.

Since some widening of the electron source may exist due to electron scattering in the target, the photon source distribution at a depth of 0.2 mm from the top of the target was also reported. The depth was chosen based on the results reported by Sterpin et al., 2011 and taking into account that the incident energy was higher in this work (6.1 instead of 5.5 MeV).

In order to evaluate the accuracy of the reconstruction method, the reconstructed source distribution was directly compared to the Gaussian electron source distribution that was used as an input to the MC calculation. The reconstructed source was also compared to the photon source distribution. In addition, a Gaussian fit was performed on the reconstructed source and the normalized root mean square error, RMSE (%), between the fitted Gaussian and reconstructed source was reported. The RMSE was calculated in the 100 - 5 % intensity region and normalized to the mean value. The above process was repeated for electron sources of FWHM equal to 0.5, 1.0, 1.5 and 2.0 mm. At this step, the incident electron source on the target is known to be Gaussian during the MC simulations. Thus, the RMSE values evaluate the performance of the method in reconstructing the expected functional form. The reconstruction was also repeated for different SSD levels of 105, 125 and 150 cm with the PSFs recalculated on each SSD level. The electron source FWHM was set to the commissioned values (1.25 × 1.1 mm).

As a second step the measured film profiles were used as an input to the algorithm. The reconstructed source was compared to the electron and photon sources that were previously determined during MC model commissioning for small fields, by inspecting the normalized RMSE (%) between the reconstructed source and a Gaussian fit, the FWHM and the Full Width at Tenth of Maximum (FWTM). It should be noted that in this case possible deviations from a Gaussian functional form may be attributed not only to the limitations of the algorithm, but also to the proximity of the source shape to a Gaussian distribution.

Finally, the reconstructed FWHM of the source and of the jaw positions were used as input source parameters to the MC beam model. The calculated dose profiles of the experimental set-up were directly compared to the respective measurements in the crossplane and inplane orientations.

7.2.10 Uncertainty analysis

The uncertainties related to the reconstructed source distribution and the FWHM and FWTM metrics can be classified in 3 main components: (i) *Jaw positioning*, related to possible misestimation of the actual jaw position by the algorithm, which would result in an erroneous system matrix. The total standard deviation (1 σ) in jaw positioning was estimated to be the jaw displacement that resulted in a mean local error between calculated and measured profiles less than 10 % in the 90 - 10 % dose region. In this work this displacement was found to be about 0.2 mm. (ii) *Experimental*, related to measurement uncertainties. The total experimental uncertainty was derived by summing in quadrature the standard deviation (1 σ) of the 5 repeated film measurements and the film calibration fitting uncertainties. The mechanical accelerator jaw repositioning is also included in this component. (iii) *PSF*, related to possible misestimation of the PSF due to source variations. The PSF uncertainty was calculated as the standard deviation (1 σ) of the PSFs extracted for source sizes of 0.5, 1.0, 1.5 and 2.0 mm.

Each uncertainty component was propagated to the source as follows: first a deviation from the mean of a specific effect (e.g. jaw position) was sampled from a Gaussian distribution, while the rest remained constant (e.g. experimental and PSF). The Gaussian distribution had a standard deviation equal to the effect's estimated standard deviation. For each sampled point the source was reconstructed using the MLEM algorithm. Another point was then sampled and the source reconstructed again. The procedure continued until the standard deviation of all reconstructed FWHM values appeared not to vary more than 1 %. The total uncertainty was calculated by randomly sampling a deviation from the mean of all effects (e.g. jaw position, experimental and PSF) at the same time and repeating the previous procedure.

7.3 Results

The MC calculated dose profiles after 2 mm of Pb, before and after deconvolution with the respective PSF, are presented in figure 7.2 for the crossplane and inplane orientation. In order to evaluate the accuracy of the kernel in debluring the profile from the electron and photon scattering effects, the profiles are directly compared to the expected photon fluence at a SSD of 105 cm. The calculations were performed using the MC accelerator model for the commissioned values of the electron source FWHM and jaw positions. Figure 7.3 presents the average PSF for electron sources of FWHM equal to 0.5, 1.0, 1.5 and 2.0 mm along with the 1 standard deviation uncertainty level. The PSFs were calculated using the methodology presented in section 2.5. The average PSF had a FWHM (δFWHM) equal to 0.88 (0.05) mm and 0.85 (0.13) mm at the crossplane and inplane orientations respectively.

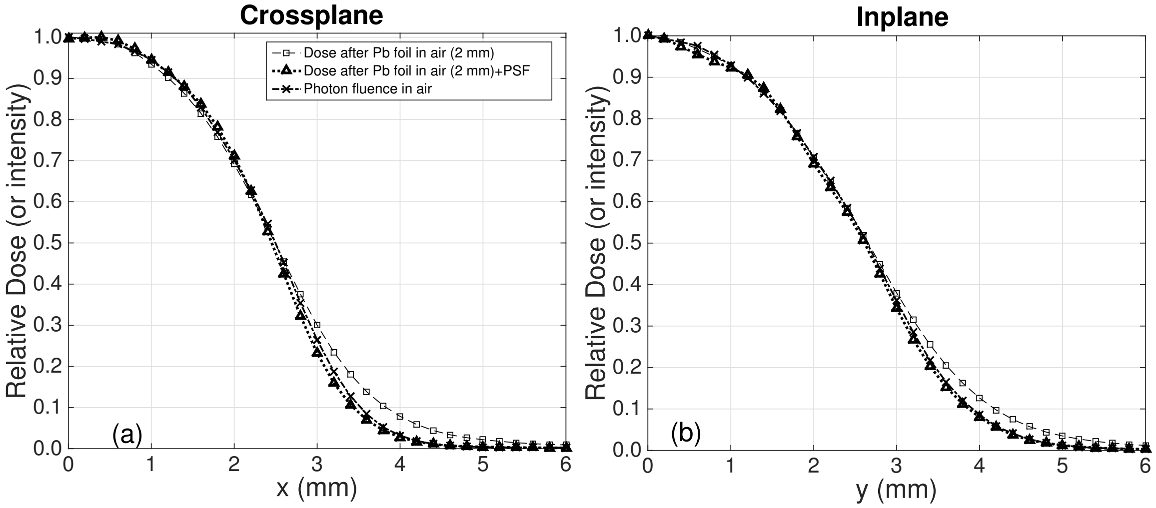

FIGURE 7.2: Monte Carlo dose calculations of the crossplane (a) and inplane (b) profiles after 2 mm of Pb in air (□) and after 2 mm of Pb in air deconvolved using the respective PSF kernel (△). The dose profiles are directly compared to the calculated photon fluence (x).

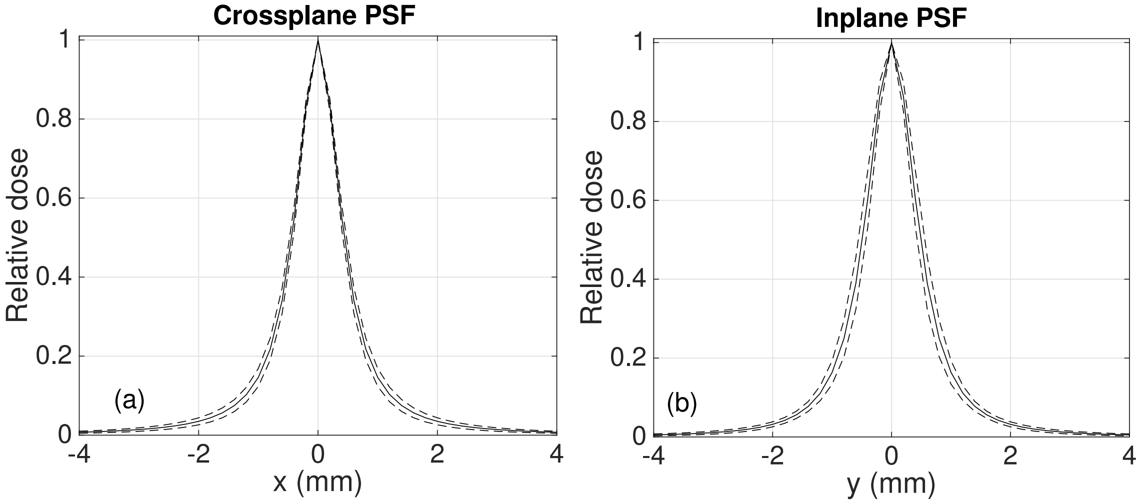

FIGURE 7.3: The average point spread function after 2 mm of Pb (solid line) for the crossplane (a) and inplane (b) orientations. The standard deviation (1 σ) due to source variations is presented with the dashed lines.

The reconstructed sources using the MC calculated dose profiles of the experimental set-up as an input are presented in figure 7.4. The calculations were performed for a range of typical electron Gaussian sources of FWHM equal to 0.5 - 2 mm. The respective photon sources at a depth of 0.2 mm in the target are also presented. The Gaussian fits to the reconstructed source distribution exhibited a RMSE (%) in the range of 2.3 % - 5.4 % and of 2.2 % - 4.1 % for the crossplane and inplane orientations respectively. The relative intensity differences between the reconstructed sources and the electron and photon sources (figure 7.5) presented a local agreement within 10 % in all cases with the major discrepancies occurring in regions of high intensity gradient and for source sizes of FWHM equal to 0.5 and 1 mm.

The ability of the MLEM algorithm to reconstruct the FWHM of the expected source and field size is presented in table 1. The reconstructed FWHM agrees to within 0.12 mm and 0.10 mm to the electron source FWHM (incident on the target) and photon source FWHM (at 0.2 mm depth in the target) respectively. The photon source appears broader than the electron source by 0.02 - 0.04 mm. The reconstructed jaw positions reproduce the expected values with an accuracy better or equal to 0.2 mm.

To evaluate the accuracy of the method to reproduce the expected dose profile, the reconstructed dose profiles are directly compared to the MC calculated dose profiles that were used as an input (figure 7.6). Discrepancies are observed mainly for the smallest source size (FWHM=0.5 mm) and in the tail region with a local dose difference reaching 17.7 % in the 90 - 10 % dose region.

Table 7.2 evaluates the sensitivity of the method to the choice of the exit plane location. The reconstruction was performed for different SSD values of 105, 125 and 150

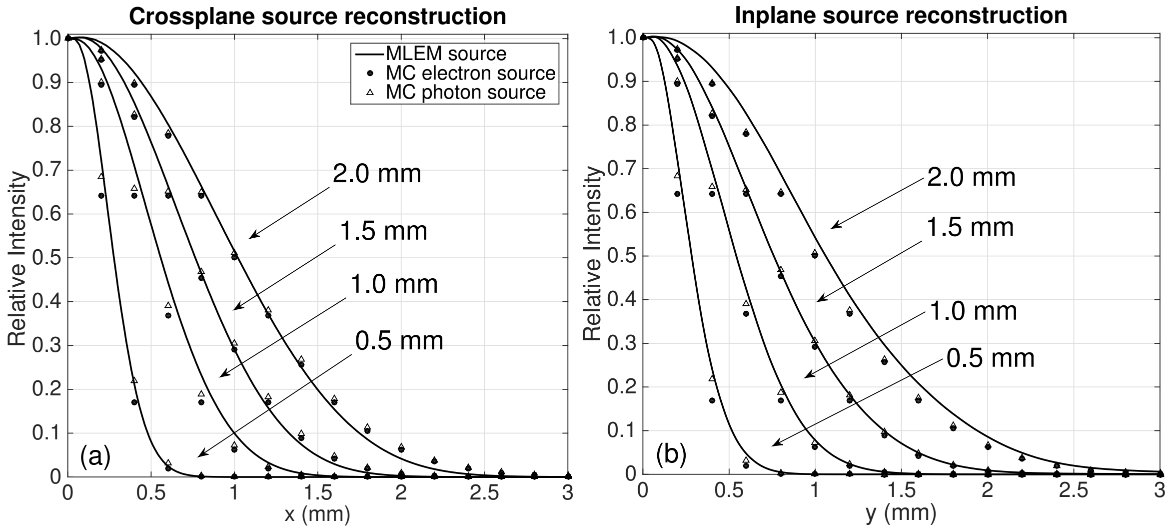

FIGURE 7.4: Reconstructed source distributions using the MC calculated dose profiles of the experimental set-up as input. Calculations were repeated for electron sources of FWHM equal to 0.5, 1.0, 1.5 and 2.0 mm. Reconstructed sources are directly compared to the expected Gaussian electron (•) and photon (△) sources.

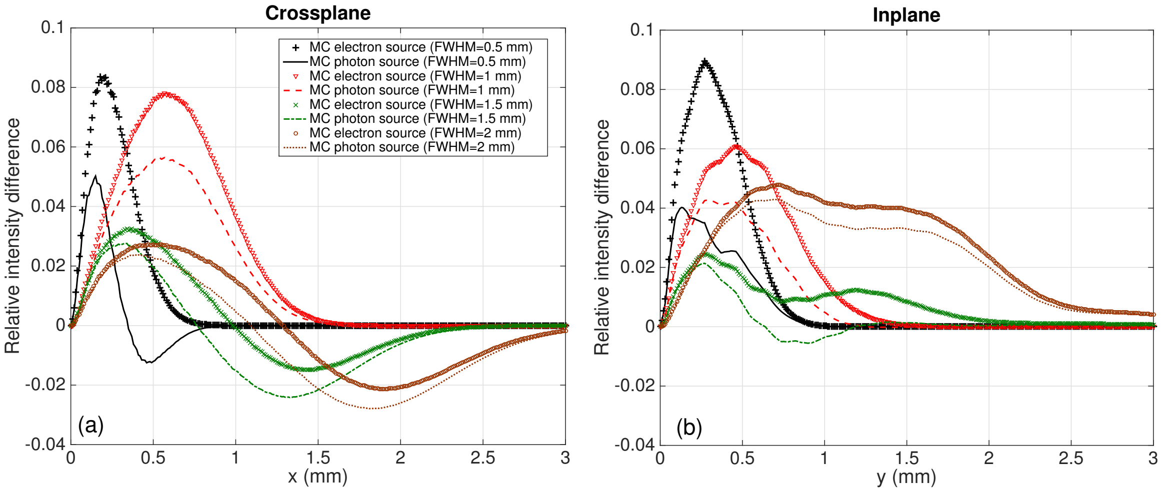

FIGURE 7.5: Relative local intensity difference between the reconstructed source distribution and the respective MC electron source (symbols) and photon source (lines) at a depth of 0.2 mm in the target for FWHM of 0.5, 1.0, 1.5 and 2.0 mm.

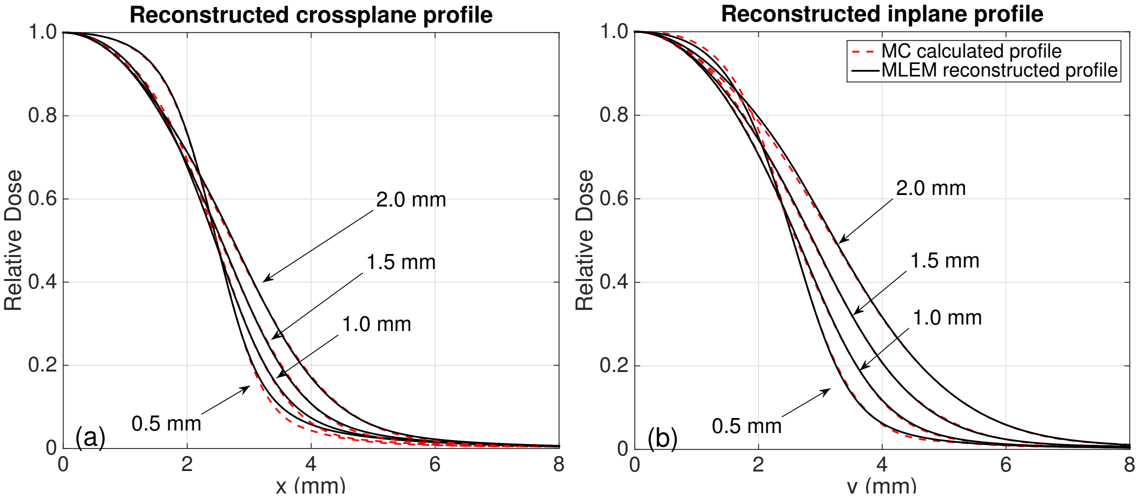

FIGURE 7.6: Reconstructed dose profiles (solid lines) and MC calculated dose profiles of the experimental set-up (dashed lines). Calculations were repeated for sources of FWHM equal to 0.5, 1.0, 1.5 and 2 mm.

TABLE 7.1: Reconstructed FWHM of the source and reconstructed field size (crossplane (X) × inplane (Y)) using the MC calculated dose profiles as input. The expected FWHM of the electron source (incident on the target) and photon source (at 0.2 mm depth in the target) are presented. The expected field size was set to the commissioned values (4.7×4.9 mm^2)

e^- source (mm^2)	γ source (mm^2)	MLEM source (mm^2)	Field (mm^2)
0.5×0.5	0.54×0.54	0.54×0.56	4.7×4.9
1.0×1.0	1.03×1.03	1.10×1.08	4.6×4.9
1.5×1.5	1.53×1.53	1.52×1.52	4.7×4.9
2.0×2.0	2.03×2.02	2.04×2.12	4.8×4.7

TABLE 7.2: Reconstructed FWHM of the source and reconstructed field size (crossplane (X) × inplane (Y)) for SSD values of 105, 125 and 150 cm. The expected source and field size were set to the commissioned values (1.25×1.10 mm^2 and 4.7×4.9 mm^2)

SSD (cm)	MLEM source (mm)	Field (mm^2)
105	1.22×1.08	4.6×4.9
125	1.20×1.08	4.8×5.0
150	1.24×1.12	4.8×5.0

cm. The MC electron source and field size were set in this case to the commissioned values of $\mathrm{FWHM_x}$ = 1.25 mm and $\mathrm{FWHM_x}$ = 1.10 mm and 4.7 × 4.9 mm^2 respectively. The reconstructed source FWHM agreed to each other within 0.04 mm and the reconstructed jaw settings within 0.2 mm.

The reconstructed source using the film dose profile measurements at the Varian Novalis accelerator is presented in figure 7.7. In the same figure the Gaussian electron source and the respective photon source, as they were determined during model commissioning, are also presented. The reconstructed source exhibited a FWHM of 1.22 mm (± 0.12) and 1.21 mm (± 0.11) at the crossplane and inplane orientation respectively. The RMSE (%) of a Gaussian fit was found to be 2.4 % and 2.7 % for the crossplane and inplane orientations respectively. The reconstructed field side for this set of measurements was 4.4 mm on both orientations.

The propagated effects of the jaw positioning, experimental and PSF uncertainties on the reconstructed source are presented in figure 7.9. Overall, the jaw positioning uncertainties resulted in the most significant source variations, while PSF and experimental uncertainties mainly affected the tail region. Table 7.3 summarizes the reconstructed source parameters and uncertainty components.

Finally, the dose profiles were recalculated using the accelerator MC beam model with the electron Gaussian source set to the reconstructed FWHM value of 1.22 × 1.21 mm^2 and field size of 4.4 × 4.4 mm^2 (figure 7.10). The dose distributions exhibited an agreement with the film measurements of 1.2 % in the 90-10 % dose region.

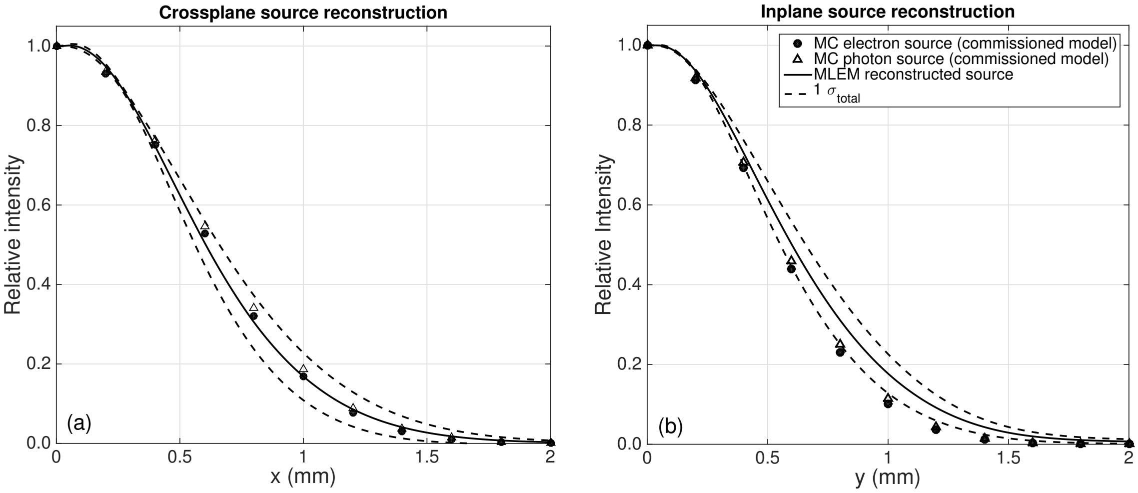

FIGURE 7.7: MLEM reconstructed source distributions using the film profile measurements as input (solid lines). The Gaussian electron (•) and photon (△) sources are also presented as they were determined during commissioning. The 1 standard deviation (1 σ) total uncertainty level is presented with dashed lines.

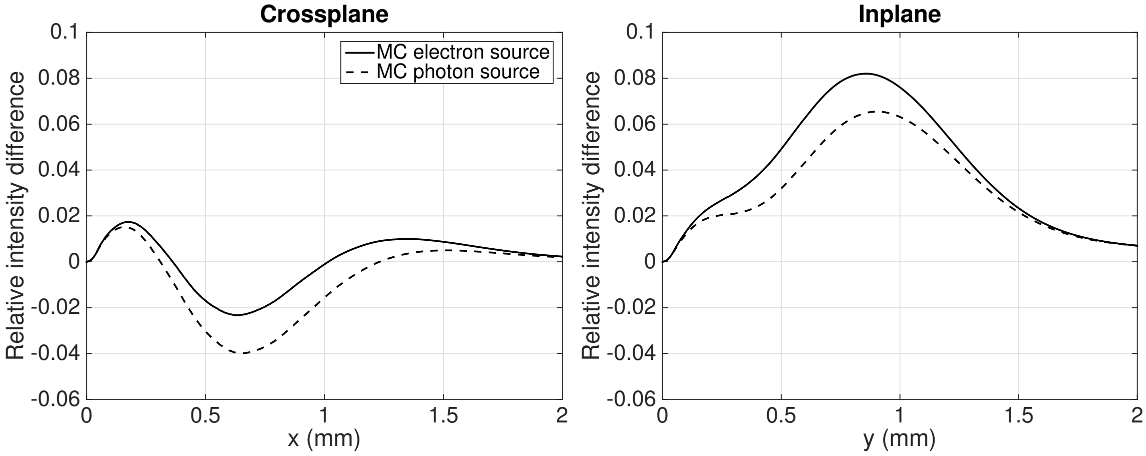

FIGURE 7.8: Relative local intensity difference between the reconstructed source distribution and the MC electron (solid line) and photon Gaussian sources (dashed line) as determined during commissioning.

7.4 Discussion

Measuring the photon fluence in air using a 2 mm Pb foil as build-up material proved to be challenging and some penumbra broadening still appeared in the dose region below 40 %. For that purpose, the use of a PSF function to account for the electron blurring and photon scatter in the build-up material appeared to be important. In fact, performing the MLEM reconstruction without using the PSF, resulted in an overestimation of the source up to 0.42 mm.

The PSFs, extracted by the MC calculations and the optimization procedure presented minimal sensitivity to the source size selected during the simulations (figure 7.3). This result ensures that the method can be applied to any accelerator of the same geometry without prior knowledge of the source. The observed variations in the PSF distributions resulted in only small variations of the reconstructed source as can be seen in figures 7.7e and 7.7f. Thus, a pre-calculated average PSF can be provided to the user or even included in the system matrix. In the latter case the blurring is inherently included in the model and the end user only needs to input the measured dose profiles. It should be emphasized that different accelerator designs may present different PSFs. Further research will be needed to verify the applicability of a universal PSF for all accelerator designs.

The MLEM reconstruction using the MC calculated dose profiles with known electron Gaussian sources reproduced the expected Gaussian shape with an accuracy of 5.4 % and 4.1 % (RMSE) in the crossplane and inplane orientations respectively. The maximum deviations were observed for the smallest source with FWHM of 0.5 mm. The discrepancy is also depicted in the tail and shoulder regions of the reconstructed

TABLE 7.3: FWHM and FWTM values of the reconstructed source using the film profile measurements, the MC electron source (incident on the target) and the photon source (at 0.2 mm depth in the target) as determined during model commissioning. The total and component uncertainties of the reconstruction are presented at the 1 σ level.

	FWHM$_x$ (mm)	FWTM$_x$ (mm)	FWHM$_y$ (mm)	FWTM$_y$ (mm)
e^- source	1.25	2.26	1.10	2.00
γ source	1.28	2.32	1.13	2.04
rec source	1.22	2.29	1.21	2.32
σ_{total} (rec source)	0.12	0.27	0.11	0.20
σ_{jaw} (rec source)	0.11	0.21	0.10	0.15
σ_{exp} (rec source)	0.03	0.12	0.04	0.11
σ_{psf} (rec source)	0.04	0.16	0.01	0.07

dose profiles upon convergence of the MLEM algorithm. The difficulty in reconstructing the source shape could potentially be attributed to the steep gradient change exhibited in this case.

The reconstructed source appears to overestimate the FWHM in most of the cases relative to the expected electron Gaussian source incident on the target (figures 7.4, 7.5 and table 7.1). This can be partly explained by the electron blurring occurring in the target. The photon source at 0.2 mm depth in the target indeed appeared broader up to 0.04 mm relative to the electron source incident on the target. This result is in agreement with the work by Sterpin et al., 2011 that reported a broadening up to 0.06 mm for a similar incident energy. This finding implies that the reconstruction algorithm actually reconstructs a distribution closer to the photon source and not to the electron source, even though both are in close agreement to each other.

A second reason for the FWHM overestimation may be related to the observation that the overestimation of the source was often coupled with an underestimation of the projected field size and vice-versa. In fact in the cases that the correct field size

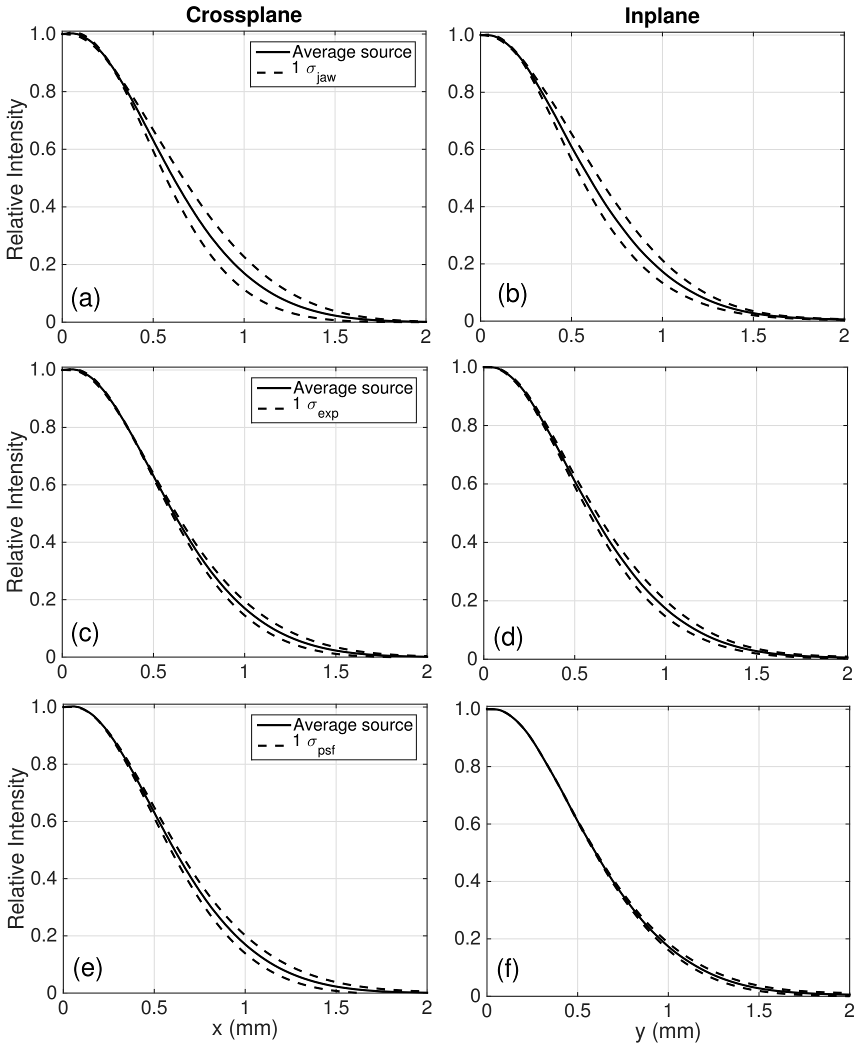

FIGURE 7.9: Uncertainty components of the experimentally reconstructed source (solid lines) using the film measurements. Uncertainties include the effects of jaw positioning (a,b), experimental (c,d) and PSF (e,f) (dashed lines).

was reproduced (FWHM of 0.5 mm and 1.5 mm in table 7.1), the MLEM reconstructed intensity distribution presented an exceptional agreement with the photon intensity distribution (figures 7.4 and 7.5) and the FWHM was within 0.02 mm to the expected value. The overall accuracy in the jaw position estimation was found to be 0.2 mm, a result which agrees with the initially estimated precision. The above observations emphasize the need for accurate reconstruction of both the source distribution and jaw position in order to properly predict the source occlusion effect. It should be noted that for the largest source size (FWHM=2 mm) the uncertainties in jaw positioning estimation increased and different combinations of source size/jaw positions could still provide acceptable agreement between reconstructed and expected dose profiles.

The experimentally reconstructed source reproduced a Gaussian shape with RMSE (%) values up to 2.7 %. The results are within the range of the RMSE (%) values reported previously using the MC simulations of known Gaussian electron sources. Relative to the previously commissioned electron source the reconstructed FWHM was -0.03 mm lower and +0.11 mm higher in the crossplane and inplane orientations respectively. Relative to the corresponding photon source the reconstructed FWHM was -0.06 mm lower and +0.08 mm higher in the crossplane and inplane orientations. In both cases, the reconstructed source agrees within the estimated total uncertainty level (1 σ), even though only marginally for the inplane orientation. More importantly, if the reconstructed source FWHM and field size are used as an input to the MC accelerator beam model, an excellent agreement was observed between measured and calculated dose profiles (figure 7.10).

The uncertainty component analysis, presented in figure 7.7 and table 7.2, indicates that the estimation of the jaw position is the major source of uncertainty during reconstruction. A 0.2 mm misestimation of the collimator position would result in about 0.10-0.11 mm misestimation of the source's FWHM. This, in turn, would result in output factor variations of 1.5 - 3.0 % for typical source sizes in the range of 0.8 to 1.4 mm and penumbra width (80 - 20 %) variations of 3-4 %. This level of accuracy still competes with most small field detectors that are currently used in the clinic. The development of independent methods for estimating the correct jaw position would greatly improve the performance of the source reconstruction algorithm. Uncertainties due to PSF variations with the source and experimental measurements, including mechanical jaw positioning, were less significant in the prediction of the FWHM. However, these effects presented a much more significant impact on the tail regions of the source distribution, which is illustrated in the reported FWTM uncertainties (table 7.3).

7.5 Conclusion

In this work, we investigated the performance of a MLEM-based source reconstruction technique for clinical linear accelerators using small field photon fluence profiles. The use of a high density build-up material along with an appropriate PSF were found important for extracting accurately the photon fluence. The PSFs exhibited overall a minimal dependence on the source. The model was able to reconstruct the electron source with an overall accuracy of 0.12 mm for typical source sizes of FWHM values of 0.5 to 2 mm that were tested in simulations. Experimentally, the method exhibited an overall

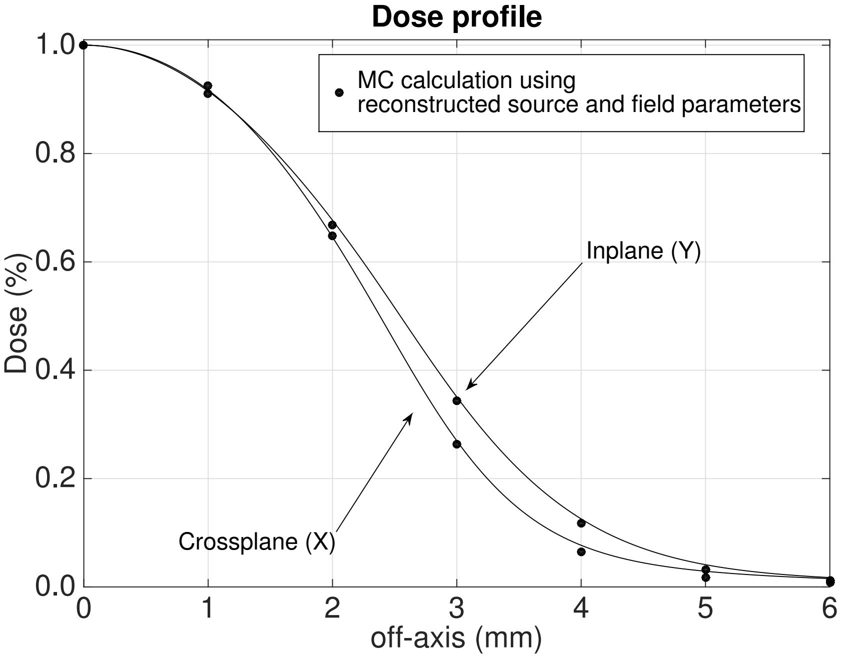

FIGURE 7.10: MC calculated crossplane and inplane dose profiles, using the MLEM reconstructed source and jaw parameters, compared to the film measurements.

accuracy level of 0.11 mm with respect to a previously commissioned MC model, with the most significant uncertainty attributed to the estimation of the jaw position at the time of measurements. The results of this study indicate that MLEM-based approaches could be a powerful and practical tool for the direct reconstruction of the source distribution, without any prior assumptions. In the future, such techniques could become part of a quality assurance procedure that would evaluate potential source variations through time and machine usage or between different accelerator types.

Acknowledgements

PP would like to acknowledge Dr. Anders Ahnesjö, Dr. Andrew Reader and Sangkyu Lee for important conversations on the subject as well as Compute Canada/Calcul

Quebec for providing computing resources. PP gratefully acknowledges the financial support by the Alexander S. Onassis Public Benefit Foundation in Greece and by the CREATE Medical Physics Research Training Network grant of the Natural Sciences and Engineering Research Council (Grant number: 432290). IL acknowledges research funding from the Research Institute of the McGill University Health Centre, the Montreal General Hospital Foundation, and the Phil Gold Fellowship.

Chapter 8

Conclusions

This work focused on two important problems in small field photon dosimetry: the calibration and response of modern detector systems in relative dosimetry and the direct reconstruction of the source intensity distribution of a clinical linear accelerator. In this section a summary of the main findings will be presented on both areas.

8.1 On the detector response in small photon fields

The accuracy of modern detector systems, including a liquid ionization chamber (PTW microLion), an unshielded silicon diode (Exradin D1V, SI), a synthetic diamond (PTW microDiamond) and a plastic scintillator (Exradin W1, SI) was first examined by Monte Carlo methods relative to the expected calculations in water. In this approach perturbations due to the presence of high density materials and volume averaging effects of the sensitive volume are accurately reported. For the field sizes of 1 × 1 cm^2 and 2 × 2 cm^2, all detector systems reproduced accurately (within 1 %) the expected output factor readings in water. Discrepancies, however, were observed for the smallest field size of 0.5×0.5 cm^2 which is the smallest field size used currently in the clinic. In that case two types of detector designs appeared to provide the optimum performance:

- the scintillator system, manufactured using solely plastic materials with material densities close to water resulted in small perturbations. In addition, for a diameter of 1 mm of the sensitive volume a small volume averaging effect was observed. Overall the agreement was within 1 % relative to dose in water measurements.
- The synthetic diamond system. In this case the diamond substrate caused a significant over-response which however was compensated by the increased volume averaging due to the 2.2 mm diameter sensitive volume. Overall the agreement was within 1.3 % relative to dose in water. In principle the concept of volume averaging compensation can be applied to the other detector systems to improve their performance.

As a second step the accuracy of the MC-derived correction factors needs to be verified experimentally, especially in the case of plastic scintillation dosimeters where a special calibration is required prior of measurements to account for the contaminant Cerenkov signal. In principle, the detector-specific output factors should converge to the same field factor after the MC-derived correction factors are applied. To that end repetitive output factor measurements were performed with all detector systems and the respective corrections were applied. In general the microLion, D1V diode and microDiamond measurements presented good agreement with the respective MC values. The detector readings agreed within experimental uncertainties after the MC-derived correction factors were applied with the exception of the W1 plastic scintillator which presented overall a higher response. This result was confirmed independently by performing measurements with a similar plastic scintillator dosimetry system (CHUQ PSD) under the same experimental conditions. The CHUQ PSD presented a close agreement with the expected field factor even for the smallest field size, which demonstrates the great potential that PSDs have in small field dosimetry. However, the findings of this study also highlight the fact that MC corrections might not necessarily reveal the full correction required for a plastic scintillator dosimetry system and discrepancies between similar scintillator systems may appear.

The accuracy of the detector response in small field profiles was also examined where it was observed that all detectors studied exhibited a good agreement with water calculations within the field. More significant discrepancies were observed outside the field size, beyond the 50 % dose level, especially in the tail regions. High density material perturbations resulted in an under-response, which was again partly compensated by an increased volume averaging effect in the case of the microLion and microDiamond designs. The plastic scintillation dosimeter appeared again to be the ideal choice combining both minimal volume averaging and material perturbation effects. The needed corrections in the tail regions should not be dismissed since measured penumbra widths (80-20 % or 90 - 10 %) are used as input during TPS commissioning.

A dosimeter that could potentially overcome the issues observed in the tail profiles is EBT-based radiochromic film. However, radiochromic film is most often associated with low sensitivity and large uncertainties during calibration in the low dose regions (less than 1 Gy) when the red channel in the transmission scanning mode is utilized. Potential benefits in using the reflection scanning mode instead to increase the sensitivity were examined. The reflection scanning was proven to offer advantages if the red channel was used and the calibration was restricted in the dose region of 0 - 2 Gy. For higher dose regions the dosimeter appeared to saturate which resulted in a highly non-linear behaviour. As a result, experimental and fitting uncertainties were significantly increased. However, for doses higher than 2 Gy the green channel could be used instead which presented similar behaviour to the red channel in the transmission mode. Thus, a two-color protocol was suggested in the full span of 0 - 8 Gy for EBT3 radiochromic film dosimetry under the reflection scanning mode. This protocol was utilized in the film measurements performed for the direct source reconstruction study.

8.2 On the reconstruction of the source intensity distribution

Determining the source distribution of a clinical linear accelerator was the second goal of this work. In beam models the source is characterized by an elliptical Gaussian source and detector-specific output factor and profile measurements are used to determine the FWHM of the Gaussian source. An iterative tuning procedure is most often followed, until the best agreement is reached between model calculations and measurements.

In this work, the MC beam model commissioning was executed in two steps: i) using large and intermediate field sizes (down to a 2 × 2 cm^2) and ii) using small field sizes (0.5 × 0.5 - 2 × 2 cm^2). In the latter case the detector model was explicitly included in the calculations. Both commissioning procedures resulted in an excellent agreement with profile measurements. However, discrepancies between the estimated source size in each case were observed. The large field commissioning procedure resulted in a FWHM of 0.9 mm and 1.0 mm in the crossplane and inplane orientations respectively. The small field commissioning procedure resulted in a FWHM of 1.25 mm and 1.10 mm respectively. The observed discrepancy resulted in a relative difference of 4.4 % in the MC output factor calculations using the microLion model for the smallest field size (0.5 × 0.5 cm^2). In addition, if the detector is not explicitly modeled, but instead a water voxel with the same dimensions of the microLion's active volume is used, the output factor will be about 5 % lower. The above findings lead us to two important conclusions in small field beam commissioning: i) small field profiles and output factors need to be measured and included in the tuning procedure for the source size to be properly estimated and ii) the detector needs to be explicitly modeled in the calculations. Approximating only the sensitive volume of a detector with a water voxel of similar dimensions is not adequate and may result in significant discrepancies. This result depends on the design specifications of the detector, which in some cases is such that the volume averaging compensates material perturbations.

In light of the previous findings, the work focused on developing a method, including both an algorithm and an experimental procedure, that would allow the direct reconstruction of the source intensity distribution. Such a method avoids a "trial-and-error" tuning procedure which is time-consuming and may result in erroneous source estimation due to detector-specific perturbations. Furthermore, the method, as a true direct reconstruction, should not make any prior assumptions regarding the source functional form. The method followed in this work was based on an MLEM-based imaging technique and photon fluence profile measurements in the smallest field size of 0.5×0.5 cm^2. The MLEM algorithm iteratively ray-traces photons from the source plane to the measurement plane and vice-versa and extracts corrections based on actual fluence profile measurements. The photon fluence profiles were extracted by film measurements, a Pb foil and a deconvolution kernel. The film measurements were scanned in reflection mode to reduce the uncertainties in the low dose region of 0 - 2 Gy.

Overall, the method reproduced the correct electron source FWHM to within 0.12 mm compared to MC benchmark simulations and the previously determined electron source during model commissioning. The source distribution agreed with a Gaussian shape within 5.4 % (RMSE) or better. The reconstructed source appeared in general to be broader than the expected electron source, a result which is partly attributed to the broader bremsstrahlung source distribution generated in the beginning of the target.

8.3 Future direction

Future work should focus on developing robust and reproducible “correction-free” detectors by compensating methods or by using water-like materials, such as in the case of radiochromic film and PSDs. For the latter case special attention is needed for the calibration process. Future research should focus on identifying the sources of uncertainty in the different PSD systems, especially as they relate to the optical fiber and photodetector technical specifications. For the source reconstruction, future work could use the technique suggested in this work to measure the source distributions of different accelerator systems and examine possible source variations through time or machine usage. Another interesting expansion of the work could be developing a 3-D MLEM reconstruction technique. It is hoped that the findings of this work will contribute to the body of knowledge and improve the dosimetry in small radiation fields.

Bibliography

Alfonso, R et al. (2008). “A new formalism for reference dosimetry of small and non-standard fields”. In: *Medical physics* 35.11, pp. 5179–5186.

Ali, ESM, MR McEwen, and DWO Rogers (2012). “Unfolding linac photon spectra and incident electron energies from experimental transmission data, with direct independent validation”. In: *Medical physics* 39.11, pp. 6585–6596.

Almberg, Sigrun Saur et al. (2012). “Monte Carlo linear accelerator simulation of megavoltage photon beams: independent determination of initial beam parameters”. In: *Medical physics* 39.1, pp. 40–47.

Alva, H et al. (2002). “The use of a reflective scanner to study radiochromic film response”. In: *Physics in medicine and biology* 47.16, p. 2925.

Araki, Fujio (2006). “Monte Carlo study of a Cyberknife stereotactic radiosurgery system”. In: *Medical physics* 33.8, pp. 2955–2963.

Archambault, Louis et al. (2007). “Water-equivalent dosimeter array for small-field external beam radiotherapy”. In: *Medical physics* 34.5, pp. 1583–1592.

Aspradakis, Maria M (2010). *Small Field MV Proton Dosimetry*. Institution of Physics, Engineering in Medicine, and Biology.

Attix, Frank Herbert (2008). *Introduction to radiological physics and radiation dosimetry*. John Wiley & Sons.

Azangwe, Godfrey et al. (2014). “Detector to detector corrections: A comprehensive experimental study of detector specific correction factors for beam output measurements for small radiotherapy beams”. In: *Medical physics* 41.7, p. 072103.

Bassinet, C et al. (2013). “Small fields output factors measurements and correction factors determination for several detectors for a CyberKnife® and linear accelerators equipped with microMLC and circular cones”. In: *Medical physics* 40.7, p. 071725.

Beaulieu, L et al. (2013). “Current status of scintillation dosimetry for megavoltage beams”. In: *Journal of Physics: Conference Series*. Vol. 444. 1. IOP Publishing, p. 012013.

Beddar, AS, TR Mackie, and FH Attix (1992a). “Water-equivalent plastic scintillation detectors for high-energy beam dosimetry: I. Physical characteristics and theoretical considerations”. In: *Physics in medicine and biology* 37.10, p. 1883.

— (1992b). “Water-equivalent plastic scintillation detectors for high-energy beam dosimetry: II. Properties and measurements”. In: *Physics in medicine and biology* 37.10, p. 1901.

Beddar, AS, DJ Mason, and PF O’Brien (1994). “Absorbed dose perturbation caused by diodes for small field photon dosimetry”. In: *Medical physics* 21.7, pp. 1075–1079.

Benmakhlouf, Hamza, Josep Sempau, and Pedro Andreo (2014). “Output correction factors for nine small field detectors in 6 MV radiation therapy photon beams: A PENELOPE Monte Carlo study”. In: *Medical physics* 41.4, p. 041711.

Berger, Martin J (1963). “Monte Carlo calculation of the penetration and diffusion of fast charged particles”. In: *Methods in computational physics* 1, pp. 135–215.

Bortfeld, Thomas (2006). “IMRT: a review and preview”. In: *Physics in medicine and biology* 51.13, R363.

Bouchard, Hugo et al. (2009a). “Ionization chamber gradient effects in nonstandard beam configurations”. In: *Medical physics* 36.10, pp. 4654–4663.

Bouchard, Hugo et al. (2009b). “On the characterization and uncertainty analysis of radiochromic film dosimetry”. In: *Medical physics* 36.6, pp. 1931–1946.

Burlin, TE (1966). “A general theory of cavity ionisation”. In: *The British journal of radiology* 39.466, pp. 727–734.

Caprile, P and GH Hartmann (2009). “Development and validation of a beam model applicable to small fields”. In: *Physics in medicine and biology* 54.10, p. 3257.

Charles, PH et al. (2013). “Monte Carlo-based diode design for correction-less small field dosimetry”. In: *Physics in medicine and biology* 58.13, p. 4501.

Charles, PH et al. (2014). “A practical and theoretical definition of very small field size for radiotherapy output factor measurements”. In: *Medical physics* 41.4, p. 041707.

Chen, Quan et al. (2011). “A slit method to determine the focal spot size and shape of TomoTherapy system”. In: *Medical physics* 38.6, pp. 2841–2849.

Chetty, Indrin J et al. (2007). “Report of the AAPM Task Group No. 105: Issues associated with clinical implementation of Monte Carlo-based photon and electron external beam treatment planning”. In: *Medical physics* 34.12, pp. 4818–4853.

Chung, Eunah, Stephen Davis, and Jan Seuntjens (2013). “Experimental analysis of general ion recombination in a liquid-filled ionization chamber in high-energy photon beams”. In: *Medical physics* 40.6, p. 062104.

Ciancaglioni, I et al. (2012). “Dosimetric characterization of a synthetic single crystal diamond detector in clinical radiation therapy small photon beams”. In: *Medical physics* 39.7, pp. 4493–4501.

Clift, MA, PN Johnston, and DV Webb (2002). "A temporal method of avoiding the Cerenkov radiation generated in organic scintillator dosimeters by pulsed megavoltage electron and photon beams". In: *Physics in medicine and biology* 47.8, p. 1421.

Cranmer-Sargison, G et al. (2011). "Implementing a newly proposed Monte Carlo based small field dosimetry formalism for a comprehensive set of diode detectors". In: *Medical physics* 38.12, pp. 6592–6602.

— (2012). "Monte Carlo modelling of diode detectors for small field MV photon dosimetry: detector model simplification and the sensitivity of correction factors to source parameterization". In: *Physics in medicine and biology* 57.16, p. 5141.

Cranmer-Sargison, Gavin et al. (2013). "A methodological approach to reporting corrected small field relative outputs". In: *Radiotherapy and Oncology* 109.3, pp. 350–355.

Crop, Frederik et al. (2009). "The influence of small field sizes, penumbra, spot size and measurement depth on perturbation factors for microionization chambers". In: *Physics in medicine and biology* 54.9, p. 2951.

Czarnecki, Damian and Klemens Zink (2013). "Monte Carlo calculated correction factors for diodes and ion chambers in small photon fields". In: *Physics in medicine and biology* 58.8, p. 2431.

Das, Indra J, George X Ding, and Anders Ahnesjö (2008). "Small fields: Nonequilibrium radiation dosimetry". In: *Medical physics* 35.1, pp. 206–215.

De Angelis, C et al. (2002). "An investigation of the operating characteristics of two PTW diamond detectors in photon and electron beams". In: *Medical physics* 29.2, pp. 248–254.

De Boer, SF, AS Beddar, and JA Rawlinson (1993). "Optical filtering and spectral measurements of radiation-induced light in plastic scintillation dosimetry". In: *Physics in Medicine and Biology* 38.7, p. 945.

Devic, Slobodan (2011). "Radiochromic film dosimetry: past, present, and future". In: *Physica medica* 27.3, pp. 122–134.

Devic, Slobodan et al. (2004). "Dosimetric properties of improved GafChromic films for seven different digitizers". In: *Medical physics* 31.9, pp. 2392–2401.

Devic, Slobodan et al. (2005). "Precise radiochromic film dosimetry using a flat-bed document scanner". In: *Medical physics* 32.7, pp. 2245–2253.

Droege, Ronald T and Richard L Morin (1982). "A practical method to measure the MTF of CT scanners". In: *Medical physics* 9.5, pp. 758–760.

Eklund, Karin and Anders Ahnesjö (2008). "Fast modelling of spectra and stopping-power ratios using differentiated fluence pencil kernels". In: *Physics in medicine and biology* 53.16, p. 4231.

— (2009). "Modeling silicon diode energy response factors for use in therapeutic photon beams". In: *Physics in medicine and biology* 54.20, p. 6135.

Fontbonne, JM et al. (2002). "Scintillating fiber dosimeter for radiation therapy accelerator". In: *Nuclear Science, IEEE Transactions on* 49.5, pp. 2223–2227.

Francescon, P, S Cora, and N Satariano (2011). "Calculation of kQclin, Qmsrfclin, fmsr for several small detectors and for two linear accelerators using Monte Carlo simulations". In: *Medical physics* 38.12, pp. 6513–6527.

Francescon, P, W Kilby, and N Satariano (2014). "Monte Carlo simulated correction factors for output factor measurement with the CyberKnife system—results for new detectors and correction factor dependence on measurement distance and detector orientation”. In: *Physics in medicine and biology* 59.6, N11.

Francescon, P et al. (2012). “Monte Carlo simulated correction factors for machine specific reference field dose calibration and output factor measurement using fixed and iris collimators on the CyberKnife system”. In: *Physics in medicine and biology* 57.12, p. 3741.

Francescon, Paolo, Stefania Cora, and Carlo Cavedon (2008). “Total scatter factors of small beams: A multidetector and Monte Carlo study”. In: *Medical physics* 35.2, pp. 504–513.

Frelin, AM et al. (2005). “Spectral discrimination of Čerenkov radiation in scintillating dosimeters”. In: *Medical physics* 32.9, pp. 3000–3006.

Garcia-Vicente, F, JM Delgado, and C Rodriguez (2000). “Exact analytical solution of the convolution integral equation for a general profile fitting function and Gaussian detector kernel”. In: *Physics in medicine and biology* 45.3, p. 645.

Guillot, Mathieu et al. (2011). “Spectral method for the correction of the Cerenkov light effect in plastic scintillation detectors: a comparison study of calibration procedures and validation in Cerenkov light-dominated situations”. In: *Medical physics* 38.4, pp. 2140–2150.

Hall, Eric J and Amato J Giaccia (2006). *Radiobiology for the Radiologist*. Lippincott Williams & Wilkins.

Hall, Eric J and Cheng-Shie Wuu (2003). “Radiation-induced second cancers: the impact of 3D-CRT and IMRT”. In: *International Journal of Radiation Oncology* Biology* Physics* 56.1, pp. 83–88.

Hartmann, Bernadette, Mária Martišíková, and Oliver Jäkel (2010). "Technical note: homogeneity of Gafchromic® EBT2 film". In: *Medical physics* 37.4, pp. 1753–1756.

Heydarian, M, PW Hoban, and Alun H Beddoe (1996). "A comparison of dosimetry techniques in stereotactic radiosurgery". In: *Physics in medicine and biology* 41.1, p. 93.

Huang, Vicky W et al. (2005). "Experimental determination of electron source parameters for accurate Monte Carlo calculation of large field electron therapy". In: *Physics in medicine and biology* 50.5, p. 779.

Jaffray, DA et al. (1993). "X-ray sources of medical linear accelerators: Focal and extra-focal radiation". In: *Medical physics* 20.5, pp. 1417–1427.

Kalef-Ezra, J and K Karava (2008). "Radiochromic film dosimetry: reflection vs transmission scanning". In: *Medical physics* 35.6, pp. 2308–2311.

Kamio, Y and H Bouchard (2014). "Correction-less dosimetry of nonstandard photon fields: a new criterion to determine the usability of radiation detectors". In: *Physics in medicine and biology* 59.17, p. 4973.

Kawrakow, I and D Rogers (2000). "The EGSnrc code system: Monte Carlo simulation of electron and photon transport". In:

Kawrakow, I et al. (2009). "The EGSnrc C++ class library, NRC Report PIRS-898 (rev A)". In: *National Research Council of Canada, Ottawa, Canada*.

Lambert, J et al. (2008). "Cerenkov-free scintillation dosimetry in external beam radiotherapy with an air core light guide". In: *Physics in medicine and biology* 53.11, p. 3071.

Laub, Wolfram U, Theodor W Kaulich, and Fridtjof Nüsslin (1999). "A diamond detector in the dosimetry of high-energy electron and photon beams". In: *Physics in Medicine and Biology* 44.9, p. 2183.

Laub, Wolfram U and Tony Wong (2003). "The volume effect of detectors in the dosimetry of small fields used in IMRT". In: *Medical physics* 30.3, pp. 341–347.

Lawrence, Theodore S, Randall K Ten Haken, and Amato Giaccia (2008). *Principles of radiation oncology*. Cancer: Principles, Practice of Oncology. 8th ed. Philadelphia: Lippincott Williams, and Wilkins.

Lechner, Wolfgang et al. (2013). "Detector comparison for small field output factor measurements in flattening filter free photon beams". In: *Radiotherapy and Oncology* 109.3, pp. 356–360.

Li, X Allen et al. (1995). "Lateral electron equilibrium and electron contamination in measurements of head-scatter factors using miniphantoms and brass caps". In: *Medical physics* 22.7, pp. 1167–1170.

Loewenthal, E et al. (1992). "Measurement of the source size of a 6-and 18-MV radiotherapy linac". In: *Medical physics* 19.3, pp. 687–690.

Lutz, Wendell R, Nasser Maleki, and Bengt E Bjärngard (1988). "Evaluation of a beam-spot camera for megavoltage x rays". In: *Medical physics* 15.4, pp. 614–617.

McKerracher, Carolyn and David I Thwaites (2002). "Verification of the dose to the isocentre in stereotactic plans". In: *Radiotherapy and Oncology* 64.1, pp. 97–107.

Mesures, Bureau International des Poids et, Commission électrotechnique internationale, and Organisation internationale de normalisation (1995). *Guide to the Expression of Uncertainty in Measurement*. International Organization for Standardization.

Morin, Jonathan et al. (2013). "A comparative study of small field total scatter factors and dose profiles using plastic scintillation detectors and other stereotactic dosimeters: The case of the CyberKnife". In: *Medical physics* 40.1, p. 011719.

Munro, P, JA Rawlinson, and A Fenster (1988). "Therapy imaging: Source sizes of radiotherapy beams". In: *Medical physics* 15.4, pp. 517–524.

NCI (2010). *Radiation therapy for cancer*. Report, National Cancer Institute.

Pantelis, E et al. (2010). "On the implementation of a recently proposed dosimetric formalism to a robotic radiosurgery system". In: *Medical physics* 37.5, pp. 2369–2379.

Pantelis, E et al. (2012). "On the output factor measurements of the CyberKnife iris collimator small fields: Experimental determination of the kQ clin, Q msr f clin, f msr correction factors for microchamber and diode detectors". In: *Medical physics* 39.8, pp. 4875–4885.

Papaconstadopoulos, P, F Tessier, and J Seuntjens (2014). "On the correction, perturbation and modification of small field detectors in relative dosimetry". In: *Physics in medicine and biology* 59.19, p. 5937.

Papaconstadopoulos, Pavlos et al. (2014). "A protocol for EBT3 radiochromic film dosimetry using reflection scanning". In: *Medical physics* 41.12, p. 122101.

Pappas, E et al. (2006). “Experimental determination of the effect of detector size on profile measurements in narrow photon beams”. In: *Medical physics* 33.10, pp. 3700–3710.

P.D. La Riviere, Radiation Physics rep (1980). *Radiation Physics Report No 30-80*. Tech. rep. Varian Internal Report.

Pena, Javier et al. (2007). “Automatic determination of primary electron beam parameters in Monte Carlo simulation”. In: *Medical physics* 34.3, pp. 1076–1084.

Podgorsak, Ervin B (2010). *Radiation physics for medical physicists*. Springer Science & Business Media.

Podgorsak, Ervin B et al. (2005). *Radiation oncology physics: a handbook for teachers and students*. Vol. 657. Vienna: International Atomic Energy Agency.

Ralston, Anna et al. (2012). “Small field diode correction factors derived using an air core fibre optic scintillation dosimeter and EBT2 film”. In: *Physics in medicine and biology* 57.9, p. 2587.

Richley, L et al. (2010). “Evaluation and optimization of the new EBT2 radiochromic film dosimetry system for patient dose verification in radiotherapy”. In: *Physics in medicine and biology* 55.9, p. 2601.

Rogers, D and AF Bielajew (1990). “Monte Carlo techniques of electron and photon transport for radiation dosimetry”. In:

Rogers, DWO et al. (1995). “BEAM: A Monte Carlo code to simulate radiotherapy treatment units”. In: *Medical physics* 22.5, pp. 503–524.

Röntgen, Wilhelm Conrad (1896). “On a new kind of rays”. In: *Science*, pp. 227–231.

Salvat, Francesc, José M Fernández-Varea, and Josep Sempau (2006). "PENELOPE-2006: A code system for Monte Carlo simulation of electron and photon transport". In: *Workshop Proceedings*. Vol. 4, p. 7.

Sánchez-Doblado, F et al. (2003). "Ionization chamber dosimetry of small photon fields: a Monte Carlo study on stopping-power ratios for radiosurgery and IMRT beams". In: *Physics in medicine and biology* 48.14, p. 2081.

Sauer, Otto A and Jürgen Wilbert (2007). "Measurement of output factors for small photon beams". In: *Medical physics* 34.6, pp. 1983–1988.

Scott, Alison JD, Alan E Nahum, and John D Fenwick (2008). "Using a Monte Carlo model to predict dosimetric properties of small radiotherapy photon fields". In: *Medical physics* 35.10, pp. 4671–4684.

— (2009). "Monte Carlo modeling of small photon fields: quantifying the impact of focal spot size on source occlusion and output factors, and exploring miniphantom design for small-field measurements". In: *Medical physics* 36.7, pp. 3132–3144.

Scott, Alison JD et al. (2012). "Characterizing the influence of detector density on dosimeter response in non-equilibrium small photon fields". In: *Physics in medicine and biology* 57.14, p. 4461.

Seuntjens, J and DWO Rogers (2009). "Monte Carlo applications in measurement dosimetry". In: *Clinical Dosimetry Measurements in Radiotherapy*, pp. 147–80.

Sham, Edwin et al. (2008). "Influence of focal spot on characteristics of very small diameter radiosurgical beams". In: *Medical physics* 35.7, pp. 3317–3330.

Sterpin, Edmond et al. (2011). “On the relationships between electron spot size, focal spot size, and virtual source position in Monte Carlo simulations”. In: *Medical physics* 38.3, pp. 1579–1586.

Stewart, BW and CP Wild (2014). *World cancer report 2014. IARC Non Serial publication.*

Treuer, H et al. (1993). “The source-density function: determination from measured lateral dose distributions and use for convolution dosimetry”. In: *Physics in Medicine and Biology* 38.12, p. 1895.

Treuer, H et al. (2003). “Geometrical and dosimetrical characterization of the photon source using a micro-multileaf collimator for stereotactic radiosurgery”. In: *Physics in medicine and biology* 48.15, p. 2307.

Underwood, TSA et al. (2013). “Mass-density compensation can improve the performance of a range of different detectors under non-equilibrium conditions”. In: *Physics in medicine and biology* 58.23, p. 8295.

Van Battum, LJ et al. (2008). “Accurate dosimetry with GafChromic™ EBT film of a 6MV photon beam in water: What level is achievable?” In: *Medical physics* 35.2, pp. 704–716.

Wagner, A et al. (2013). “Use of a liquid ionization chamber for stereotactic radiotherapy dosimetry”. In: *Physics in medicine and biology* 58.8, p. 2445.

Walters, B, I Kawrakow, DWO Rogers, et al. (2005). “DOSXYZnrc users manual”. In: *NRC Report PIRS* 794.

Walters, BRB, I Kawrakow, and DWO Rogers (2002). “History by history statistical estimators in the BEAM code system”. In: *Medical physics* 29.12, pp. 2745–2752.

Wang, Lilie LW and Konrad Leszczynski (2007). “Estimation of the focal spot size and shape for a medical linear accelerator by Monte Carlo simulation”. In: *Medical physics* 34.2, pp. 485–488.

Wickman, GORAN (1974). “A liquid ionization chamber with high spatial resolution”. In: *Physics in medicine and biology* 19.1, p. 66.

Wulff, J, K Zink, and I Kawrakow (2008). “Efficiency improvements for ion chamber calculations in high energy photon beams”. In: *Medical physics* 35.4, pp. 1328–1336.

Wulff, Jörg et al. (2010). “Investigation of correction factors for non-reference conditions in ion chamber photon dosimetry with Monte-Carlo simulations”. In: *Zeitschrift für Medizinische Physik* 20.1, pp. 25–33.

Yin, Z, RP Hugtenburg, and AH Beddoe (2004). “Response corrections for solid-state detectors in megavoltage photon dosimetry”. In: *Physics in medicine and biology* 49.16, p. 3691.

Zhu, Timothy C, Bengt E Bjärngard, and Hobart Shackford (1995). “X-ray source and the output factor”. In: *Medical physics* 22.6, pp. 793–798.

Zhu, Timothy C and AS Saini (2009). *Diode dosimetry for megavoltage electron and photon beams*.